Departamento de Ingeniería Mecánica
Escuela Técnica Superior de Ingeniería Industrial

TRABAJO FIN DE MÁSTER

Clasificación de partículas de alúmina en recubrimientos APS mediante SEM: vista superiores y secciones

Classification of sprayed alumina particles in APS coating by SEM: top views and sections

Titulación: Máster Universitario en Ingeniería Industrial
Autor: Jesús García López
Director: Jose Andrés Moreno Nicolás

Cartagena, September 15, 2018

Contents

List of Figures

List of Tables

Chapter 1

Introduction

1.1 Introduction

Thermal spraying is a process in which a protective coating is applied on a substrate by spraying on it small, from 10 to 100 μm, and high-velocity, above 100 m/s, molten particles of metals, alloys or ceramics which coalesce and solidify after impact to form a dense layer. Such coatings are used to protect mechanical parts from corrosion, erosion and heat. Their failure during operation can leave components exposed and create the risk of catastrophic breakdown [1].

Adhesion of the coatings to the substrate and residual stresses generated at the interface are the main characteristics, which influence the global behaviour of the obtained structure [2].

The quality of the spray coating is mainly determined by the conditions of the impacting particles such as size, velocity, temperature, and phase, as well as the substrate conditions, such as thermophysical properties, surface roughness, wetting ability, temperature, and contact resistance. Therefore, it is necessary to develop a good understanding of the fundamental physical principles governing droplet spreading and solidification so that the correlation between the process parameters (gas velocity and temperature, substrate temperature and thermophysical properties, powder size and materials) and the properties of the splat can be established and the coating quality can be controlled [3].

1.2 State of the science

1.2.1 Surface technology and thermo-chemical treatment of surface

In recent years, machining parts must sustain increasing mechanical, thermal and chemical loads to improve their operational behaviour and reliability. Current constructive materials like steels, cast iron, light metals and polymers cannot withstand this increasing operation loads. On the other hand, materials like ceramics, hard metals, cermets, which are a combination of ceramics and metals, or pure metals with superior qualities which would be able to realize these loadings, are either not available in the demanded amounts, in general too expensive, or finally difficult to machine, e.g. concerning standard manufacturing processes.

Therefore, surface technology processes are an ideal tool to improve the functionality of high loaded machining components, meaning the creation of a load adapted surface, e.g. concerning tribological, thermal or corrosive loads, whereas the substrate material fulfil the demands on geometry and mechanical stability. In this case, a load optimized, tailored layer composite is manufactured.

Figure 1.1 shows a schedule of the layers under the surface. The machining process can form a hardened layer over the bulk material. Over the hardened layer appears a "Beilby layer", which results from flow and bond of a molecular layer in the surface because of the machining process.

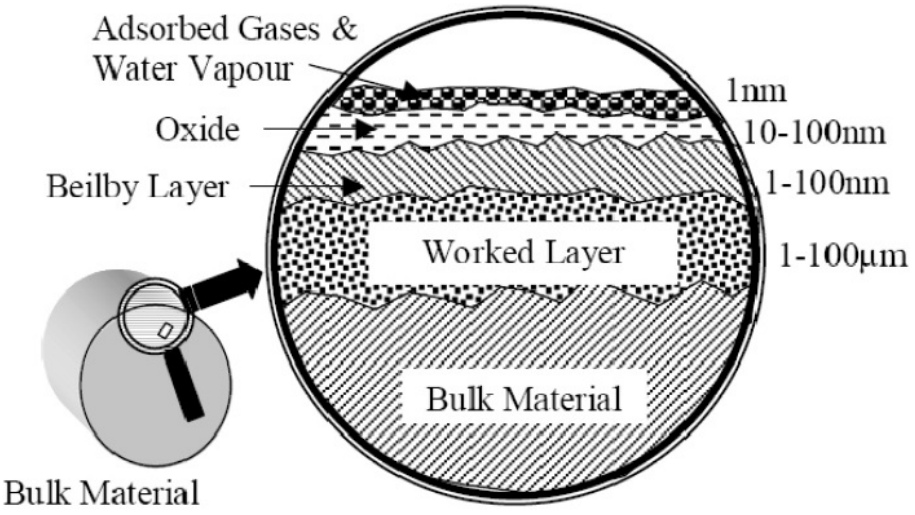

Figure 1.1: Layers distribution under the surface [4]

An option to reinforce the surface of metallic components is a local modification of the material by means of thermo-mechanical or thermo-chemical processes on the surface. In all the cases the superficial resistance and the hardness are increased by means of a modification of the crystalline network like defects generation.

In the case of thermal processes in the surface of components with Fe - C alloys, this is hardened by means of a heating (1000 - 1200 °C) and cooled fast later; originating a martensitic crystal structure where the carbon atoms are dissolved in the crystalline network.

Between these we can mention:

- Hardening by means of flame.
- Hardening by immersion.
- Hardening by induction.
- Hardening by means of electrical conduction.
- Hardening of high energy like laser or electron beam.

In the case of the thermo-chemical processes, non-metallic elements, like C and N, or metallic ones, like Cr, Al and Si, are spread in a substrate helped by a high temperature.

Between these we can mention:

- Without additional heat treatment:
  - Aluminizing.
  - Boronizing.
  - Chrome plating.
  - Nitro carburizing.
  - Nitriding.
  - Siliconizing.
- With additional heat treatment:
  - Carburizing.
  - Boronizing.
  - Nitro carburizing.
  - Chrome plating.

1.2.2 Material deposition process

In the case of material deposition, an additional coating layer, ranging from some nanometres up to several millimetres, is deposited on the component surface. A good

bonding between substrate and coating material is important for the functionality of de layer composite. Regarding the physical state of the coated material, the material deposition processes can be classified into different groups:

- Liquid state, e.g. lacquering processes.
- Solid state, e.g. electrostatic coating or thermal spraying processes.
- Gaseous state, e.g. Physical Vapour Deposition (PVD) and Chemical Vapour Deposition (CVD) processes.
- Ionized state, e.g. electroplating and galvanic processes.

Thermal spraying is a group of coating processes in which metallic and non-metallic materials are deposited in a molten or semi-molten state on a prepared, activated substrate surface. The activation prior to the coating process, i.e. removal of impurities and chemical reaction layers, as well as magnification of the specific surface, improves the bonding strength of the layer composite. The standard activation process for thermally sprayed coatings is a grit blasting process. Thermal spraying processes are being practiced since the early 1900's when Dr. Schoop introduced the technology using a combustion flame as heat source. The usual coating thickness ranges from 50 - 250 μm, for special applications also up to several millimetres. The economic benefits of thermal spraying processes are the relatively low equipment and operation cost, the relative simple handling mechanism and the relative harmless environmental impacts. Practical solutions to a specific problem frequently follow a well-established sequence of events:

- Problem analysis.
- Specification of coating properties.
- Proposed solution, including selection of materials to be sprayed, equipment and technique used.
- Application of coating.
- Analysis of results in terms of technical performance and economic viability.

Regarding the energy source [4], the thermal spray techniques are classified:

- Combustion.
  - Flame spray (FS).
    - Powden.
    - Wire.
  - High velocity oxygen fuel (HVOF).
    - O_2 + combustible gas (HVOF - G).

    - O_2 + combustible liquid (HVOF - K).

- Electrical.
  - Plasma Spray.
    - Specific atmosphere (IPS, VPS, SPS).
    - Atmospheric plasma spray (APS).
    - Special process (HPPS, WSPS, RPS, UPS).
  - Wire arc spray.
- Cold spray process.
- Laser.

Oxy-fuel flame is the oldest thermal spraying technology, an external combustion flame is generated using a mixture of oxygen and fuel gas, normally acetylene. The powder or wire materials are molten in the flame and accelerated to the substrate material. To increase the particle velocity, compressed air can be added.

Figure 1.2 shows comparison between the velocity and temperature of the sprayed particles of different procedures.

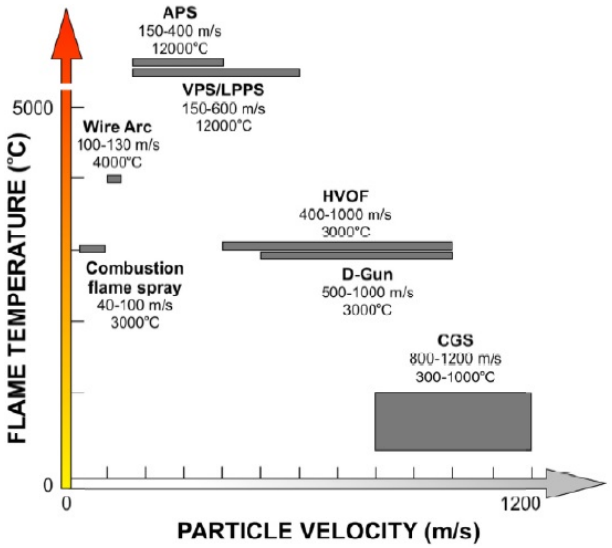

Figure 1.2: Comparison between the velocity and temperature of the sprayed particles of different procedures [5]

HVOF spraying processes differs from conventional flame spraying in that the combustion process is internal and the gas flow rates and pressures are much higher, therefore generating extremely high particle velocities.

The combination of high gas flow rates and high combustion pressure leads to the generation of a supersonic gas jet with characteristic shock diamonds.

At first, a wide range of gaseous fuels like hydrocarbons mixed with oxygen are currently used, e.g. propylene, propane, ethane or acetylene. Nowadays HVOF spraying systems use liquid fuels, generating lower combustion temperatures but much higher impact velocities, due to the increased oxygen gas flow rates. Typical coating materials deposited by HVOF spraying are cermets, but also pure metallic and low melting ceramic coatings (TiO_2) are used.

The use of a wire material represents a cost-effective and air-efficient alternative to powder flame spraying producing metallic coatings due to the lower cost of feedstock materials, the lower gas consumption, the higher spray rate and the higher deposition efficiency. Generally, wires are used for pure metals and metal alloys. Furthermore, the handling, storage and operation using wires are somewhat easier and simpler than by using powder feedstock materials.

The plasma spraying process uses a DC electric arc to generate a stream of high temperature ionized plasma gas, which acts as heat source. The arc is struck between a tungsten cathode and a copper anode within the torch. The torch is fed with a continuous flow of inert gases which are ionized by the DC arc and transferred in the plasma condition. The coating material, in powder form, is carried in an inert gas stream into the plasma jet where it is molten and propelled towards the substrate. Due to the high thermal energy of the plasma jet, materials with high melting points can be deposited. A schematic drawing of the atmospheric plasma spraying process is shown in Figure 1.3.

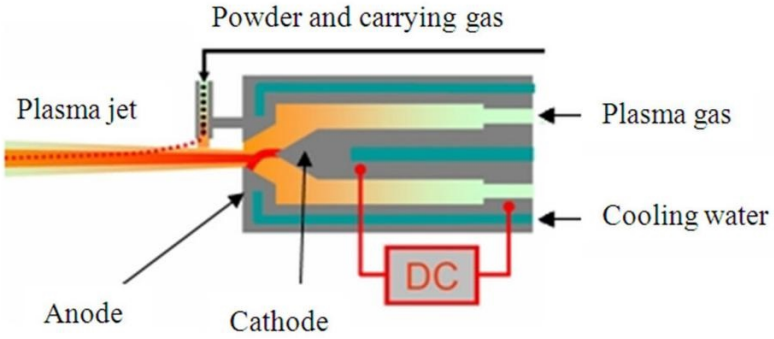

Figure 1.3: Schematic drawing of the Atmospheric Plasma Spraying process (APS) [6]

The wire arc spray coating process offers several attractive features compared to other coating processes, such as use of wires as the feedstock material, relatively simple equipment requiring no water-cooling and only low voltage power supplies. Arc spraying processes use electrical energy to create an arc that heat and melt two consumable wires electrodes. By using an atomizing gas stream the molten material is removed from the wire tips, accelerated and propelled towards the component surface to be coated.

The wire arc spraying has the highest deposition rate of all thermal spraying processes. Typical coating materials deposited by wire arc spraying are zinc, aluminium, steel and their alloys.

Figure 1.4 shows a schematic drawing of the wire arc spraying process.

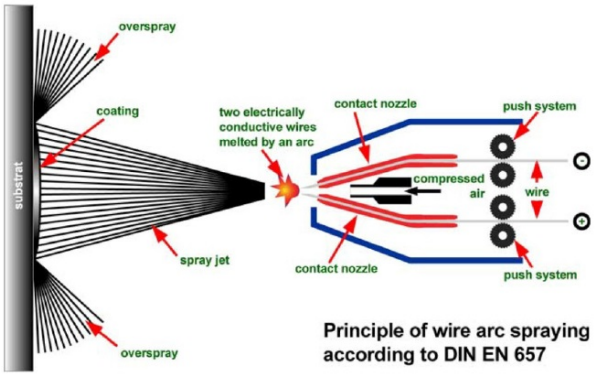

Figure 1.4: Schematic drawing of the wire arc spraying process (WAS) [7]

1.2.3 Coating materials

The characteristics of powder and wire material used for thermal spraying have a large influence on the coating quality. Powder materials are usually in the range from 5 - 200 μm, depending on the thermal spraying process. Morphology, composition and finally raw material cost can be varied by the manufacturing process.

Figure 1.5 shows a control system gas.

Figure 1.5: Control system gas [IFKB]

In Figure 1.6 we can see a power supply for APS process.

Figure 1.6: Power supply for APS process [IFKB]

Figure 1.7 shows the different kinds of powder particles used in thermal spray processes.

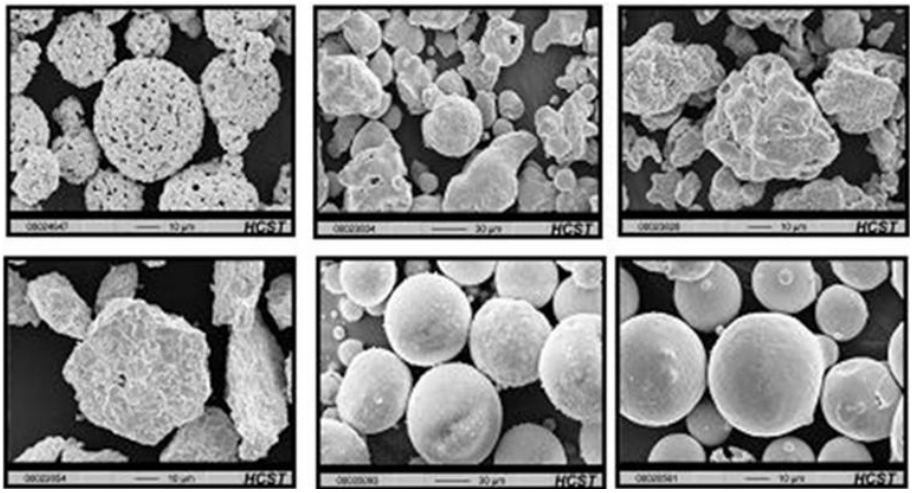

Figure 1.7: Types of powder particles used in thermal spray processes [4]

The characteristics that define the powder material concretely are:

- Chemical composition.
- Phase composition.
- Manufacturing process.
- Grain size and distribution.
- Morphology.
- Flowability.

- Apparent density.

The coating reliability depends on a good characterization of raw material powder and wire, and on the coating. The useful parameters to characterize the coating are:

- Coating structure.
  - Hardness.
  - Porosity/cracks.
  - Adherence.
  - Phases/element distribution.
- Chemical composition.
- Thermal and physical properties.
  - Thermal strain coefficient.
  - Conductivity (λ).
  - Specific heat (C_p).
- Mechanical properties.
  - Hardness (HV).
  - Youg's modulus (E).
  - Yield stress (S_y).
  - Ductility.
- Residual stress.

1.2.4 Process parameters

As this project deals with APS coating, this section is dedicated to the process parameters of this type of spray.

It is possible to consider the following parameters:

- Electric power.
- Electrodes geometry.
- Plasma stabilization.
- Coating material.

- Thermal spray conditions.

The gases used are listed below:

- Argon.
- Mixture of hydrogen and argon.
- Mixture of argon and helium.
- Mixture of argon and nitrogen.
- Nitrogen.
- Mixture of nitrogen and hydrogen.

The election of the gases is subject to the capacity of melting the sprayed particles. This capacity is bigger for molecular gases, especially hydrogen, due to its high thermal conductivity, higher than the atomic gases. On the other hand, the stream of the monatomic gases reaches higher velocity. The mixture of monatomic and molecular gases ensures the correct fusion of the particles at a high spray velocity. Helium is used as additive (in argon) because of its high thermal conductivity, but also because it causes a narrow spray cone. The usual flow is about 40-50 NLPM, although in some cases it surpasses 80 NLPM. Electric power is up to 60 kW in typical plasma torches, but can reach more than 100 kW.

The tip of the cathode varies depending on the working gas. The form and diameter of the anode influence the plasma flow pattern, by determining the distribution of the plasma temperature and jet velocities. The electric arc "contacts" the anode and cathode in one or more places, called "roots", resulting in deterioration and wear. Plasma stabilization is usually achieved by using a sheath or vortex of working gas. In some facilities, the water vortex is used to limit the arc [8].

Coating material can be classified attending to:

- Production method.
- Chemical composition.
- Physical properties as density, melting point, latent heat of fusion and pressure of vapour.
- Particle morphology.
- Size distribution.
- Particles size.

The powder feeder can be one of these devices: Gravity-based, fluidized-bed, rotating wheel, vibration-based. The usual powder feed rate typically ranges from 50 to 100

g/min, but can reach 200 g/min.

The injection angle is usually 90 degrees although sometimes is 60 degrees backwards or downwards of the plasma jet. This injector can be located inside the nozzle for refractory materials or in the outside. The length and diameter of the opening nozzle affect injection velocity of the spray.

Powder carrier gas flow ranges from 3 to 10 NLPM.

The spray distance is usually in the range 60 to 130 mm; spray angle is generally 90° although it can change by geometric requirements. Spray atmosphere is air [8].

The substrate can be classified attending to:

- Chemical composition.
- Surface treatment.
- Substrate wrapping.
- Substrate temperature.

1.2.5 Alumina phases and grain morphology

As reviewed by Levin and Brandon [9], alumina exists in many metastable polymorphs besides the thermodynamically stable $\alpha - Al_2O_3$ (corundum form). The metastable Al_2O_3 structures can be divided into two broad categories: a face-centered cubic (FCC) and a hexagonal close-packed (FCP) arrangement of oxygen anions. The Al_2O_3 structures based on FCC packing of oxygens include γ, η (cubic), θ (monoclinic), and δ (either tetragonal or orthorhombic), whereas the Al_2O_3 structures based on FCP packing are represented by the α (trigonal), κ (orthorhombic), and χ (hexagonal) phases. Some additional Al_20_3 phases have also been identified. [10]

The Al_2O_3 structures based on FCC packing are obtained by the following processes:

$$\gamma\text{AlOOH(boehmite)} \xrightarrow{300-500^\circ\text{C}} \gamma \xrightarrow{700-800^\circ\text{C}} \delta \xrightarrow{900-1000^\circ\text{C}} \theta \xrightarrow{1000-1100^\circ\text{C}} \alpha - Al_2O_3$$

$$\alpha - \text{Al(OH)}_3\text{(bayerite)} \xrightarrow{200-300^\circ\text{C}} \eta \xrightarrow{600-800^\circ\text{C}} \theta \xrightarrow{1000-1100^\circ\text{C}} \alpha - Al_2O_3$$

$$\text{Amorphous (anodic film)} \rightarrow \gamma \rightarrow \delta \rightarrow \theta \rightarrow \alpha - Al_2O_3$$

$$\text{Melt} \rightarrow \gamma \rightarrow \delta, \theta \rightarrow \alpha - Al_2O_3$$

The Al_2O_3 structures based on FCP packing are obtained by the following processes:

$$\alpha\text{AlOOH(diaspore)} \xrightarrow{700-800^\circ\text{C}} \alpha - Al_2O_3$$

$$\gamma - \text{Al(OH)}_3\text{(gibbsite)} \xrightarrow{150-300^\circ\text{C}} \chi \xrightarrow{650-750^\circ\text{C}} \kappa \xrightarrow{1000^\circ\text{C}} \alpha - Al_2O_3$$

$$5Al_2O_3 \cdot H_2O(\text{tohdite}) \xrightarrow{700-800^\circ C} \kappa' \xrightarrow{750^\circ C} \kappa \xrightarrow{900^\circ C} \alpha - Al_2O_3$$

$$\text{Vapor(CVD)} \rightarrow \kappa \rightarrow \alpha - Al_2O_3$$

As above mentioned, corundum is the thermodynamically stable phase of coarsely crystalline aluminium oxide.

Liquid Al_2O_3 exhibits $\gamma - Al_2O_3$ like coordination, which leads to the possibility of the formation of $\gamma - Al_2O_3$ prior to the formation of the stable $\alpha - Al_2O_3$ during rapid solidification. The octahedral aluminium sites found in crystalline $\alpha - Al_2O_3$ occur only at the 2 % level in liquid alumina [11].

Liquid alumina, with a density of about 2.8 g/cm^3 at its melting point, has a significant volume change during the solidification. [12]

The γ phase has lower density than the α phase (at room temperature, they are of about 3.66 and 3.99 g/cm^3, respectively), resulting in the highest volume contraction for α phase upon solidification.

Levi et al. [13] models predicting the thermal history of alumina powders electrohydrodynamically atomized gave the following results: at approaching 105 K/s, there is amorphous phase formation; at somewhat lower cooling rates, the metastable $\gamma - Al_2O_3$ can be formed directly from the melt and; at cooling rates in the range of 1-100 K/s, only $\alpha - Al_2O_3$ forms.

The surface where alumina will grow is important too. The study by Ashenford et al. [14] shows that α phase can grow on the template of a single crystal r-plane sapphire substrate but not on steel substrates. Sapphire possesses the same corundum type structure.

The cracks present in the lamellas of Figure 1.8 are a mixture of a complex stress released principally because the cooling process: differential shrinkage between the coating and substrate and a differential volume reduction from the three distinct coating phases - γ, amorphous and α.

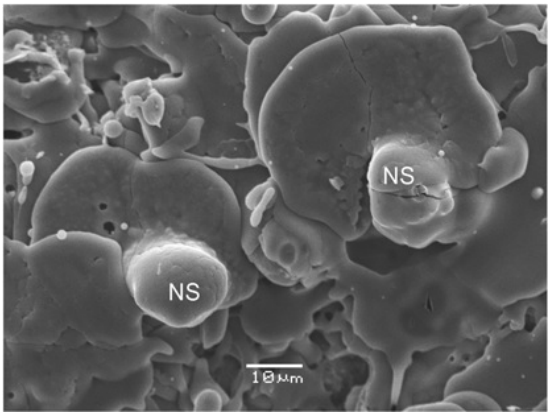

Figure 1.8: SEM image from the top of a coating. NS: not spread [10]

In order to study the phases in a splat, particles where sprayed on water, Figure 1.9.

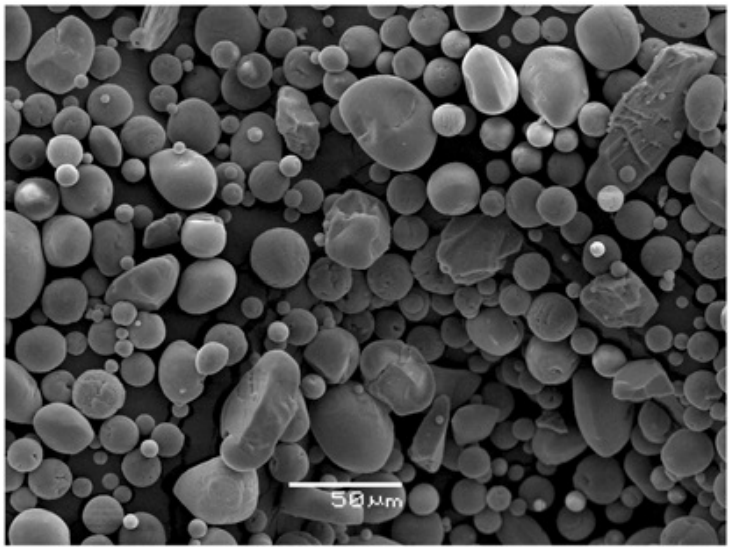

Figure 1.9: SEM image from alumina particles collected in water [10]

As can be observed in Figure 1.10, the phases present in the coating and in the feedstock captured in water are quite different. The coating presents predominantly γ and amorphous phases, while the particles captured in water is practically all α phases. The broad hump in the coating diffraction between 20 and 50 degrees of 2θ is a common indication of the presence of the amorphous phase. Gualtieri et al. [15] found for a plasma sprayed alumina coating about 84 wt % of γ phase, 12 wt % of amorphous phase and 3.7 wt % of α phase.

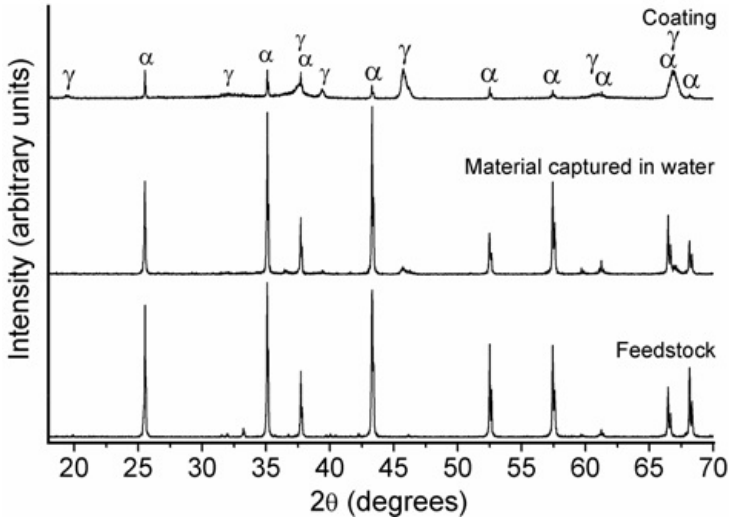

Figure 1.10: X-ray diffraction (XRD) patterns of the alumina feedstock, of the particles collected in water and of the coating [12]

Under real quenching conditions in liquid water, the particle is assumed to be in contact both with the liquid and the boiled water. Then, the values of the heat transfer

coefficient during a higher stand-off distance and in water could be low enough to lead to solidification with cooling rates in the range of where only α phase forms.

Amorphous phase could be formed during higher cooling rates at the front area of the deposition. When a particle starts its deposition against the substrate, at the start, it experiences a very high heat transfer, which could lead to the presence of the amorphous phase, but during the deposition, somewhat lower cooling rates occurs because of the presence of the γ phase. Li et al. [16], with a HOVF process conclude that high velocity splat of alumina quenching on smooth aluminum, steel and silicon substrates results in suppression of crystallization yielding a predominantly amorphous splat.

If the cooling rate determines the grain width, the front area of the deposition has the highest cooling rates and the lowest grains width. Chraska and King confirmed this for a plasma sprayed zirconia splat. [17]

Then, the zones of not spread material above the splats observed in Figure 1.9 could help to form some $\alpha - Al_2O_3$ or more helpful in forming γ phase than the formation of the amorphous one.

The line profile analysis from the XRD spectrum of the coating reveals a medium crystallite size of 18 nm for γ phase. Meanwhile, α one gave size of about 116 nm. These results are not very precise, because the single-line analysis gives good results in the crystallite size range of 50 and 100 nm. But the broadening in the XRD peaks indicates small crystallite sizes and γ phase gives peaks which are broader, so it has a smaller crystallite size than α one.

In the coating, the presence of the amorphous phase and the small crystallite sizes confirm that the cooling rate could have very high values. Both the presence of amorphous and γ phases confirm inhomogeneous cooling rate during deposition.

The cooling rate of the particles during thermal spray deposition is affected by their temperature and heat drainage to the substrate. With an increase of the spraying power there is an increase in the temperature of the particles and this is expected to lead to a decrease in the presence of α phase in the coating.

To increase the phase content in a thermal spray coating for a specific substrate it is necessary to reduce the spraying power deposition, which according to Zhang et al. [18], decreases the efficiencies, increases porosity and could reduce residual stresses.

Figure 1.11 shows two types of alumina splats on glass and stainless steel substrates at 20 °C. [19]

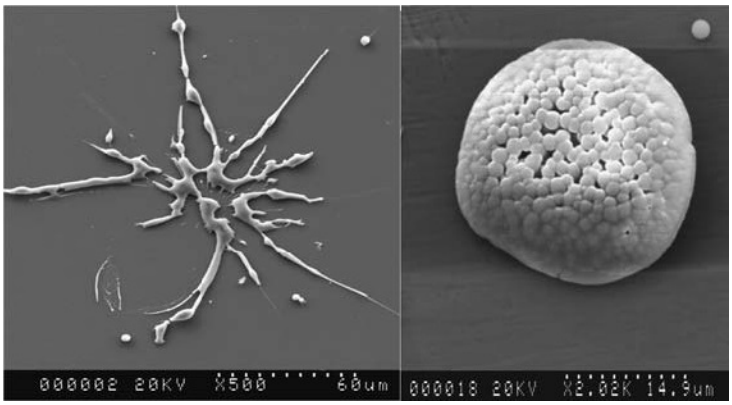

Figure 1.11: Two types of alumina splats on glass (left) and stainless steel (right) substrates at 20 °C [19]

As for the grain morphology, Figure 1.12 illustrates the front morphologies depending on the temperature gradient (G) in the liquid phase just ahead of the advancing solid–liquid interface and on the solidification velocity (V_s).

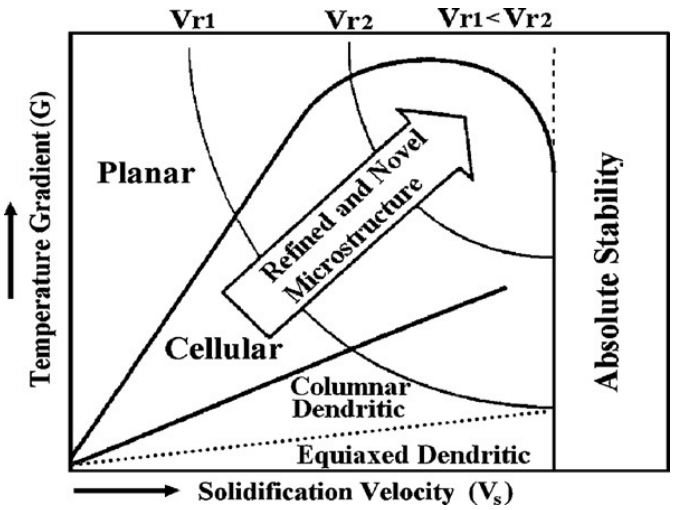

Figure 1.12: Dependence of solidification morphology on temperature gradient and solidification velocity [20, 21]

Table 1.1 shows the spray parameters used to obtain the splat in the Figure 1.13, formed on mirror-polished substrate preheated at $T_s = 200$ °C. Figure 1.14 is a detail of the former figure.

Table 1.1: Spray parameters [22,23]

Plasma torch	F4-VB
Torch nozzle diameter	6
Plasma gas (l/min)	80 (Ar), 10 (H_2)
Arc current (A)	600
Voltage (V)	66
Spray distance (mm)	140
Carrier gas mass flow rate (l/min)	3
Powder feeding rate (g/min)	30

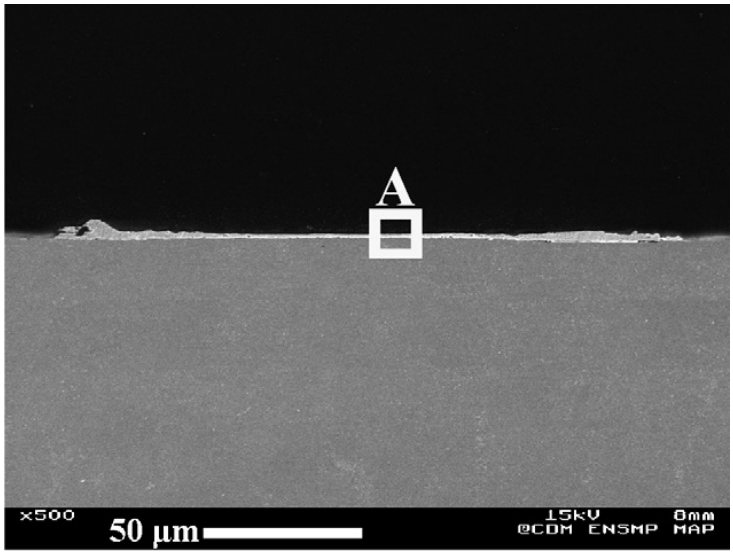

Figure 1.13: Cross section of an etched splat [24]

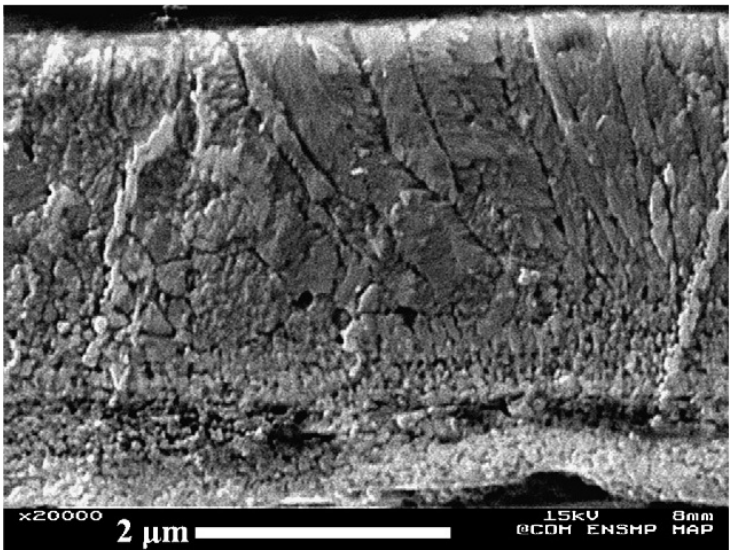

Figure 1.14: Magnification of area A of Figure 1.13 [24]

Figures 1.15 and 1.16 show the effect of temperature substrate.

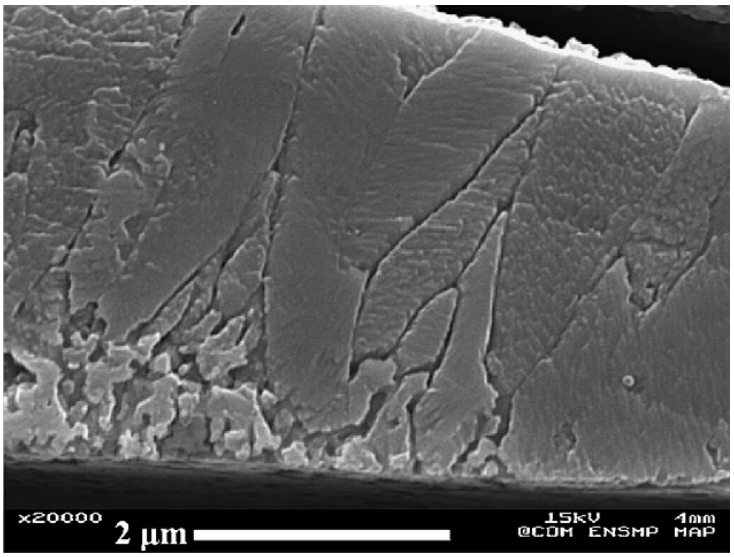

Figure 1.15: Splat section formed on substrate preheated at $T_s = 250$ °C [24]

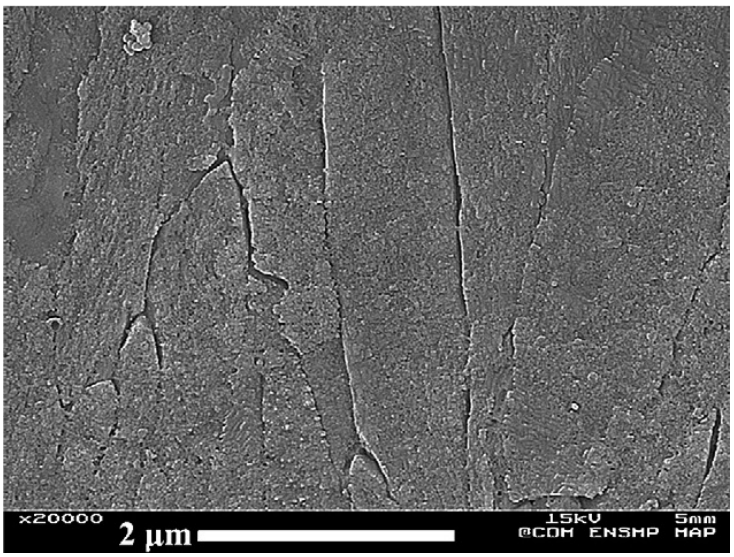

Figure 1.16: Splat section formed on substrate preheated at $T_s = 300$ °C [24]

Chraska and King [25] have related the splat's columnar width with the undercooling (ΔT). More specific, the splat's cross-sectional columnar width, d, has been determined as [25]:

$$d = \sqrt[3]{\frac{8 \cdot u}{\pi \cdot J}}$$

where u and J are the solidification rate and nucleation rate respectively.

The solidification rate is calculated by

$$u = \alpha \cdot \omega \cdot e^{-\frac{Q}{k_B \cdot T}} \cdot e^{1-e^{-\frac{\Delta G_V}{k_B \cdot T}}}$$

where α is the interatomic spacing, ω the atomic vibration frequency, Q the activation energy for an atom to transfer across the solid–liquid interface, k_B the Boltzmann's constant and ΔG_V the driving force for solidification. ΔG_V has been approximated as

$$\Delta G_V \simeq L \cdot \Delta T_r$$

where L is the latent heat of fusion, $T_r = T_m - T/T_m$ the reduced undercooling and T_m is the melting temperature. The atomic vibration frequency ω can be calculated by

$$\omega = \frac{k_B \cdot T_m}{h}$$

where h is the Planck's constant.

The nucleation rate is calculated by:

$$J = n \cdot \omega \cdot e^{-\frac{Q}{k_B \cdot T}} \cdot e^{e^{-\frac{16 \cdot \pi \cdot \sigma^3 \cdot f(\theta)}{3 \cdot \Delta G_V^2 \cdot k_B \cdot T}}}$$

where n is the nucleation site density, σ the surface tension, $f(\theta)$ is a function of the contact angle, θ, for a solid nucleus on the substrate surface. The function of the contact angle can be approximated as

$$f(\theta) = \frac{2 - 3 \cdot cos(\theta) + cos(3 \cdot \theta)}{4}$$

Finally, the columnar width can be written as

$$d = \sqrt[3]{\frac{\alpha \cdot \omega \cdot \left(1 - e^{-\frac{L \cdot \Delta T_r}{k_B \cdot T_m}}\right)}{n \cdot \omega \cdot e^{-\frac{16}{3}} \cdot \frac{\pi \cdot \sigma^3 \cdot f(\theta)}{L^2 \cdot \Delta T_r^2 \cdot k_B \cdot T_m}}}$$

The columns' mean width (d) was measured by image analysis and the undercooling was calculated for each substrate temperature by using the last formulation of d. In order to do the calculation, it was assumed that in the case of metals, α is $5 \cdot 10^{-10}$ m [26] and the product, $n \cdot \omega$, is 10^{42} $m^{-3} \cdot s^{-1}$ [27].

Results are shown in Table 1.2 and they confirm that the splats' cooling velocity was decreased with the increase of the substrate temperature above the transition temperature, T_{tr}.

Table 1.2: Mean width of columns of splats formed on mirror polished substrates and their undercooling [24, 27]

Substrate temperature T_s(°C)	Mean columns's width (μm)	S.D. (μm)	Undercooling ΔT(°C)
200	0.82	±0.08	792
250	0.95	±0.07	375
300	1.15	±0.07	249

Table 1.3 shows the width of splats columns and their undercooling.

Table 1.3: Mean width of splats' columns (d) and their undercooling (ΔT) [28, 29]

Substrate roughness R_a (μm)	0.02			1.33		
Substrate temperature T_S ((°C))	200	250	300	200	250	300
Columns' mean width d (μm)	0.82	0.95	1.15	1.02	1.08	1.44
S.D. (μm)	±0.08	±0.07	±0.07	±0.07	±0.07	±0.07
Undercooling (ΔT)	792	375	249	304	276	192

1.2.6 Splat morphology

As regards as the morphology of the splats, the dependence of the fraction of disk-shaped splats both on the substrate temperature and ambient pressure is summarized schematically [30] in Figure 1.17, as a 3D transition curve.

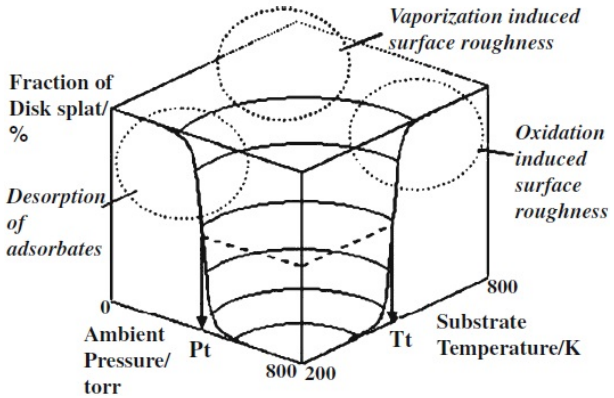

Figure 1.17: Three-dimensional transition map of flattening behaviour in the thermal spray process [30]

Figure 1.18 shows zirconia splats collected on a stainless-steel substrate, with a mean substrate roughness, R_a, lower than 0.05 μm and a temperature, T_s, around 300 (°C).

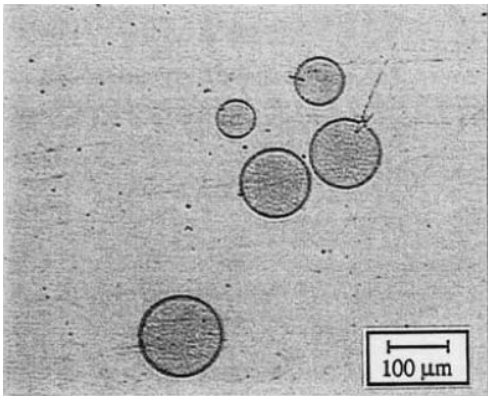

Figure 1.18: Zirconia splats on stainless steel substrate [31]

Atomic Friction Microscope (AFM) allows the observation of details in the 0.1 μm size or less, such as the columnar structure of the splat or details of a crack or rim, Figure 1.19.

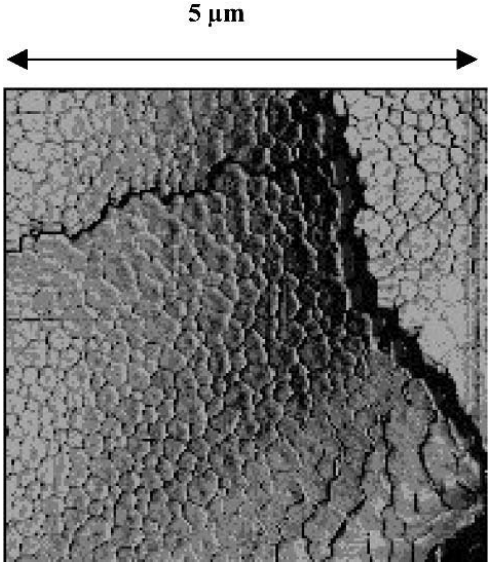

Figure 1.19: Columnar structure within a small area (5 x 5 μm^2) of a splat presented in Figure 1.18 [32]

One way to evaluate the splat morphology is by the shape factor (SF), which is defined by the dimensionless parameter:

$$SF = \frac{4 \cdot \pi \cdot S}{P^2}$$

where P is the perimeter of the splat and S its surface. For a disk-shaped splat, $SF = 1$ and SF decreases when the splat is jagged.

Figure 1.20 shows the morphology of plasma sprayed alumina particles based on their velocity and temperature prior to impact.

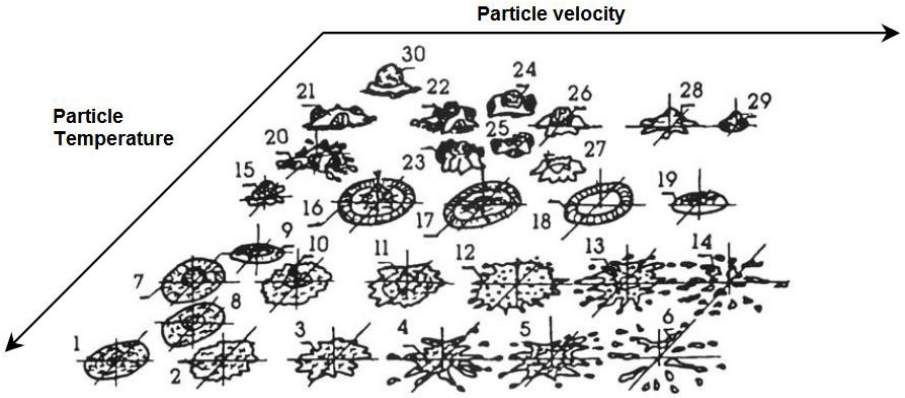

Figure 1.20: Morphology of plasma sprayed alumina particles based on their velocity and temperature prior to impact [33]

1.2.7 Splat flattening

Several review papers [34-38] present different analytical models of splat formation. In the event of droplet impact perpendicularly to a smooth substrate without solidification, the splat solidification is assumed to start only when flattening is completed.

As regards of splats size, under typical thermal spray conditions, surface energy is negligible in comparison to kinetic energy, and the spread factor (flattening degree), ξ, is defined as D/d_p, where D is the diameter of the splat, assumed to be cylindrical and d_p is the diameter of the impacting droplet.

ξ becomes a function of Re alone, which quantifies the viscous dissipation of the inertia forces:

$$\xi = a \cdot Re^b$$

where a and b are constants.

The current values for these constants are typically ranged from 0.5 to 1.2941 for a and 0.125 to 0.25 for b. [39] Madejski uses 1.29 for a and 0.2 for b. [40] According to different authors, a varies between 0.8 corresponding to the mean diameter of an extensively fingered splat and 1.2941 for disk-shaped splat, and b is either 0.2 or 0.125 or 0.167. [36]

Analytical and numerical investigations by different groups are summarized in the papers of Kang and Ng [40] and Vardelle et al. [41]. Works in this field have also been performed by Amada et al. [42, 43] and Liao et al. [44].

If the droplet is freezing as it spreads, the maximum spread diameter may be reduced. The effect of solidification in restricting droplet spread is modelled by assuming that all the kinetic energy stored in the solidified layer is lost. If s^*, calculated by s/d, where s is the solid layer thickness, is the dimensionless solid layer thickness when the

droplet has spread to its maximum extent. The maximum spread factor is [45]:

$$\xi = \sqrt{\frac{We + 12}{\frac{3}{8} \cdot We \cdot s^* + 3 \cdot (1 - cos\theta) + 4 \cdot \frac{We}{\sqrt{Re}}}}$$

where

$$Re = \frac{\rho \cdot v_d \cdot d}{\mu} \qquad We = \frac{\rho \cdot v_d^2 \cdot d}{\sigma}$$

Professor Jan Madejski initiated the analysis of the splat in a rigorously scientific way. He formulated a theoretical model on the impact of a molten droplet with a solid substrate by making a relationship between the splat diameter (D) and the diameter of the initial droplet (d).

$$Re = \frac{d_p \cdot v_p}{\nu_p}$$

$$\xi = 1.2941 \cdot Re^{0.2}$$

Where ξ is the degree of spreading, D/d_p, d_p is the particle diameter prior to impact, D is the final diameter of the splat, ν_p is the viscosity of particle prior to impact and v_p is the velocity of the particle at impact.

His model is an excellent introduction to understand particle deformation and it has been refined by different authors to integrate the real conditions of thermal spraying:

- Particle wetting of the substrate and thermal contact resistance.
- Substrate roughness.
- Spraying at angles different from normal.
- Particle oxidation at splashing.
- Particular features of the splat formation from submicrometric or nanometric particles.

The Madejski's model considers an ideal contact between the substrate and the lamellae, R_{th}=0. The values of R_{th} in the range $10^{-7} - 10^{-8}$ K/W, considered very low, can increase during the lamellae flattening. High values of R_{th} increase the solidification time and this may increase flattening of the lamellae. Quantification of the wetting effect is difficult because of the low precision of available data at high temperatures.

Subsequent studies show that with values of the exponent from 0.2 to 0.25 in the Madejski's model, the flattening degree of ceramic particles will be remarkably underestimated. Li's results revealed that only an exponent close to 0.1 can be applied to assess particle splashing [46]. Therefore, as a general formula to predict the flattening degree of spray molten droplet, the equation found to be more suitable is:

$$\xi = 1.21 \cdot Re^{0.125}$$

As for plasma-sprayed alumina coatings deposited by the powder with a mean particle diameter of 20 μm, previous Li's study showed that the mean lamellar thickness under a typical deposition condition was 1.75 μm [47]. This result corresponds to a flattening degree of 2.76.

In order to understand better the splat morphology, the simulation of the splat flattening must be developed. Two models have been used in the study of liquid droplet flattening: incompressible and compressible ones.

For incompressible models, upon impact, the liquid droplet can rebound, deposit, or splash, at least partially. This splashing corresponds to the ejection of tiny droplets mostly in the impact direction. In the following it will be called "impact splashing". These phenomena are related, at least for a water or an ethanol droplet, [38,48-50] to critical values of the Sommerfeld parameter, K, of the particle at impact defined as

$$K = We^{1/2} \cdot Re^{1/4}$$

Thus, for the liquid aforementioned rebound happens when K is lower than 3, splashing when K is greater than 58 and deposition for the intermediate values.

Under plasma spraying conditions, the limit between deposition and splashing is not so precise, but the trend is the same. [50] Moreover, with alumina particles sprayed by a DC plasma jet, calculated values of K vary between 50 and 1800, [50] which means that impact splashing is more the rule than the exception.

Allen [51] has suggested that splashing may be the result of Rayleigh-Taylor instabilities that occur when a fluid accelerates into a less dense one. Models devoted to investigate droplet flattening onto a smooth surface, allowed the calculation of the flattening degree.

These models were improved by introducing the Weber number which takes into account the liquid material surface tension. In these theories, the Weber number appears as We^{-1}. However, it can be neglected, at least at the beginning of flattening, when the impact velocity v_p is high as in DC plasma spraying, supersonic RF plasma spraying, and HVOF spraying. In that case, the equation that defines ξ holds. Some theories also introduce the contact angle between liquid and solid at equilibrium that has an appreciable effect at the end of the flattening process.

For compressible models, Dykhuizen [35] and Armster et al. [38] recall that, due to their complexity, these models have only been used to study the initial impact and no results on final splat sizes have been obtained. Such calculations have shown that the maximum impact pressure of a spherical droplet is larger than the classic water hammer pressure

$$\rho_p \cdot c_l \cdot v_p$$

where c_l is the sound velocity in the liquid phase, ρ_p the density of the impacting liquid, and v_p the particle velocity at impact.

According to the review of Armster et al., [38] compressibility, characterized by the impact Mach number, v_p/c_l, governs the very first moment after a drop hits a surface. On impact, the velocity of the liquid is suddenly changed and the liquid is compressed by the wave propagating into the drop, Figure 1.21.

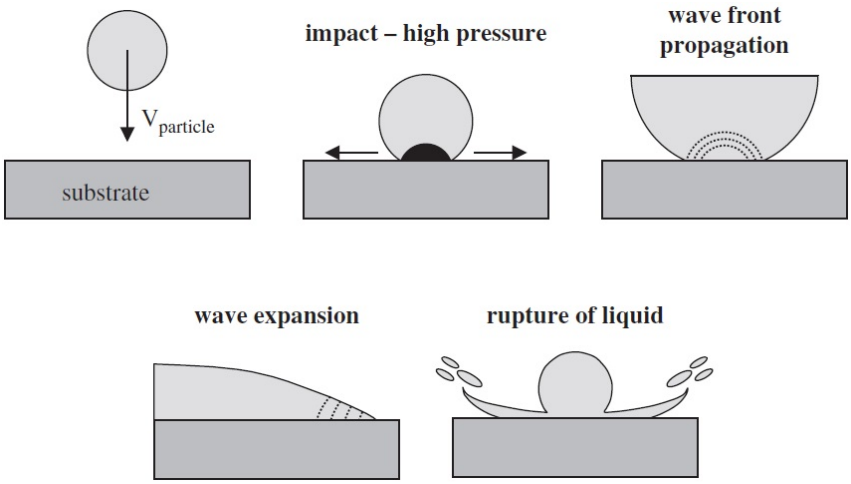

Figure 1.21: Schematic of the wave propagation at impact with the resulting impact splashing [52]

For example, for a liquid metal drop impacting at 300 m/s, ρ_l, around 8000 kg/m^3, and c_l of 3000 m/s (Ma = 0.1), the impact hammer pressure is already approximately $7 \cdot 10^9$ Pa (70 000 atm) [38]. This pressure starts to be released after a time

$$t_c \sim \frac{d_p \cdot v_p}{4 \cdot c_l^2}.$$

With a droplet radius of 20 μm, t_c is around $3 \cdot 10^{-10}$ s, which is very short compared with the flattening time, around 10^{-6} s. At that time t_c, the radius of the contact zone equals

$$r_c = \frac{d_p \cdot v_p}{2 \cdot c_l} = \frac{d_p \cdot Ma}{2}$$

In the preceeding example, r_c is 2 μm. This value has to be compared with the 20 μm of the splat radius.

In the event of droplet impact perpendicularly to a smooth substrate with solidification, as soon as it starts before flattening is completed, the flattening process is drastically modified. There are several factors which have strong influence during the flattening: cooling rate (CR), solidification process and splashing during flattening process.

The CR has been predicted using analytical or one-dimensional (1D) heat transfer models. It depends on the following effects: [53-57]

- The quality of the contact between the splat and the underlying material. A very simple model [58,59] gives the cooling velocity as

$$V_s = \frac{h \cdot T_p}{L_p \cdot \rho}$$

where L_p is the latent heat of solidification, T_p the particle temperature, ρ the density of material, and h the heat transfer coefficient at the interface.

This expression shows that h has a drastic effect on the solidification rate at the interface. Solidification generally starts at the end of the flattening process; [58-62] i.e., when surface energy becomes important. If the contact is uniform, h can be expressed in terms of the contact angle through

$$h = 0.5 \cdot h_c \cdot (1 + \cos\theta)$$

where h_c being the heat transfer coefficient for perfect wetting ($\theta = 0$).

Instead of h, the thermal contact resistance $R_{th} = 1/h$ is often used. R_{th} makes possible to quantify the quality of contact between the splat and the underlying layer. A perfect contact corresponds to $R_{th} \sim 10^{-8}$ m^2 K/W while a poor contact is about 10^{-6} m^2 K/W.

- The latent heat of fusion. This provides a heat source that needs to be compared with other sources. The Stephan number is a measure of the solidification time, and it is defined as the ratio of the sensible to the latent heat

$$Ste_s = \frac{c_{p,s} \cdot (T_m - T_s)}{L}$$

where $c_{p,s}$ is the heat capacitance of the solid phase, L the latent heat of fusion, T_m the melting temperature, and T_s the temperature of the substrate.

It is also sometimes defined for the liquid phase as

$$Ste_l = \frac{c_{p,l} \cdot (T_p - T_m)}{L}$$

where $c_{p,l}$ is the heat capacitance of the liquid phase, and T_p the impacting droplet temperature.

- The ratio of splat to substrate thermal diffusivities characterizes the CR, especially for a perfect contact.

- Lastly, a great effect is linked to splat thickness. The CR decreases drastically when the splat thickness increases. Therefore, CR will be much lower with subsonic RF plasma deposited splats than with DC plasma deposited splats. Also, CR should be higher at the periphery of the flattening droplet, provided that the contact is perfect. At the splat rim, where the contact pressure is very low and the surface tension is at a maximum, splat curling occurs and the contact of the flattening

particle with the substrate is very poor, thereby inducing a slower liquid cooling through the already solidified part of the splat and a rounded rim due to the surface tension. Outside the rim area within the splat, the contact splat-substrate is good and splat thickness is lower. Therefore, in principle, solidification would start there. However, in this area the reduced radius $\eta = 2r/d_p$ might be higher than 2. Then the contact pressure may not be sufficient to overcome the pressure resulting from flash evaporation of condensates or adsorbates at the surface and the disturbance of the spreading process by asperities and surface defects, resulting in a high local thermal contact resistance. Thus, solidification will start in an area where the flattening droplet is thinner but the impact pressure higher.

According to the high CRs achieved in plasma spraying, up to 10^9 K/s at the very beginning of the cooling process, the flattening droplet undergoes hypercooling, generally resulting in heterogeneous nucleation starting at contact with the underlying material. [57, 63-65] The rate of nucleation and crystallization can be calculated from the classic theory of nucleation when assuming a steady-state process. The critical free-energy change required to reach the critical size of embryos is linked to the contact angle that affects the lowering of the activation energy required for nucleation. Reciprocally, the experimentally observed size of the columns within splats allows the determination of the values of θ and CRs.

At the end of the flattening process, the starting solidification, especially close to the splat periphery where it is thinner, may impede the liquid flow and splashing will occur. However, it will proceed almost parallel to the substrate surface and result in extensively fingered splats. A similar phenomenon will occur when the liquid flow encounters surface asperities.

Approximate equations describing the time evolution of the splat thickness and radius during the flattening process, and taking into account the surface roughness, [66] have been proposed in the literature. It is assumed that roughness increases the shear stress due to the friction between the flattening droplet and rough surface.

A mathematical model including different geometrical asperities has been developed by Fukanuma [67] and recently improved. [68] These models show that the surface roughness promotes splashing at impact and during flattening. Splats are extensively distorted. As they are thicker (up to three times) than those obtained on smooth substrates, their CR is decreased.

For a droplet that does not undergo solidification, the Sommerfeld parameter K characterizes the phenomena at impact. Escure et al. [50, 69, 70] have investigated the deposition and splashing conditions for K values ranging between 4 and 1800. The deposited particles were alumina and the substrates, either stainless steel or alumina. The temperature of the stainless substrate was varied between 600 and 1100 K and that of alumina substrate between 600 and 2300 K. At 600 K, stainless steel and alumina substrates are over the transition temperature and corresponding to splats that exhibit no flattening splashing (disk-shaped splats). On alumina substrate at 2300 K, no solidification can

occur before flattening is completed.

In the words of Escure et al., it can be seen that the quantity of splashed droplets (in the 1 μm range) increases with K. [50] For impacting particles with a mean diameter is approximately 30 μm, splashed droplets reach heights of about 3 mm. The size of the splashed droplets is in the micrometre range and corresponds to a rather small quantity of the impacting material. Moreover, these small particles reach a distance high enough from the substrate to be outside the dynamic boundary layer and, thus, entrained by the plasma flow.

Contrary to what has been observed with ethanol droplets, [46] the transition between deposition and splashing is not exactly at $K = 57.7$. Whatever may be the substrate temperature, deposition occurs for K between 4 and 70 while splashing is observed down to $K = 10$ and is the rule for $K > 70$. This dispersion might be due to the fact that the smooth surface becomes rough after the impact of $5 \div 10$ particles and the measurement accuracy of K on the order of 30 %.

When spraying different materials on smooth substrates, R_a lower than 0.5 μm, made of different materials, the following phenomena are observed. Below a substrate temperature, linked to substrate and impacting droplet materials, splats are extensively fingered while above this temperature, they are almost disk shaped. The splat fingers corresponding to splashing parallel to the substrate surface, are termed as flattening splashing. The latter differs from the "impact splashing" defined above. The most interesting feature lies in the drastic change from fingered-splat pattern to the almost disk-shaped one at a certain narrow temperature range when the substrate temperature increases. The transition temperature T_t at which the splat shape changes was defined and introduced by Fukumoto et al. [71] The fact that the splat pattern varies with the substrate temperature has been recognized by many investigators such as, for example, Houben. [72]

When the smooth substrate, Ra around 0.05 μm, was preheated at temperature T_s higher than transition temperature, T_t, the adhesion of coatings was higher than in the event in which T_s was lower T_t. [73-76]

Figure 1.22 shows the effect of substrate temperature on the coating adhesion. The adhesion strength changes progressively with substrate temperature and corresponds quite well to that of the splat shape on a smooth substrate. Thus, investigation of the flattening mechanism of the sprayed particles is significantly meaningful for the practical use of thermal spray coatings.

The observation of bottom surfaces of splats shows that, generally, they exhibit numerous pores and rapidly solidified structures at low substrate temperature. It seems that splat solidification starts at points unevenly distributed at the bottom of the flattening particle and the resultant solidified part affects drastically the flowing behaviour of the molten part. Almost no pores can be observed with a solidification structure looking quite flat and dense over more than 50-60 % of the bottom surface of splats, at substrate temperatures higher than T_t. In the latter case, solidification occurs most likely when

flattening is almost completed. Similar observations of rapidly solidified microstructures in the bottom part of splats have been made by Safai [77] and Sampath. [78] Inada and Yang [79] suggested that the rapidly solidified layer at the bottom surface affects the flow behaviour of the upper molten part. Some numerical simulations by Mostaghimi support this hypothesis. [80] It is inferred that the rapidly solidified layer formed just after the impingement on the substrate plays an important role for the flattening process.

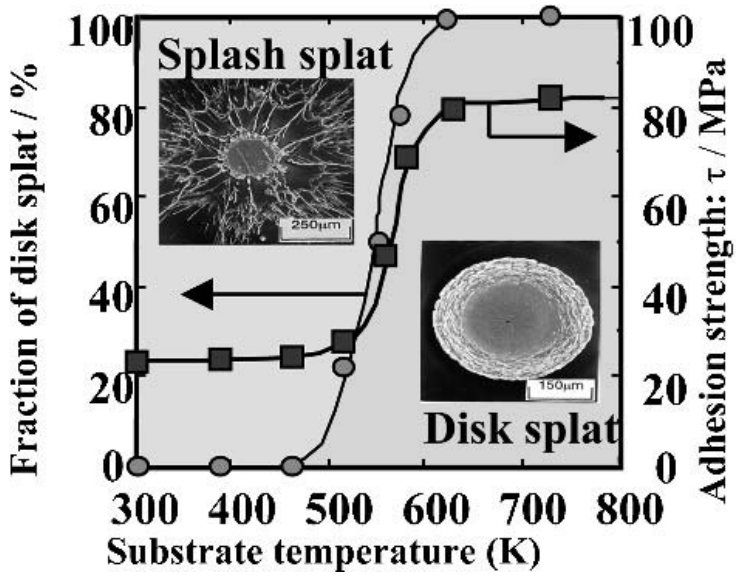

Figure 1.22: Variation of the adhesive strength of the coating with substrate temperature (Ni sprayed material with a size distribution 10-44 μm; stainless steel AISI304 substrate) [73]

Preheating a metallic substrate over the transition temperature T_t may result in the formation of an oxide layer at the substrate surface. The latter results in the formation of jagged splats and, correlatively, a decrease in coating adhesion. [31]

The most probable explanations concerning the transition temperature deal with the desorption of adsorbates and condensates at the substrate surface, wetting of the substrate by the liquid material, and solidification effects. [72-91]

The flattening behaviour and the grain or column size of the resulting splat have been observed systematically for many particle/substrate material combinations [81, 87, 92-94].

It is well known that the standard free energy of formation of the oxide layer from the metal can be closely related to the static wetting of the molten metal on the oxide substrate. [95] Here, it is assumed that this relation is applicable to dynamic wetting. The smaller standard free energy of the metal corresponds to the lower transition temperature. It is confirmed that a better wettability promotes the occurrence of disk-shaped splats.

The morphology of the resulting splat was observed, for an alumina particle DC plasma-sprayed and impinging (below the transition temperature of gold and close to

that of stainless steel) onto the boundary between a gold-coated and a naked stainless-steel substrate surface. The substrate temperature was 400 K. A half-splashed splat was observed on the gold-coated substrate, while it was half disk shaped on the naked substrate. The typical splat morphology is shown in Figure 1.23(a). Furthermore, on the naked surface, the disk splat was probably formed without any initial solidification of the splat, as shown by the corresponding missing central part on the coated substrate, Figure 1.23(b). This fact indicates that initial solidification is not always a necessary condition for flattening splashing, and the wetting affects flattening at least as much as solidification.

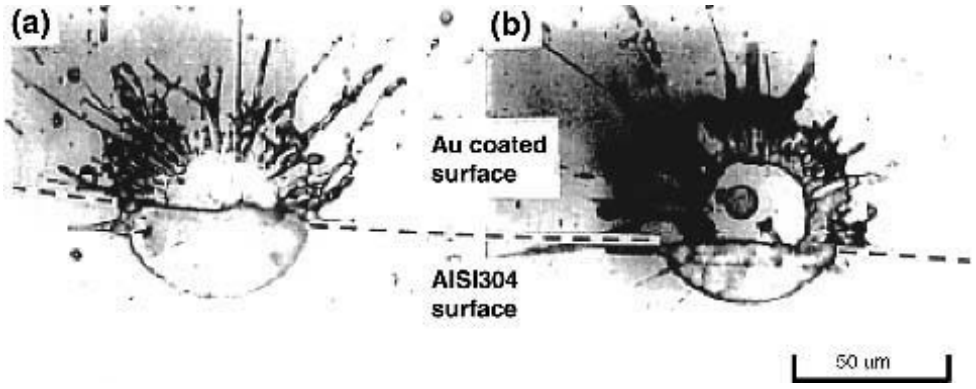

Figure 1.23: Al_2O_3 splat morphology on the boundary line between gold-coated and AISI 304 stainless steel surface: (a) half-disk shaped and half-splashed splat, (b) splashed splat without central disk. [89]

Figure 1.24 shows the variation of the thermal conductivity of plasma-sprayed oxide particles and transition temperature. The transition temperature decreases with the increase in particle thermal conductivity. Moreover, the slope of the curve is steeper when the transition temperature is higher. While the interface wettability, temperature, and viscosity of particles were different for all material couples, the linear relationship between T_t and particle thermal conductivity could be observed for each material. The linear relationship indicates that the flattening of oxide particles could be linked to the particle thermal conductivity. In addition, the gold-coated substrate exhibits the worst wetting with respect to ceramic particles; thus the higher transition temperature corresponds to the worst wetting at the splat/substrate interface. Therefore, an initial solidified layer at the bottom surface of the particle can exist even for ceramic particles and must affect the spreading of the liquid material on the surface.

The qualitative dependence of the wetting of molten droplets on substrate temperature is shown in Figure 1.25. The three curves with an upward slant to the right and the capital letters A, B, and C correspond to the variation of the wetting of different materials with substrate temperature. The rank of the curves along the y-axis corresponds to the rank of the wettability between droplet and substrate. The two horizontal lines in Figure 1.25 correspond to some critical values in wetting. That is, the lower line is related to the critical value of the wetting for the formation of splashed splats due to solidification, and the upper line corresponds to the critical value for the appearance of a disk-shaped splat.

In the case of point a on curves B and C, where wetting is lower than the lower critical value, a jagged splat is formed although no solidification occurs at the initial stage of spreading. If the wetting condition is over the lower critical value, (B and C curves, with point b corresponding to a rise of the substrate temperature, or with point c on curve A), a splashed splat with a central disk will be obtained. The central disk part in the splat grows with an increase in substrate temperature, and when the wetting condition reaches the point d on each curve, that is the upper critical value. Then the transition from a splashed to a disk-shaped splat occurs. The transition temperature increases with the droplet wetting at the interface.

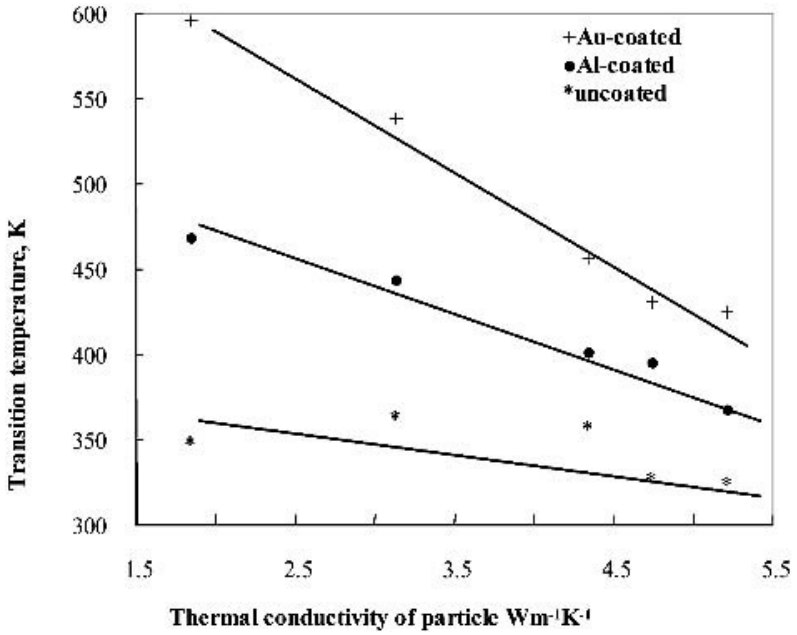

Figure 1.24: Variation of transition temperature with the thermal conductivity of impacting particle [89]

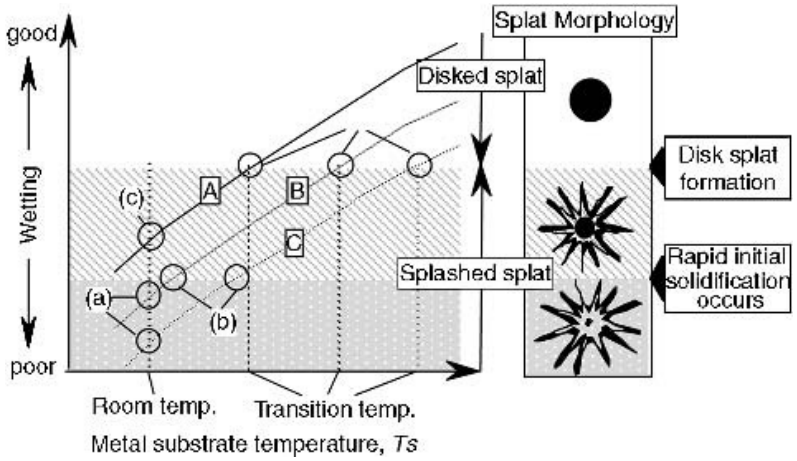

Figure 1.25: Relationship between wetting and splat pattern [89]

The solidification affects the flattening behaviour because the splat cooling depends on the heat transfer rate through the initial solidification layer between the wetting range

of both critical lines. However, the wetting at the splat/substrate interface seems to be the most dominant factor with regard to the flattening of the thermal sprayed ceramic particles.

The SEM observation of a millimetre-sized Ni splashed-splat on a gold-coated substrate shows that the gold film was torn at the location where the Ni droplet impinged, while it remained intact in the region between the central disk and the splashed material. It can be inferred from this result that splashing is not due to the liquid material flow on the substrate surface from the impact point to the periphery, but to the jetting away from the upper part of the molten spreading material.

Gougeon et al. [96] followed the surface area of a flattening molybdenum particle on a glass coupon by measuring the time evolution of its shadow using a laser attenuation method. The flattening particle area tends to increase up to a maximum that is followed by a rapid decrease by a factor of $2 \div 4$. They estimated that the liquid material enlarged to the maximum area and, when the kinetic energy is fully dissipated, shrinkage occurred due to surface tension. The flattening splashing was thought to result from this shrinkage.

Free-falling experiments were carried out as a simulation of the thermal spray process. [82, 84] The cross section of a Ni splat collected on a stainless-steel substrate at room temperature is shown in Figure 1.26(a). It exhibits an isotropic coarse grain structure, whereas on a high-temperature substrate Figure 1.26(b), it has a fine columnar structure. The mean grain size of the splat obtained on a substrate at room temperature is obviously larger than that obtained on a high-temperature substrate. This result indicates that the splat solidification rate on a substrate kept at room temperature is considerably lower than on a high temperature substrate. Similar results were obtained with splats of alumina or zirconia deposited onto stainless steel substrates. [45] The splat cooling rate is affected by the thermal contact resistance at the splat/substrate interface. [45] The latter controls the interface microstructure of the splat. For free-falling experiments similar to that of Fukumoto, measurements of the heat transfer coefficient at the droplet/substrate interface have been reported by Liu, [97] Hofmeister, [98] and Bennett. [99]

The particle effusivity is an interesting parameter in order to study the possible melting of the substrate at impact, which is defined by

$$e_p = \sqrt{\rho_p \cdot c_{pp} \cdot \kappa_p}$$

where ρ_p, c_{pp} and κ_p represent the specific mass, the specific heat at constant pressure and the thermal conductivity of the particle, respectively.

Thus, with Mo, which has an effusivity, e_{Mo}, higher than that of stainless steel, e_{SS}, inducing a possible melting of the substrate at impact. The melting is effectively observed in the crater formed below the particle impact. [100] As underlined by theory, [38] the formation of a crater modifies splat formation. However, with the increase in substrate temperature, the splat changes from highly splashed, flowerlike to relatively contiguous morphology. These underlines, again, the importance of the transition temperature. Similar results were obtained by Li et al. [101]

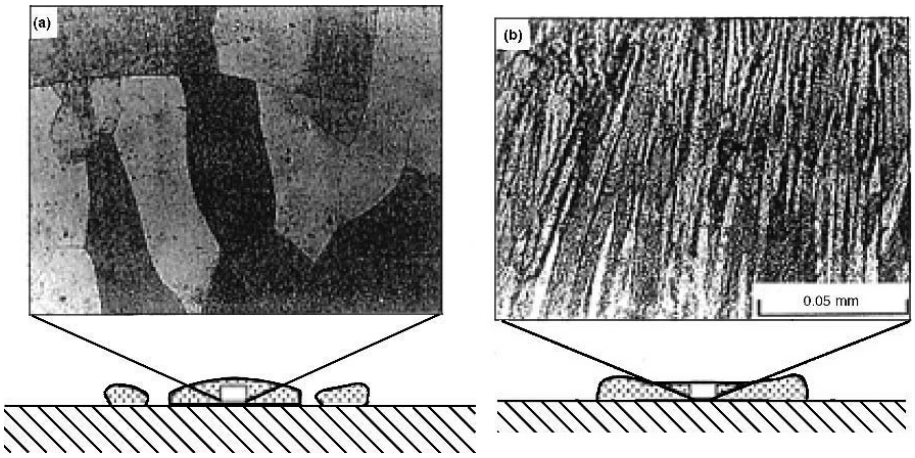

Figure 1.26: Cross section microstructures of nickel splats. On a stainless steel 304L substrate: (a) T_s = 300K, (b) T_s = 600 K [82]

Evaporable substances (xylene, glycol, and glycerol) with different boiling points (417, 471, and 563 K, respectively) were brushed on a polished stainless-steel substrate, $R_a <$ 0.05 μm, [102, 103] and the preheating of the substrate was used to control the presence of organic substances on the substrate surface. The plasma-sprayed materials were Al, Ni, Cu, Al_2O_3, and Mo. The results show that, except for Mo, the presence of an evaporable substance on the surface affects significantly the flattening process. As soon as the substrate is preheated 50 K over the boiling temperature of the organic film, which also corresponds for the studied systems to a substrate temperature over T_t, disk-shaped splats are obtained. Splats are extensively fingered below the evaporation temperature.

With Mo, the substrate preheating has little influence and disk-shaped splats are never obtained. [100] It is, thus, believed that the evaporation of the organic layer upon impact of the molten droplet induces the flattening splashing, probably by changing the flow directions in the periphery of the flattening droplet. [102, 103]

The transition temperature over which splats are disk shaped was also observed in low-pressure falling droplet experiments. [82, 83, 104] For example, Fukumoto et al. have shown that with Cu [82] or Ni, [84] 2 mm diameter droplets impacting on a 304L stainless steel substrate, the transition temperature depends also on a critical chamber pressure p_t. Below p_t, the transition does not depend anymore on substrate temperature as illustrated in Figure 1.27. At atmospheric pressure Figure 1.27(a), as already mentioned, over 500 K the transition to disk-shaped splats takes place and over 600 K, the column sizes are rather small. Once the substrate has been preheated either in air or soft vacuum, the column sizes are rather small (points c and d in Figure 1.27).

When the substrate is left at room temperature at a pressure of 10 Pa, the column size is small even at 300 K and decreases a little when the substrate temperature increases. Thus, it can be assumed that the desorption of adsorbates and condensates promotes the occurrence of disk- shaped splats. [80, 82, 102] This assumption was also made by Pershin et al. [105] when considering the impact of alumina particles plasma sprayed on stainless

steel and glass substrates where temperatures were varied in the range 20-500 °C.

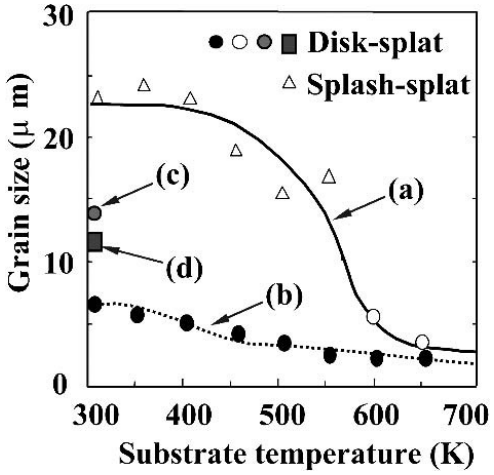

Figure 1.27: Grain size of a nickel splat at (a) atmospheric pressure, (b) low pressure 10 Pa, on an as-polished substrate (c), on substrate heated at 673 K in air and (d) in soft vacuum. [84]

The flattening splashing is not at all linked to the particle impact velocity because when varying it between 30 and 300 m/s for the same material and substrate, [45, 74] splats are disk shaped as soon as substrate temperature is over the transition temperature T_t. Thus, the flattening splashing occurring for $T_s < T_t$ when flattening is almost completed is linked to the flattening velocity v_f of the liquid flow. This velocity v_f depends on the initial particle impact velocity v_p but also on the liquid thickness controlling the splat CR (with impact velocity ratios up to 10 times, the splat thickness ratios are between 3 and 4 for the same droplet impact temperature T_p).

A new criterion K_f, based on the flattening information of the particle, has been introduced. It was obtained by using the maximum flattening velocity v_f and splat thickness b, and is defined as

$$K_f = We_f^{0.5} \cdot Re_f^{0.25} = \left(\frac{\rho \cdot b \cdot v_f^2}{\sigma}\right)^{0.5} \cdot \left(\frac{\rho \cdot b \cdot v_f}{\mu}\right)^{0.25} = \frac{\rho^{0.75} \cdot b^{0.75} \cdot v_f^{1.25}}{\sigma^{0.5} \cdot \mu^{0.25}}$$

The maximum flattening velocity v_f changes with substrate temperature. Its relationship with the impact velocity v_p can be expressed as

$$v_f = a \cdot v_p$$

The parameter a is a function of both substrate temperature and impact velocity: $a = f(T_s, v_p)$. Furthermore, it is assumed that the splat thickness b is constant during the flattening process and is equivalent to that obtained when the flattening is completed. The particle deforms from a spherical to a cylindrical shape just after the impact and the splat thickness b can be calculated from the conservation equation of mass

$$b = \frac{2 \cdot d_p^3}{3 \cdot D^2}$$

where D is the splat diameter.

It is then assumed the value of Madejski for the flattening ratio can be used, the expression of b is given by

$$b = 0.4 \cdot d_p \cdot Re^{-0.4}$$

and the new criterion K_f, based on the flattening parameter, is given as

$$K_f = 0.5 \cdot a^{1.25} \cdot Re^{-0.3} \cdot K$$

To evaluate K_f and the splat morphology, a concrete value of a is required. However, the flattening velocity of the thermal spray particle cannot be measured because the flattening is too fast (about 1 μs in DC spraying). Therefore, a value was measured by the free-falling droplet experiment under Reynolds and Peclet numbers equivalent to those experienced in thermal spraying. The experimental results are shown in Figure 1.28(a) for Ni droplets impacting on a stainless-steel substrate. It is found that a decreases monotonically with increasing T_s. Also, a remarkable change in a value occurs transitionally at the substrate temperature of T_t. This change corresponds to the change in the splat shape from splashed splat to disk-shaped splat. That is, once the disk-shaped splat is formed, the flattening velocity suddenly decreases. Thus, the flattening splashing is due to the rapid flow of the liquid during flattening. For thermal spray particles, it is expected that a similar change of a near T_t occurs. Figure 1.28(b) shows the calculated results of K_f. As T_s increases, K_f decreases gradually with a discontinuity for a substrate temperature of T_t. When $T_s = T_t$, the critical value of K_f is calculated as about 7. This corresponds to K_f^c that is the criterion for the flattening splashing. On the one hand, if K_f of the splat is smaller than K_f^c, which is 7, a disk-shaped splat is formed; on the other hand, if it is larger than 7, flattening splashing will occur.

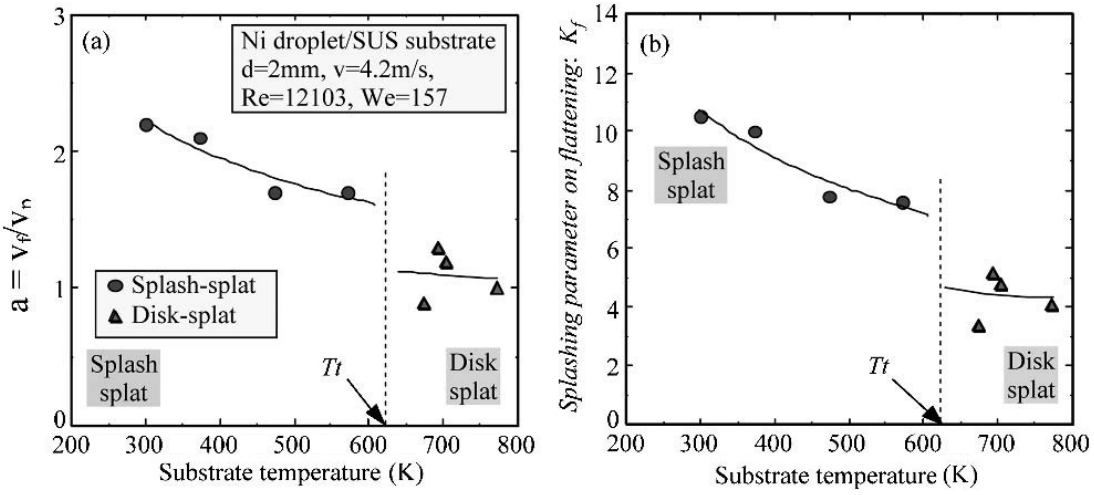

Figure 1.28: Change of flattening behaviour with substrate temperature: (a) measurement result of a, (b) evaluation result of K_f [83]

Most substrates are metals or alloys and the composition, roughness and thickness of the oxide layer at their surface play also a very relevant role on the splat formation and

its CR, controlling its final shape and thickness [106–114]. The oxide layer composition, roughness and thickness vary for the same metal or alloy with the preheating temperature, the preheating kinetic and the time during which the substrate is preheated.

The preheating temperature plays a very important role in the oxide layer development because it follows a kinetic law of Arrhenius type

$$e^{-\frac{E}{k \cdot T}}$$

However, for a given preheating temperature, the increase of the preheating time results in a thicker oxide layer but with no change in its composition [115]. When the oxide layer is thin (a few tens nanometres), as with titanium alloys or stainless steels, under certain conditions the oxide layer can be melted and an intermediate oxide formed enhancing the adhesion of the splat. This is the case with titanium substrates where the oxide layer is melted by the impact of liquid alumina particles forming $TiAl_2O_5$. It allows achieving a very good coating adhesion (greater than 50 MPa) on smooth substrate, R_a lower than 0.05 [114]. On the contrary, with stainless steel, the spinel layer at the surface even when melted cannot react with liquid alumina (no existing oxide) and the adhesion is fairly low.

When the oxide layer is thick, as with low carbon steel where the hematite layer can reach a few micrometres, no melting can occur and the adhesion is again purely mechanical.

As for plasma-sprayed alumina coatings deposited by the powder with a mean particle diameter of 20 μm, previous Li's study showed that the mean lamellar thickness under a typical deposition condition was 1.75 μm [51]. This result corresponds to a flattening degree of 2.76.

Wetting, described by the angle θ in Figure 1.29, affects the contact area between the splat and the underlying substrate. Thus, small contact angles reduce the contact area and increase thermal contact resistance, R_{th}.

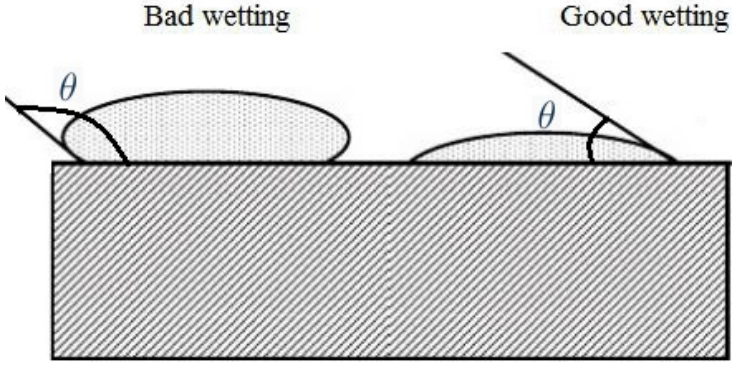

Figure 1.29: Wetting angles between a splat and the substrate [36]

Good wetting would result in a pancake shape rather than a flower shape, Figure 1.30. Additionally, a bad wetting could be one of the causes of gas cavities at the interface between the lamellae and the substrate.

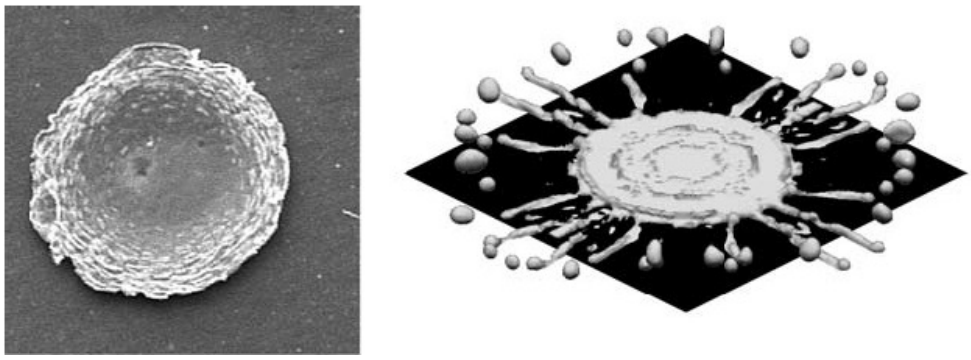

Figure 1.30: Splat shape: pancake (left), flower (right) [37]

Figure 1.31 shows the relationship between the degree of particle melting at impact and splat structure. When the particle is heat softened or beginning to resolidify, the splat does not flow out and begins to lift at the edges. Properly melted particle become into a splat that flows forming a well bonded classical lamellar shape. Superheated particle become into a splashed splat, creating debris, satellites, and dusting [35].

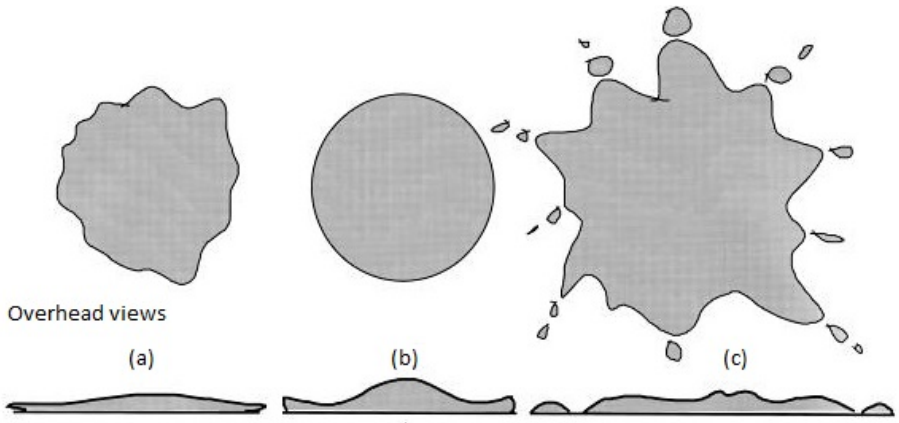

Figure 1.31: Relationship between degree of particle melting at impact and splat structure: a) Particle is heat softened or beginning to resolidify, b) Properly melted particle, c) Superheated particle [35]

Sand blasting determines the substrate roughness, whose irregularities constrain the splashing. The effect of the roughness substrate is rendered in Figure 1.32, which depicts a tin droplet of 2.2 mm diameter after impacting on a substrate. Time is represented on the left side and surface roughness, R_a, on the top.

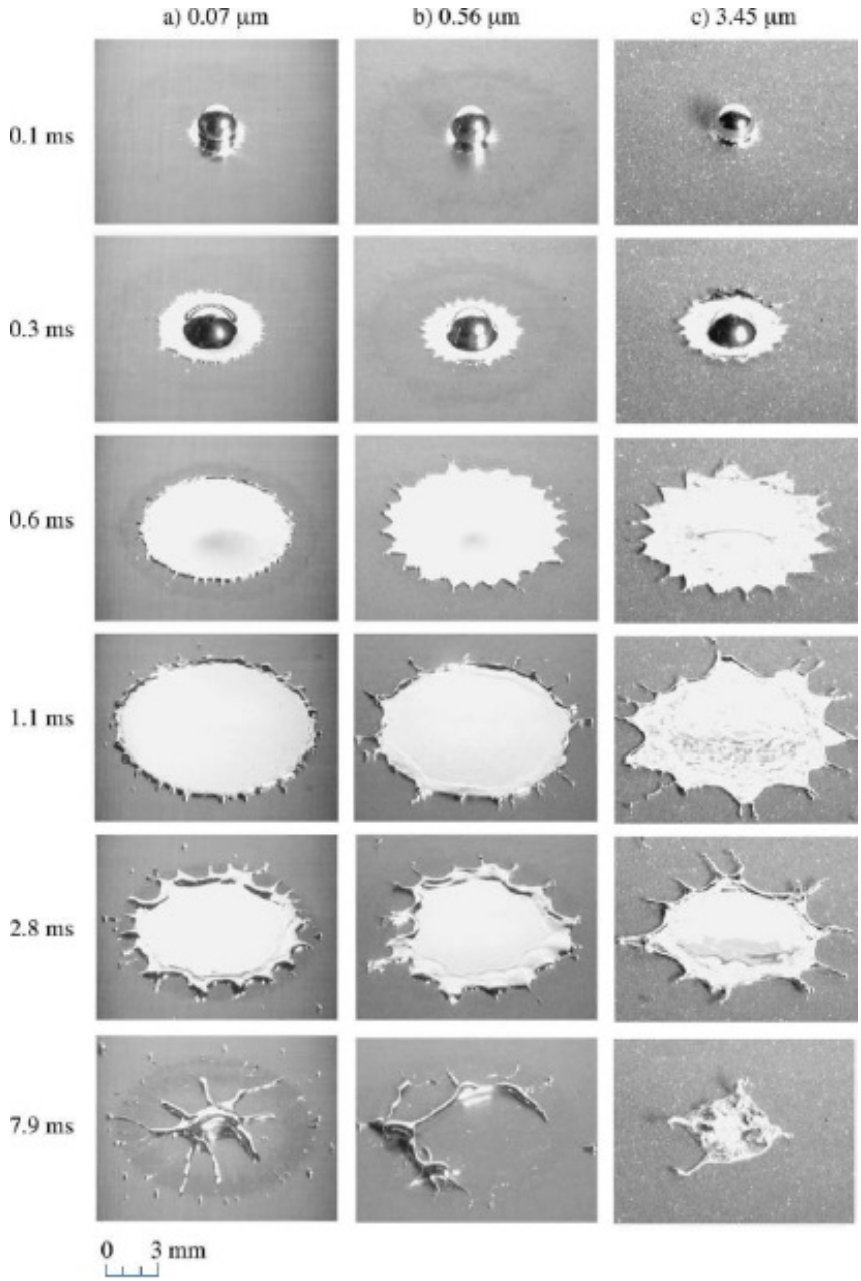

Figure 1.32: Impact of tiny droplets on a stainless-steel plate with different surface roughness [49]

It is remarkable the differences on droplet morphology. To be more precise, with lower surface roughness the droplet has more freedom in the shrinkage process, as it can be seen in the first column and bottom row. By contrast, as shows last column and bottom row, with bigger surface roughness, the droplet has more difficulties to move during the shrinkage process. Finally, the image in the second column and bottom row shows that the shrinkage process is more unstable and the droplet seems to split in two cores connected by a narrow strand.

The distance and angle between the tip of the gun and the substrate surface must be taken under consideration too for the understanding of splat shape. A long distance may result in freezing of the melted particles before they reach the target, whereas a short standoff distance may not provide sufficient time for the particles in flight to melt [36]. It is found that the porosity increases and the coating thickness decreases, hence deposition efficiency, with an increase in standoff distance [45].

The first factor to be considered in spraying under an angle α, 90° means spraying with the torch perpendicular to the substrate, is the reduction in the particles velocities. Just as the angle increases, the splats become more elongated, changing into elliptic rather than circular. The pressure with which the droplet acts on the substrate decreases with a factor of $\cos(\alpha)$. This may result in weaker mechanical and thermal interactions and, consequently, in worse adherence.

1.2.8 Splat adhesion

It is currently admitted [116, 117] that adhesion depends on several types of mechanisms, including chemical reaction, diffusion and mechanical interlocking.

Chemical reaction occurs only if the impacting particle melts locally the substrate and, when diffusion or mixing occurs between both liquids, a new compound can be formed.

For substrates at room temperature, chemical reaction can occur only if the particle effusivity is higher than that of the substrate, e_s.

For substrates preheated at higher temperatures (up to 700-1000K for stainless steel), it can occur with high temperature particles. It must be kept in mind that the highest the preheating temperature, the thickest the oxide layer. Its composition will also drastically change. TEM measurements showed that the interface splat–oxide layer was composed of elements coming both from the ceramic splat (Al_2O_3) and substrate (Ti-6Al-4V alloy) [118].

The adhesion of the alumina coating being 36±5 MPa for an initial $R_a \sim 10$ nm due to the oxide layer against 18±5 MPa for an initial $R_a \sim 50$ nm. On a polished 316L substrate with an oxide layer 20 nm thick, an alumina coating peeled off during spraying; when the substrate was covered with a 3 μm thick PECVD alumina coating ($R_a \sim 6$ nm), the adhesion reached 66±5 MPa.

The good adhesion on polished Ti-6Al-4V is probably due to the melting of the TiO_2 layer resulting in the formation of Al_2TiO_5, while no $Fe_xAl_yCr_zO_w$ oxide can be formed with the spinel at the surface of the 316L substrate.

Diffusion can be achieved for metals and alloys only if the substrate temperatures are over 1100–1200 K. It happens only if spraying is performed under soft vacuum and if the oxide layer at the substrate surface is previously withdrawn. It can be achieved for

example by using a reverse polarity transferred arc between the substrate and the anode of the plasma torch, with the plasma torch controlling the arc current of the transferred arc at low levels (a few tens of amperes).

Mechanical interlocking is the most encountered mechanism for coating adhesion. The heights of the peaks, R_t, must be adapted to the splat diameter ($2 \div 3$ R_t = D). However, the transition temperature plays here again a crucial role and the adhesion can be increased by a factor $2 \div 4$ when the substrate is preheated over the transition temperature.

Of course, as preheating promotes oxidation, it is of primary importance to know what happens with the development of the oxide layer. The characteristics of this oxide layer are linked to the substrate material, to the surrounding atmosphere for preheating and the way the substrate is preheated (flame, plasma jet or furnace, heating kinetic V_m, preheating temperature T_{ps} and preheating time t_{ps} [106-111, 119-124]). For example, considering 304L stainless steel substrates [119, 120, 123], two types of oxide layers are observed at 573 K: a $Fe_{3-x}Cr_xO_4$ spinel and a pure hematite, of $30 \div 50$ nm thickness depending on the preheating time. At 773 K, dual oxide layers with sesquioxide $Fe_{2-x}Cr_xO_3$ (x$\sim$0.1) and a Ni chromite spinel, of $50 \div 100$ nm thickness develop.

With low-carbon steel substrates, 1040 steel, and depending on the preheating parameters V_m, T_{ps} and t_{ps}, the relative thickness of both oxide layers formed (hematite at the top and magnetite at the bottom) can be varied [108]. The adhesion of alumina coating on a rough substrate reaches 34$\pm$4 MPa when the hematite content is high and 40$\pm$8 when it is low [108]. In fact, on smooth substrates, the hematite layer is very brittle and adhesion defects occur within it as soon as the thickness is higher than 150 nm, with splats detaching from the substrate and leaving a hole in such layers [108]. The importance of the preheating temperature and time is illustrated in Tables 1.4 and 1.5. It is observed that cast iron is very sensitive to the preheating time with a fast development in oxide layers; the adhesion/cohesion is almost divided by a factor of 3 as soon as the preheating time is multiplied by 3. The stainless-steel oxidation is not so drastic and when the preheating time is multiplied by 5, the adhesion/cohesion is only reduced by 30 %. In good connection with the preceding remarks about oxide layers, it might also be possible that roughness promotes the substrate or oxide layer melting, especially for the peaks under splats.

Table 1.4: Preheating temperature and time and substrate roughness for different tests [57, 125]

Test	Substrate material	Roughness R_a (μm)	Preheating time (s)	Preheating temperature (K)
1	Alumina on cast iron	6	90	500
2		6	300	500
3	Zirconia on SS 304L	12	60	573
4		12	120	773
5		12	600	773

Table 1.5: Effect of the preheating temperature and time on splat morphology an adhesion/cohesion of alumina or zirconia coatings deposited on different substrates [58, 125]

Test	Adhesion/cohesion (MPa)	Splat shape on smooth substrate	Column size (nm)
1	60 ± 5	Disk	100 - 150
2	22 ± 4	Fingered	Irregular
3	50 ± 2	Disk	125 - 250
4	65 ± 4	Disk	125 - 250
5	45 ± 2	Lace	125 - 250

Alumina particles were sprayed onto polished ($R_a \sim 0.4$ μm) plasma sprayed coatings [126]. The latter were either as-sprayed (with more than 99 wt % of γ phase) or preheated at 1373 K at a kinetic of 5 $K \cdot min^{-1}$, annealed for 6 h and cooled at a kinetic of 5 $K \cdot min^{-1}$ resulting in a 100 % α-columnar structure. Some were also preheated to 1873K at a kinetic of 5 $K \cdot min^{-1}$, annealed for 3 h and cooled at a kinetic of 5 $K \cdot min^{-1}$ resulting in a α-granular structure with grains between 3 and 5 μm. A PECVD coating ($\sim$ 3 μm thick) was also deposited on a stainless steel 304L substrate at 573 K. It presented a columnar structure with column diameters in the range of 100 $\div$ 150 nm and a R_a of 6 nm. The results obtained with splats and corresponding coatings are summarized in Table 1.6.

Table 1.6: Characteristics of splats and resulting coating adhesion when spraying alumina on different alumina substrates [126]

Alumina substrate manufacturing process	Substrate phase	R_a (nm)	Splat morphology	Adhesion (MPa)
Plasma spraying	γ-alumina	400	Columnar: regular 100 - 150 mm	35±3
PECVD	α-columnar	400	Columnar: irregular 150 - 300 nm	3±1
	α-granular	400	Columnar: very irregular 100 - 400 nm	Detached
	α-columnar	6	"Lace" or "ring" splat	60±5

Such results have been recently confirmed by Valette et al. [107, 109, 123]. When preheating a low-carbon steel substrate under a CO_2 atmosphere, a $Fe_{1-x}O$ develops at its surface. After plasma preheating of the substrate surface over the transition temperature, the $Fe_{1-x}O$ layer is transformed into Fe_3O_4. The resulting oxidized surface is composed of flat grains 1 $\div$ 2 μm thick and 3 $\div$ 7 μm wide. The alumina coating adhesion in this surface reaches 60 MPa and seems mainly due to a good progressive crystalline structures accommodation with five interfacial zones:

- a transition zone between the initial 1040 steel and C-impoverished steel resulting from the pre-oxidation treatment;
- a transition zone between steel, very poor in carbon and pure iron at the top of the C-diffusion area;
- an interface between pure iron and iron monoxide (wüstite), these two phases being linked by a well-known epitaxial relationship; it also possibly plays the role of a compliance zone because it is sometime considered as the most plastic iron oxide;
- a transition zone between $Fe_{1-x}O$ and Fe_3O_4 keeping memory of the initial iron monoxide structure (clusters observed in TEM pictures);
- an interface between Fe_3O_4 and γ-alumina with possible crystallographic relationship.

These interfaces correspond to a zone where the physical properties evolve gradually without any gap which is an essential condition for a good resistance to mechanical or thermal stresses [124].

The values of R_{th} in the range $10^{-7} - 10^{-8}$m^2 K/W, considered very low, can increase during the lamellae flattening. High values of R_{th} increase the solidification time and this may increase flattening of the lamellae. Quantification of the wetting effect is difficult because of the low precision of available data at high temperatures.

1.2.9 Residual stress

Other important splat characteristics are the development of cracks and pores on the splat surface [127]. At particle deposition on the substrate or rather coating surface, heat dissipates from the splats into the surface, which is accompanied by a shrinkage of the splats due to the change in temperature and phase transitions during solidification. Simultaneously, the substrate expands because of the rise in temperature [128]. These effects lead to tensile solidification and quenching stresses in the coating, Figure 1.33. Because of high solidification and quenching stresses, microcracks perpendicular to the surface can occur if the tensile stresses exceed the material ultimate tensile strength. The most likely cause of this intra-splat cracks is the residual stress relaxation [129].

Figures 1.34 and 1.35 show the effect of coating shrinkage. This phenomenon produces interfacial shear stresses that may deform the substrate or weaken the bond between the spray coating and the substrate, leading to the flaw of the coating.

The examination of fractured coating surface after fracture mechanics test and shear strength test suggest that cohesive fracture, explained later on Subsection 1.2.10, easily occurs on the interface area between flattened particles, the weakest part in the coating. It is also suggested that only limited interface area is in real contact [132].

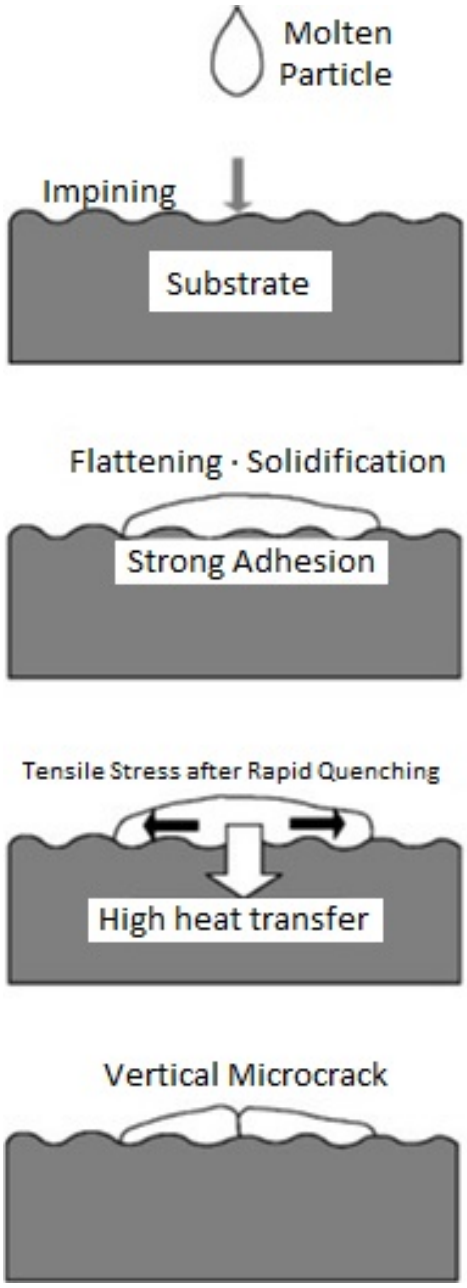

Figure 1.33: Schematic illustrations showing mechanism of vertical microcracking formation in a flattened particle [127]

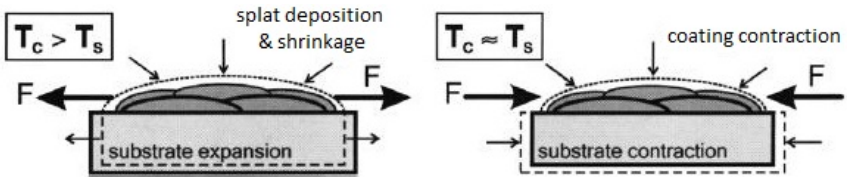

Figure 1.34: Formation of quenching stresses during solidification of the coating (left) and thermal stresses during temperature change of the component (right) [130]

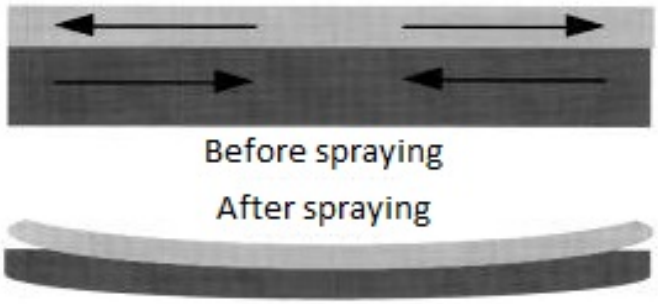

Figure 1.35: Effect of coating shrinkage [131]

Figure 1.36 shows a cross section of alumina coating with vertical microcracks. Measurement shows that the interface bonding of a commonly used alumina coating sprayed under optimised conditions only reaches to 32 %.

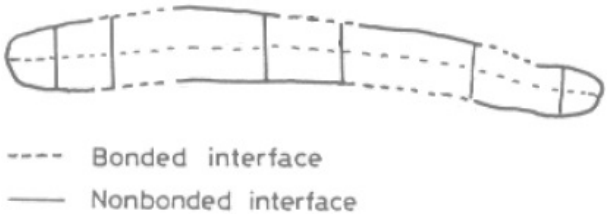

Figure 1.36: Schematic diagram of structure of a cross section of a flattened particle with vertical cracks: bounded interface (dashed line) and non-bounded interface (continuous line) [132]

The vertical fractures happen in the transition between bonded and non-bonded interfaces, except close to the end of the splat.

Figure 1.37 shows a schematic diagram of structure of a properly melted particle. In this figure, pores can be seen in the centre of the splat base. Another important characteristic is the fracture in the splat periphery.

Figure 1.37: Schematic diagram of structure of a properly melted particle [131]

The pores can be interlamellar and globular. The origin of the interlamellar pores come from incomplete splat contact, whereas the globular comes from unmelted particles, missing cores and trapped gas [24]. The interlamellar pores can be explained by poor heat transfer.

Figure 1.38 shows all micro-structural defects present in a thermally sprayed coating from a cross-section view. Number 1 indicates the substrate; number 2, weak contact to the substrate; number 3, crack resulting from one-torch-pass stresses; number 4, crack resulting from relaxation of vertical stresses; number 5, lamellae solidified with columnar

crystals; number 6, crack resulting from relaxation of in-plane stresses; number 7, large pore, a few micrometres in size; number 8, well-deformed lamellae; number 9, powder particle that remained solid upon spraying; number 10, small pore of sub-micrometre size.

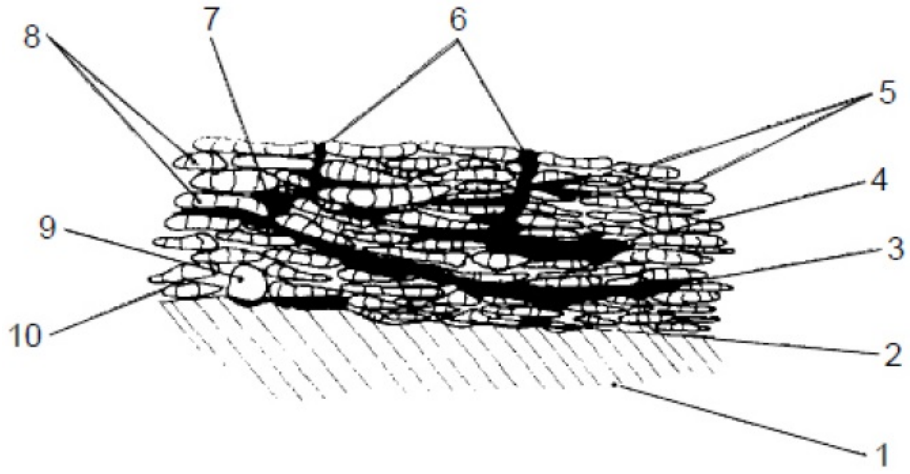

Figure 1.38: Cross-section of a thermally sprayed coating with all micro-structural defects [9]

1.2.10 Coating microstructure and mechanical properties

Molten particles impact on the substrate and their shapes change to lamellae. The transformation is controlled by the processes of deformation and solidification, being in turn dependent on the following factors:

- Particle velocity, size and temperature at impact.
- Particle material properties in the liquid state: wetting the substrate, viscosity and surface tension.
- Temperature and roughness of the substrate.
- Stand-off distance and angle.

The most common assumption about the solidification and deformation processes is to consider that these occur simultaneously. The temperature known as contact temperature at the interface between the particle and the substrate at impact influences adhesion of the lamellae and, consequently, adhesion of the coating to the substrate. The mechanism of adhesion can be, most probably, mechanical anchorage and, less probably, metallurgical bonding. The temperature in the particles bodies strongly influences the microstructure of coatings. At the beginning, its thermal evolution, cooling rate, determines its solidification, which, in turn, influences the formation of crystal phases and size.

To understand particle splashing, impact can be divided in two stages: a compressible one, starting when the spherical particle contacts the substrate and finishing with the formation of a truncated sphere, including compressed liquid near to the contact circle on the substrate surface; and an expansion one, starting at the end of the first stage. During this second stage, the liquid expands radially taking a shape like those shown in Figure 1.20.

In a quickly solidification, the α phase will remain and little γ phase will be formed; but the longer it takes, the more α alumina transforms into γ. Additionally, oxidation of lamellae can take place during the time of solidification, which is in the order of microseconds, before the next particle arrives. An oxide layer can be formed on the lamella's top.

1.2.11 Scanning Electron Microscope (SEM)

In optical microscopy, the probing beam is light that is either reflected on or transmitted through a specimen before forming its image. The image is formed by contrast between different features of the sample (brightness, phase, colour, polarization, fluorescence...) depending on the illuminating source. Magnification is controlled by a system of optical lenses. The limit of resolution is normally limited by the wavelength of the light used and not by the lens. According to diffraction theory, the closest distance between two points that can be resolved in an image is proportional to the wavelength λ [133].

In electron microscopy, the light is replaced by an electron beam. Since 10 to 500 keV electron beams have much lower wavelengths than light, the resolution is greater.

There are two main interactions between the energetic primary electron beam and specimen: elastic and inelastic. The deflection of incident electrons from the outer shell or nucleus of the specimen atoms are elastic interaction with a negligible kinetic energy loss. This type of interaction yields backscattered electrons. In case of inelastic scattering, the specimen atoms absorb a considerable amount of energy from the primary electrons and release their own electrons, secondary electrons, as a result. In addition to secondary electrons, inelastic interactions also cause the emission of Auger electrons, characteristic X-ray photons and cathodoluminescence. Modern SEM instruments use energy dispersive spectroscopy (EDS) to detect the emitted X-ray's for semi-quantitative analysis of the elemental composition. Figure 1.39 shows a schematic of the interaction volumes and resulted radiations.

The substantial energy loss during the inelastic interaction of the electron beam and material atoms leaves only a small amount of kinetic energy for secondary electrons, typically less than 50 eV. There are some backscattered electrons with this low level of energy, but their presence is negligible. Because of their low energy, secondary electrons can only escape from a depth of a few nanometres from the sample surface. Thus, secondary electrons are used to generate the topographical image at a resolution approximating the

size of the focused electron beam. Secondary electrons are the most commonly used in SEM due to their higher intensity compared to other types of radiations.

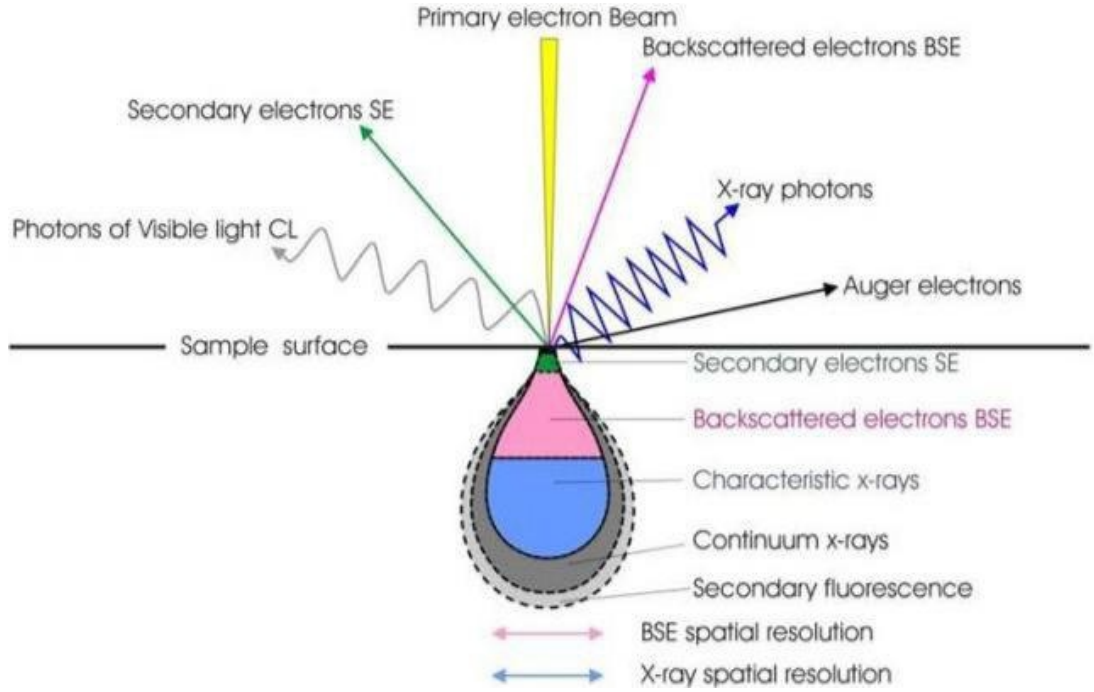

Figure 1.39: Signals generated from the interactions of the electron beam and sample in SEM and the regions from which the signals can be detected [134]

Backscattered electrons have kinetic energies greater than 50 eV. Due to their greater energy, backscattered electrons can escape from much deeper within the sample (more than 1 μm) in comparison to secondary electrons. Elements with higher atomic numbers can deflect more incident electrons, resulting in more backscattered electrons. Therefore, backscattered electron imaging is normally used to produce an image with good contrast between areas with different elements or chemical compositions.

It needs to be pointed out that inside most electron microscopes, spectroscopy is also performed as it is mentioned above. The electron beam used for imaging can excite X-ray fluorescence, especially in the heavy elements of the sample, and the energies of these photons can be analysed to identify these elements. For this type of analysis, the X-ray signal from the coating element needs to be kept in mind. Carbon is the most benign because it gives an almost undetectable signal. Metal coatings such as gold will give their characteristic signal and the investigator needs to check in advance whether this will interfere with any peaks from the specimen.

Energy-dispersive X-ray spectroscopy (EDX), sometimes called energy dispersive X-ray analysis (EDXA) or energy dispersive X-ray microanalysis (EDXMA), is an analytical technique used for the elemental analysis or chemical characterization of a sample. It relies on an interaction of some source of X-ray excitation and a sample. Its characterization capabilities are due in large part to the fundamental principle that each element has a unique atomic structure allowing a unique set of peaks on its electromagnetic emission

spectrum [135].

1.2.12 Sample preparation

Characterization of materials in the solid state can be a vast and diverse field encompassing many techniques [136-138]. In the last few decades, revolutionary changes in electronic instrumentation have increased the use of highly effective automated instruments for obtaining analytical information on the composition, chemistry, surface, and internal structures of solids at micrometre and nanometre scales. These techniques are based on various underlying principles and cannot be put under one discipline [133].

There are two common categories of materials characterization: microscopy and spectroscopy. Microscopy implies obtaining magnified images to study the morphology, structure, and shape of various features, including grains, phases, embedded phases, embedded particles, and so on.

The common microscopic techniques are:

- Optical microscopy (OM), with a maximum magnification of 1000: reflection, transmission, phase contrast and polarized light.
- SEM with resolution of 1000 Å.
- Transmission electron microscope (TEM), with spatial resolution ranges from 2 to 5 Å: scanning transmission electron microscope, high-resolution electron microscope and analytical electron microscope.

Table 1.7 provides a summary of the analytical techniques whose sample preparation concerns are covered.

Table 1.7: Common Microscopic Techniques and Sample Preparation Concerns [133]

TECHNIQUES	FEATURES
	SAMPLE PREPARATION
OM	Surface and internal microscopy, crystallographic information identification of particulates.
	Polish and etch one side for reflection mode. Some thinning for transmission mode.
SEM	Surface and internal morphology. Special techniques to characterize semiconductor and magnetic devices.
	Polish and etch (apply coating if required) one side.
TEM	Internal nanostructure. Some case of surface structure if using replicas. Phase determination capability. Crystallographic information from 4000 $Å^2$ area.
	Very critical. Ultrathin specimens needed.

The oldest microscopy technique for materials analysis was optical microscopy. Even

to this day, for feature sizes above 1 μm, this is one of the most popular tools. For smaller features, electron microscopy techniques such as SEM and TEM are the tools of choice.

For both optical and electron microscopy, specimen preparation is crucial, the basic concern being that the specimen prepared be a true representative of the sample. The first step obviously is to cut the specimen to obtain a suitable size. After that, the cut sample surface is polished to expose the feature(s) of interest. These steps are commonly referred to as metallography even though they are applicable to not only to metal. For reflection modes of microscopy, OM and SEM, polishing could be followed by etching. The cut sample size depends on the microscope and could range from a few centimetres in a normal SEM to a few inches in a specially designed SEM. Thus, the main step for sample preparation is depicted at the following diagram, Figure 1.40.

The electron beam belonging to the SEM techniques requires completely different instrumentation (source, collimator, detector, magnification control...) from the optical ones. Moreover, electrons are very readily absorbed by matter. Therefore, the entire path of the beam, from source to specimen to detector, must be in vacuum. From the sample preparation point of view, this is of major significance.

For this type of microscopy, in the case of electrically insulating materials, the surface of the specimen may be electrically isolated when bombarded with electrons. This leads to charge build-up on the specimens that makes imaging or other analysis difficult. To address this issue, special sample coating steps are often required.

In the SEM, electrically non-conducting specimens can absorb electrons and accumulate a net negative charge that repels the following electron beam, thereby degrading the image [139]. To a certain extent, lowering the accelerating voltage or reducing the spot size can reduce this artefact, but that would limit the instrument capability considerably. The best way to counter this is to coat the specimen with a thin conducting film. In the past, organic antistatic agents have been tried, but the best method is to deposit a thin film (tens of nanometres) of a metal or carbon [140]. This step, although not mandatory, is also used in some TEM studies to enhance electronic contrast.

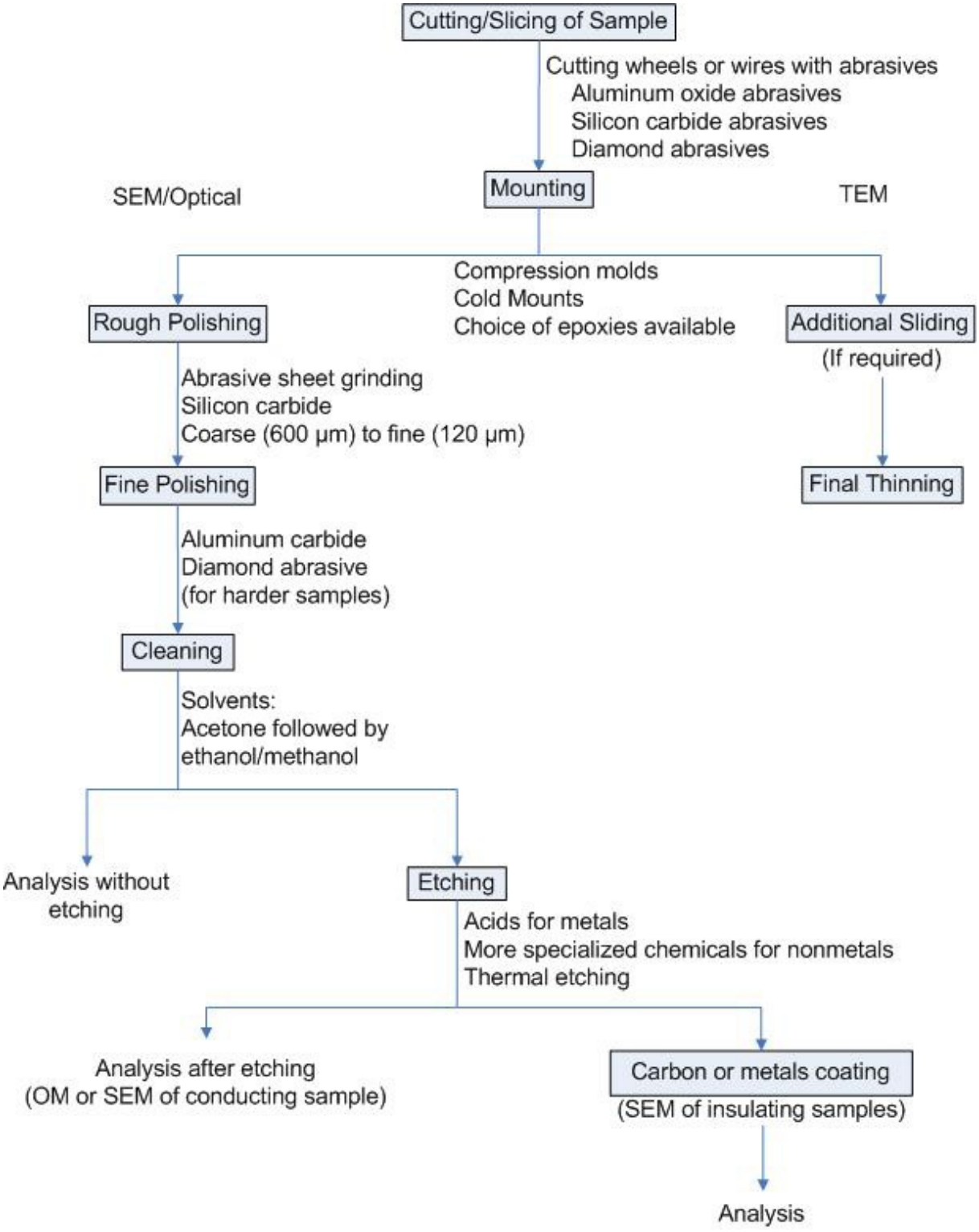

Figure 1.40: Basic steps for specimen preparation-microscopy [133]

1.2.13 Image processing analysis

The interest of the application of image processing (IP) in surface science seems obvious. Dependent on the scale, direct or indirect visual evaluation of the surface structure is always sought. In micro- and nanoscience and technology this is also true. Numerous characterization tools and methods produce as output two dimensional structures that can be considered as images and treated as such.

In fact, image processing can be applied at smaller or larger extent to virtually all the range of available non-destructive evaluation techniques including [141]:

1. Optical interferometer and profilometers or microtopographers.
2. Diffractometers as angle-resolved scattering and total integrated scattering.
3. Ellipsometers.
4. Spectroscopes and fluorescence spectrophotometers.
5. Photoacoustic and life-time spectroscopy systems.
6. Scanning electron microscope.
7. Scanning tunnelling microscope.
8. Atomic force microscope.
9. Raman spectroscopy.
10. X-ray diffraction (XRD).
11. Fourier transform infrared spectroscopy.
12. Eddy currents.
13. Induced magnetic fields.
14. Thermal waves analysis.
15. Ultrasonic waves.
16. X-ray.
17. Shearographers.
18. Holographic and tomographic systems.

An image is considered to be a two-dimensional function, f(x,y), where x and y are spatial coordinates, and the amplitude of at any pair of coordinates (x,y) is called the intensity or grey level of the image at that point. When x,y, and the amplitude values of f are all finite, discrete quantities, the image is called a digital image [142]. In general, an

image may be considered as being formed by or to containing sub-images [141].

The histogram of an image is the graphical representation of the number of pixels for each intensity value. In Figure 1.41, the histogram of the image named pout is shown.

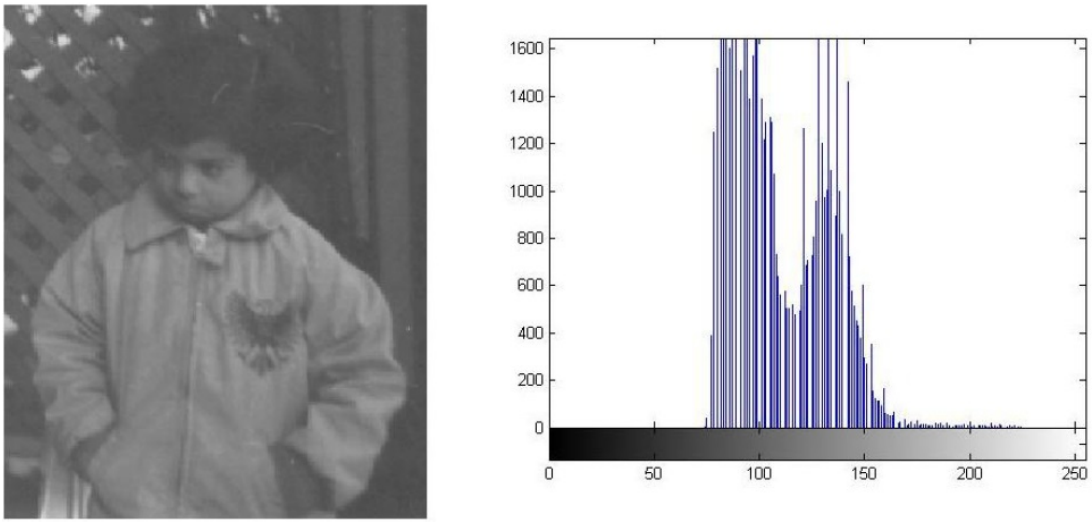

Figure 1.41: Plot of the histogram for the intensity image pout [143]

Contrast is defined as the separation between the darkest and brightest parts of the image. The above image shows that this has a low contrast as it only covers almost a third of the total tone range. For this reason, this image is low quality.

Noise is defined as an undesirable variation of the pixel intensity values. This variation can be random, as in the pepper and salt noise; or not, as in periodic noise.

Therefore, appropriate techniques of refining images are needed so that the resultant images are of better visual quality, free from aberrations and noises. Image enhancement, filtering, and restoration have been some of the important applications of image processing since the early days of the field.

Bellow, a list of the most important operators or processing techniques in surface characterisation is provided [142, 144]:

1. Color corrections such as brightness and contrast adjustments, color mapping, color balancing, quantization, or color translation.
2. Contrast stretching and histogram equalisation and manipulation.
3. Binary operations.
4. Arithmetic-based operations.
5. Convolution-based operations in the spatial domain or in the frequency domain.
6. Smoothing Operations.

7. Linear and non-linear Filters.
8. Derivative-based Operators.
9. Morphological Operators, Dilation and Erosion, Boolean Convolution, Opening and Closing, Skeletonization, Propagation.
10. Morphological smoothing enhancing and edge detection.
11. Shadowing Correction.
12. Defocus correction.
13. Enhancement and Restoration Techniques.
14. Unsharp masking, Noise suppression, Distortion suppression, Segmentation.
15. Thresholding and binarization.
16. Colour manipulation.
17. Pseudo colouring.
18. Processing in the Fourier space. Spatial filtering. Correlation and convolution.
19. Measuring and characterization.
20. Euclidean geometry transformations such as enlargement, reduction, and rotation.
21. Digital compositing or optical compositing (combination of two or more images). Used in film-making to make a "matte".
22. Interpolation, demosaicing, and recovery of a full image from a raw image format using a Bayer filter pattern.
23. Image registration, the alignment of two or more images.
24. Image recognition, for example, extract the text from the image using optical character recognition or checkbox and bubble values using optical mark recognition.
25. Image segmentation.
26. High dynamic range imaging by combining multiple images.
27. Geometric hashing for 2-D object recognition with affine invariance.

1.3 Preliminary work

This work is related with the research line of the research group, called Numerical Simulation in Industrial Engineering, belonging to Polytechnic University of Cartagena. To be more precise, this research line deals with analysis of coating on machine pieces. In addition, the final degree project developed by Diego Ángel López Gallego and the thesis not yet finished of Noelia González Morales are used as a data base to carry on with the task.

As mentioned in Section 1.2, the coatings are an important technological development that improves the protection against heat, wear or corrosion that are found in each production step in industry. One of the approaches, which contribute to a better insight of the relationship between the coating properties and the spray parameters, is the knowledge of the manner in what the droplets are deposited onto the substrate surface. The aforementioned work developed the methodology which let us analyse the splash shape.

In this way, the components of the research group have established, since several years, a collaboration with the Institute for Manufacturing Technologies of Ceramic Components and Composites (IFKB), belonging to the Stuttgart University. Carrying on with this collaboration, single splats and coatings images from SEM have been analysed.

1.4 Only the important literature

Ya-Zhe Xing; Xing-Hang Li; QiangWang; Yong Zhang; & Xu-Ding Song. Substrate temperature dependence of splat morphology for plasma-sprayed cast iron on aluminum surface. 2015, Surface & Coatings Technology, Vol 283, 234-240.

Sobolev, V.V; & Guilemany J.M. Flattening of droplets and formation of splats in thermal spraying: a review of recent work–Part 2. 1999, J. Therm. Spray Technol., Vol. 8, 301–314.

Pasandideh-Fard, M; Pershin, V; Chandra, S; & Mostaghimi, J. Splat shapes in a thermal spray coating process: simulations & experiments. 2001, Journal of Thermal Spray Technology, 11, pp. 206-217.

Ohmori, A; & Li, C-J. The structure of thermally sprayed ceramic coatings and its dominant effect on the coating properties. 1993, Plasma Spraying, theory & applications (ed.) Surayanarayanam, World Scientific Publishing CO., pp. 179-200.

Berndt, C.C.J. Measurement of adhesion for thermally sprayed materials. 1993, Adhesion Sci. Technol. 7(12), pp. 1235-1264.

Kilkarni, A; Goland, A; Herman, H; Allen, A.J; Ilabsky, J; Long, G; & De Carlo, F. Knowledge Concerning Splat Formation: An Invited Review. 2004, Journal of Thermal

Spray Technology 356, 13(3), pp. 239-250.

Pech, J., Hannoyer, B., Lagnoux, O., Denoirjean, A., and Fauchais, P. (1999). In "Progress in Plasma Processing of Materials" (P. Fauchais and J. Amouroux, eds.), p. 543. Begell House, New York.

Chapter 2

Nature of the work

2.1 Introduction

This section deals with the aims of the study, the useful effects of this work and ultimately the work in the future in relation to this process of manufacture.

2.2 Aims of the task

The basic aim of the present work is the application of SEM in order to characterise the splat morphology in APS coatings. As result of this test, the relationship between the APS parameters and the resulting splats is established, which allows the optimization of the process.

2.3 Useful effects

On the one hand, this work permits to classify the splat morphology according to the spray parameters. On the other hand, it permits a better understanding of the splashing process.

Additionally, the information from this image analysis would allow checking the quality of the coating.

2.4 Future studies

As interesting works in the future, it is recommended:

- Phases analysis by XRD.
- Splat cutting by Focused Ion Beam (FIB).
- Chemical treatment of the splats in order to show the internal structure.

Chapter 3

Analysis of the literature

1. Okumus, S.C. Microstructural & mechanical characterisation of plasma sprayed $Al_2O_3 - TiO_2$ composite ceramic coating on Mo/cast iron substrates. 2005, Materials Letters, 59, pp. 3214-3220.

   This reference provides general information, which contains from the atmospheric plasma spray process to the splat characterisation.

2. Dhiman, R., McDonald, A.G. & Chandra, S. Predicting splat morphology in a thermal spray process. 2007, Surface & Coatings Technology, 201, pp. 7789-7801.

   This reference provides general information, which contains from the atmospheric plasma spray process to the splat characterization.

3. Zhang, H., Wang, X.Y., Zheng, L.L. & Jiang, X.Y. Studies of splat morphology & rapid solidification during thermal spraying. 2001, Int. J. of Heat & Mass Transfer, 44(24), pp. 4579-4592.

   This reference provides general information, which contains from the atmospheric plasma spray process to the splat characterization.

4. Acedo Fornell, M. C. Thermally sprayed coatings on piston rings, processing and characterization. Augsburg, 2005.

   This reference provides general information, which contains from the atmospheric plasma spray process to the splat characterization.

5. Oksa, M., Turunen, E., Suhonen, T., Varis, T. & Hannula S. "Optimization and Characterization of High Velocity Oxy-fuel Sprayed Coatings: Techniques, Materials & Applications". Coatings 2011, 1, pp. 17-52.

   This paper deals with issues related to comparison between APS and other thermal spray processes.

6. Gadow, R., Friedrich, C., Killinger, A. & Floristán, M. Development of Atmospheric Plasma Sprayed Dielectric Ceramic Coatings for High Efficiency Tubular Ozone Generators.2010, Journal of Water Resource and Protection, Vol. 2, No. 9, Article ID: 2716, 10 pages.

   This article provides information about atmospheric plasma spray processes.

7. Metalizing Equipment CO. PVT. LTD, Provider of thermal spray technology & surface engineering solutions `http://www.mecpl.com/wire-arc-spray.php`

   This website provides useful information for handle the wire arc spray equipment.

8. Pawlowski, L. The Science & Engineering of Thermal Spray Coatings. 2008, second edition, John Wiley & Sons, Ltd, pp. 67-113.

   This classical book provides general information, which contains from the atmospheric plasma spray process to the splat characterisation.

9. I. Levin and D. Brandon, J. Am. Ceram. Soc. 81[8] (1998) 1995-2012.

   This paper deals with alumina phase.

10. The effect of cooling rate in thermally sprayed alumina. A. Zimmer.

    This paper deals with sprayed alumina.

11. C. Landron, L. Hennet, T.E. Jenkins, G.N. Greaves, J. P. Coutures and A.K. Soper, Phys. Rev. Lett. 86[21] (2001) 4839-4842.

    This paper deals with alumina phase.

12. B. Glorieux, F. Millot, J.-C. Rifflet and J.-P. Coutures, Int. J. Thermophys. 20[4] (1999) 1085-1094.

    This paper deals with alumina grain morphology.

13. C.G. Levi, V. Jayaram, J.J. Valencia and R. Mehrabian, J. Mater. Res. 3[5] (1988) 969-983.

    This paper deals with the thermal history of alumina powders.

14. D.E. Ashenford, F. Long, W.E. Hagston, B. Lunn and A. Matthews, Surf. Coat. Tech. 116–119 (1999) 699-704.

    This paper deals with alumina phase.

15. M.L. Gualtieri, M. Prudenziatia and A.F. Gualtieri, Surf. Coat. Tech. 201[6] (2006) 2984-2989.

    This paper deals with alumina phase.

16. L. Li, B. Kharas, H. Zhang and S. Sampath, Mat. Sci. Eng. A-Struct. 456[1-2] (2007) 35-42.

This paper deals with HOVF process.

17. T. Chraska and A.H. King, J. Mater. Sci. Lett. 18[18] (1999) 1517-1519.

This paper deals with alumina grain morphology.

18. J. Zhang, H. Chen, T. Sekino, S.H. Kim and S.W. Lee, J. Ceram. Proc. Res. 9[3] (2008) 317-320.

This paper deals with thermal alumina spraying.

19. Aleinov, I. and Puckett, E. G. (1995). "Proceedings of the 6th International Symposium on Computational Fluid Dynamics", Lake Tahoe, CA, p. 13.

This paper deals with thermal alumina spraying.

20. D.I. Pantelis, Traité Métall. M1 240 (1993) 22 (in French language).

This paper deals with alumina grain morphology.

21. S. Kou, Welding Metallurgy, John Wiley & Sons, New York, 1987.

This paper deals with alumina grain morphology.

22. D.K. Chistoulis, D.I. Pantalis, F. Borit, V. Guipont, M. Jeandin, Proceedings of 5th I International Conference "THE Coatings in Manufacturing Engineering", Chalkidiki, Greece, October 2005, pp. 229-239.

This paper deals with alumina grain morphology.

23. S. Beauvais, V. Guipont, F. N'Guyen, M. Jeandin, D. Jeulin, A. Robisson, R. Saenger, Thermal Spray Solutions. Advances in Technology and Applications, Proceedings of the 2004 International Thermal Spray Conference, ASM International Osaka, Japan, 2004, 2004 (only in CD-ROM).

This CD-ROM deals with alumina grain morphology.

24. M. Ducos, B. Bossuat, H. Walaszek, S. Barradas, M. Jeandin, Building on 100 years of success, Procedings of the 2006 International Thermal Spray Conference, ASM International (only in CD-ROOM), seatle, USA, May 2006.

This CD-ROM deals with alumina grain morphology.

25. C. Moreau, P. Gougeon, M. Lamontagne, J. Therm. Spray. Technol. 4 (1) (1995) 25-33.

This paper deals with alumina grain morphology.

26. D.K. Christoulis, D.I. Pantelis, F. Borit, V. Guipont, M. Jeandin, Surf. Eng. 6 (2006) 420-431.

This paper deals with alumina grain morphology.

27. T. Chraska, A.H. King, Thin Solid Films 397 (2001) 30–39.

This paper deals with thermal alumina spraying and alumina grain morphology.

28. W. Kurz, D.J. Fisher, Fundamentals of Solidification, 3rd ed., Trans Tech Publications, 1989.

This paper deals with thermal alumina spraying and alumina grain morphology.

29. ASM Handbook, Welding, Brazing and Soldering, vol. 6, ASM International, 1993.

This paper deals with thermal alumina spraying and alumina grain morphology.

30. M. Fukumoto, T. Yamaguchi, M. Yamada, and T. Yasui. Splash Splat to Disk Splat Transition Behavior in Plasma-Sprayed Metallic Materials, J. Therm. Spray Technol., 2007, 16(5-6), p 905-912.

This paper deals with splat morphology.

31. L. Bianchi, A. C. Leger, M. Vardelle, A. Vardelle, and P. Fauchais. "Splat Formation and Cooling of Plasma-Sprayed Zirconia", Thin Solid Films, 1997, 305, pp. 35-47.

This paper deals with splat morphology.

32. L. Bianchi, A. Denoirjean, F. Blein, and P. Fauchais: "Microstructural Investigation of Plasma Sprayed Ceramic Splats", Thin Solid Films, 1977, 299, pp. 125-35.

This paper deals with splat morphology.

33. Kudinov V. V., Pekshev P. Y. & Safiullin V. A. Forming of the Structure o Plasma Sprayed Materials. 1989, High Temp. Dust Laden Jets, (ed.) sololenko et Fedorchenko, pp. 381-418.

This paper deals with morphology of plasma sprayed alumina particles based on their velocity and temperature prior to impact.

34. A. Vardelle, C. Moreau, and P. Fauchais: "Deposit Formation Dynamics", MRS Bull., 2000, July, pp. 32-37.

This paper deals with splat flattening.

35. R.C. Dykhuizen: "Review of Impact and Solidification of Molten Thermal Spray Droplets", J. Therm. Spray Technol., 1994, 3(4), pp. 351-61.

This paper deals with splat flattening and adhesion.

36. P. Fauchais, A.C. Leger, M. Vardelle, and A. Vardelle: "Formation of Plasma-Sprayed Oxide Coatings", in Proc. of the Julian Szekely Memorial Symp. on Materials Processing, H.Y. Sohn, J.W. Evans, and D. Apelian, ed., TMS, Warrendale, PA, 1997, pp. 571-92.

This paper deals with splat flattening.

37. V.V. Sobolev and J.M. Guilemany: "Flattening of Droplets and Formation of Splats in Thermal Spraying: A Review Of Recent Work-Part 1", J. Therm. Spray Technol., 1999, 8(1), pp. 87-101; "Flattening of Droplets and Formation of Splats in Thermal Spraying: A Review Of Recent Work-Part 1", J. Therm. Spray Technol., 1999, 8(2), pp. 301-14.

This paper deals with splat flattening and adhesion.

38. S.Q. Armster, J.-P. Delplanque, M. Rein, and E.J. Lavernia: "Thermo-Fluid Mechanisms Controlling Droplet Based Materials Processes", Int. Mater. Rev., 2002, 7(6), pp. 265-301.

This paper deals with splat flattening and adhesion.

39. C. W. Kang and H.W. Ng, Splat Morphology and Spreading Behavior Due to Oblique Impact of Droplets onto Substrates in Plasma Spray Coating Process, Surf. Coat. Technol., 2006, 200, p 5462-5477.

This paper deals with splat flattening.

40. J. Madejski: "Solidification of Droplet on a Cold Surface", Int. J. Heat Mass Transfer, 1976, 19, pp. 1009-20.

This paper deals with splat flattening.

41. A. Vardelle, M. Vardelle, P. Fauchais, and D. Gobin, Monitoring Particle Impact on a Substrate During Plasma Spray Process, NATO Ser. E Appl. Sci., 1995, 282, p 95-121.

This paper deals with splat flattening.

42. S. Amada, K. Tomoyasu, and M. Haruyama, Splat Formation of Molten Sn, Cu and Ni Droplets, Surf. Coat. Technol., 1997, 96, p 176-183.

This paper deals with splat flattening.

43. S. Amada, M. Haruyama, and T. Ohyagi, Kazuyuki Tomoyasu, Wettability Effect on the Flattening Ratio of Molten Metal Droplets, Surf. Coat. Technol., 2001, 138, p 211-219.

This paper deals with splat flattening.

44. C.-J. Li, H.-L. Liao, P. Gougeon, G. Montavon, and C. Coddet, Experimental De-

termination of the Relationship Between Flattening Degree and Reynolds Number for Spray Molten Droplets, Surf. Coat. Technol., 2005, 191, p 375-383.

This paper deals with splat flattening.

45. M. Pasandideh-Fard, R. Bhola, S. Chandra, and J. Mostaghimi, Deposition of Tin Droplets on a Steel Plate: Simulations and Experiments, Int. J. Heat Mass Trans., 1998, 41, p 2929-2945.

This paper deals with splat flattening and adhesion.

46. Li, C.-J., Liao, H.-L. Gougeon, P., Montavon, G. & Coddet, C. Experimental determination of the relationship between flattening degree and Reynolds number for spray molten droplets. 2005, Surface & Coatings Technology, 191, pp. 375–383.

This work deals with the relationship between the in-flight particle and substrate conditions, and the formation of the different known splat shapes.

47. Li, C.-J. Characterisation of the microstructure and properties of plasma-sprayed ceramic coatings. 1989, PhD thesis, Osaka University.

This paper deals with issues related to the plasma spray process parameters and its contention with splat microstructure.

48. C. Mundo, M. Sommerfeld, and C. Tropea: "Droplet-Wall Collisions: Experimental Studies of the Deformation and Break-Up Process", Int. J. Multiphase Flow, 1995, 21, pp. 151-73.

This paper deals with splat flattening.

49. C.D. Stow and M.G. Hadfield: "An Experimental Investigation of Fluid Flow Resulting From the Impact of a Water Drop With an Underlying Dry Surface", Proc. R. Soc. London, 1981, A373, pp. 419-41.

This paper deals with splat flattening and adhesion.

50. C. Escure, M. Vardelle, and P. Fauchais: "Experimental and Theoretical Study of the Impact of Alumina Droplet on Cold and Hot Substrates", Plasma Chem. Plasma Process., 2003, 3, pp. 291-309.

This paper deals with splat flattening.

51. R.F. Allen: "The Role of Surface Tension in Splashing", J. Coll. Interface, 1975, 51, pp. 350-51.

This paper deals with splat flattening.

52. Cedelle, J., Vardelle, M., Pateyron, B., and Fauchais, P. (2004). Experimental investigation of the splashing processes at impact in plasma sprayed coating formation. In "Proceedings of the International Thermal Spray Conference", pp. 1008-1013,

Osaka, Japan and DVS Düsseldorf, Germany (electronic version).

This paper deals with splat flattening.

53. Allen, R. F. (1975). J. Colloid Interf. 51, 350.

This paper deals with splat flattening.

54. Vardelle, A., Vardelle, M., Fauchais, P., and Gobin, D. (1995). NATO Ser. E Appl. Sci. 282, 95.

This paper deals with splat flattening.

55. Wang, S. P., Wang, G. X., and Matthys, E. F. (1998). Int. J. Heat Mass Transfer 41, 1177.

This paper deals with splat flattening.

56. Sun, D. W., Xu, J., Zang, H., Wan, Y. P., Prasad, V., and Wang, G. X. (2000). Effect of contact resistance and substrate melting on thermal spray coating. In "Thermal Spray: Surface Engineering via Applied Research" (C.C. Berndt, ed.), pp. 195–201. ASM International, Materials Park, OH, USA.

This paper deals with splat flattening.

57. Fauchais, P., Vardelle, M., Vardelle, A., Bianchi, L., and Leger, A. C. (1996). Plasma Chem. Plasma Process. 16(1), 99S.

This paper deals with splat flattening and adhesion.

58. Sobolev, V. V. and Guilemany, J. M. (1999). Part 1, J. Therm. Spray Techn. 8(1), 87.

This paper deals with splat flattening.

59. Sobolev, V. V. and Guilemany, J. M. (1999). Part 2, J. Therm. Spray Techn. 8(2), 301.

This paper deals with splat flattening.

60. Vardelle, A., Moreau, C., and Fauchais, P. (2000). MRS Bull. July, pp. 32–37.

This paper deals with splat flattening.

61. Dykhuizen, R. C. (1994). J. Therm. Spray Techn. 3(4), 351–361.

This paper deals with splat flattening.

62. Fauchais, P., Leger, A. C., Vardelle, M., and Vardelle, A. (1997). Formation of plasmasprayed oxide coatings. In "Proceedings of the Julian Szekely Memorial Symposium on Materials Processing" (H.Y. Sohn, J.W. Evans and D. Apelian, eds.), p.

571. TMS, Warrendale, P. A.

This paper deals with splat flattening.

63. Pasandideh-Fard, M., Bhola, R., Chandra, S., and Mostaghimi, J. (1998). Int. J. Heat Mass Transfer 41, 2929–2945.

This paper deals with splat flattening.

64. Robert, C., Denoirjean, A., Vardelle, A., Wang, G. X., and Sampath, S. (1998). Nucleation and phase selection in plasma-sprayed alumina: modelling and experiment. In "Thermal Spray: Meeting the Challenges of the 21st Century" (C. Coddet, ed.), pp. 767–773. ASM International, Materials Park, OH, USA.

This paper deals with splat flattening.

65. Pasandideh-Fard, M., Pershin, V., Chandra, S., and Mostaghimi, J. (2002). J. Therm. Spray Techn. 11(2), 206–217.

This paper deals with splat flattening.

66. Sobolev, V. V., Guilemany, J.M., and Martin, A. J. (1996). J. Therm. Spray Techn. 5(2), 207.

This paper deals with splat flattening.

67. Fukanuma, H. (1996). Mathematical modelling of flattening process on rough surfaces in thermal spray. In "Thermal Spray: Practical Solutions for Engineering Problems" (C. C. Berndt, ed.), pp. 647–656. ASM International, Materials Park, OH, USA.

This paper deals with splat flattening.

68. Fukanuma, H., Xie, R., Oo, N., Fujiwara, J. Y., and Kuroda, S. (2002). Characterization of roughened substrate surface on bond strength of thermal spray deposits. In "International Thermal Spray Conference Proceedings" (E. Lugscheider, ed.), pp. 312–317. DVS, Düsseldorf, Germany.

This paper deals with splat flattening.

69. C. Escure, M. Vardelle, and P. Fauchais: "Visualization of Particle Impact in Thermal Spray", in Thermal Spray: Surface Engineering Via Applied Research, C.C. Berndt, ed., ASM International, Materials Park, OH, 2000, pp. 743-52.

This paper deals with splat flattening.

70. C. Escure, M. Vardelle, A. Vardelle, and P. Fauchais: "Visualization of the Impact of Drops on a Substrate in Plasma Spraying Deposition and Splashing Modes", in Thermal Spray 2001, New Surface for a New Millenium, C.C. Berndt, K.A. Khor, and E.F. Lugscheider, ed., ASM International, Materials Park, OH, 2001, pp. 805-

12.

This paper deals with splat flattening.

71. M. Fukumoto, S. Katoh, and I. Okane: "Splat Behavior of Plasma Sprayed Particles on Flat Substrate Surface", in Proc. of the 14th Int. Thermal Spray Conference, Vol. 1, A. Ohmori, ed., High Temp. Soc. of Japan, Osaka, Japan, 1995, pp. 353-59.

This paper deals with splat flattening.

72. J.M. Houben: "Future Development in Thermal Spraying", in Proc. 2nd National Conference on Thermal Spray, 1984, pp. 1-19.

This paper deals with splat flattening.

73. M. Fukumoto, H. Hayashi, and T. Yokoyama: "Relationship Between Particle's Splat Pattern and Coating Adhesive Strength of HVOF Sprayed Cu-Alloy", J. Jpn. Therm. Spray Soc., 1995, 32-3, pp. 149-56 (in Japanese).

This paper deals with splat flattening.

74. L. Bianchi, A. Grimaud, F. Blein, P. Lucchese, and P. Fauchais: "Comparison of Plasma Sprayed Alumina Coatings by RF and DC Plasma Spraying", J. Therm. Spray Technol., 1995, 4(1), pp. 59-66.

This paper deals with splat flattening.

75. N. Sakakibara, H. Tsukuda, and A. Notomi: "The Splat Morphology of Plasma Sprayed Particles and the Relation to Coating Properties", in Thermal Spray: Surface Engineering via Applied Research, C.C. Berndt, ed., ASM International, Materials Park, OH, 2000, pp. 753-58.

This paper deals with splat flattening.

76. L. Pershin, M. Lufitha, S. Chandra, and J. Mostaghimi: "Effect of Substrate Temperature on Nickel Coating Adhesion", in 15th Int. Symposium on Plasma Chemistry, Vol. 6, A. Bouchoule, J.M. Pouvesle, A.L. Thomann, J.M. Bauchire, and E. Robert, ed., GREMI, CNRS, Univ. of Orléans, France, 2001, pp. 2633-37.

This paper deals with splat flattening.

77. S. Safai and H. Herman: "Microstructural Investigation of Plasma Sprayed Aluminum Coatings", Thin Solid Films, 1977, 45, pp. 295-307.

This paper deals with splat flattening.

78. S. Sampath and H. Herman: "Rapid Solidification and Microstructure Dependent During Plasma Spray Deposition", J. Therm. Spray Technol., 1996, 5(4), pp. 445-56.

This paper deals with splat flattening.

79. S. Inada and W.J. Yang: "Solidification of Molten Metal Droplets Impinging on a Cold Surface", Exp. Heat Transfer, 1994, 7(2), pp. 93-100.

    This paper deals with splat flattening.

80. J. Mostaghimi, M.P. Fard, and S. Chandra: "Dynamics of Splat Formation in Plasma Spray Coating Process", Plasma Chem. Plasma Proc., 2002, 22(1), pp. 59-84.

    This paper deals with splat flattening.

81. M. Fukumoto, Y. Huang, and M. Ohwatari: "Flattening Mechanism in Thermal Sprayed Particle Impinging on a Flat Surface", in Thermal Spray: Meeting the Challenge of the 21st Century, C. Coddet, ed., ASM International, Materials Park, OH, 1998, pp. 401-07.

    This paper deals with splat flattening.

82. M. Fukumoto, E. Nishioka, and T. Matsubara: "Effect of Interface Wetting on Flattening of Freely Fallen Metal Droplet Onto a Flat Substrate Surface", in Thermal Spray: Surface Engineering Via Applied Research, C.C. Berndt, ed., ASM International, Materials Park, OH, 2000, pp. 797-802.

    This paper deals with splat flattening.

83. M. Fukumoto, E. Nishioka, and T. Nishiyama: "Proposal for New Criterion for Splashing of Thermal Sprayed Particle Onto a Flat Substrate", in Thermal Spray 2001, New Surface for a New Millenium, C.C. Berndt, K.A. Khor, and E.F. Lugscheider, ed., ASM International, Materials Park, OH, 2001, pp. 841-48.

    This paper deals with splat flattening.

84. M. Fukumoto, T. Nishiyama, and E. Nishioka: "Effect of Surface Morphology of Substrate on Flattening Behavior of Freely Fallen Metal Droplet", in Proc. Int. Thermal Spray, Conf. Essen 2002, E. Lugscheider, ed., DVS, Düsseldorf, Germany, 2002, pp. 37-41.

    This paper deals with splat flattening.

85. N.Z. Mehdizadeh, S. Chandra, and J. Mostaghimi: "Effect of Substrate Temperature and Roughness on Coating Formation", in Proc. Int. Thermal Spray Conf., Essen 2002, E. Lugscheider, ed., DVS, Düsseldorf, Germany, 2002, pp. 830-37.

    This paper deals with splat flattening.

86. Y. Huang, M. Ohwatari, and M. Fukumoto: "Effect of Substrate Material on Flattening Behavior of Plasma Sprayed Ni Particles", in Proc. 6^{th} Int. Symposium, Japan Welding Society, Osaka, Japan, 1996, pp. 731-36.

This paper deals with splat flattening.

87. M. Fukumoto and Y. Huang: "Flattening Mechanism in Thermal Sprayed Ni Particles Impinging on Flat Substrate Surface", J. Therm. Spray Technol., 1999, 8(3), pp. 427-32.

    This paper deals with splat flattening.

88. Y. Tanaka and M. Fukumoto: "Investigation of Dominating Factors on Flattening Behavior of Plasma Sprayed Ceramic Particles", Surf. Coat. Technol., 1999, 120-121, pp. 124-30.

    This paper deals with splat flattening.

89. Y. Tanaka and M. Fukumoto "Influence of Solidification and Wetting on Flattening Behavior of Plasma Sprayed Ceramic Particles", Int. J. Mater. Product Technol., Special Issue, SPM1, 2001, pp. 518-23.

    This paper deals with splat flattening.

90. M. Fukumoto, E. Nishioka, and T. Matsubara: "Flattening and Solidification Behavior of Metal Droplet on Flat Substrate Surface Held at Various Temperatures", Surf. Coat. Technol., 1999, 120-121, pp. 131-37.

    This paper deals with splat flattening.

91. E. Nishioka, T. Matsubara, and M. Fukumoto: "Effect of Wetting at Splat/Substrate Interface on Flattening Behavior of Freely Fallen Droplet", Int. J. Mater. Product Technol., Special Issue, SPM1, 2001, pp. 700-05.

    This paper deals with splat flattening.

92. G. Montavon, S. Sampath, C.C. Berndt, H. Herman, and C. Coddet: "Effect of Vacuum Plasma Spray Processing Parameters on Splats", J. Therm. Spray Technol., 1995, 4(1), pp. 67-74.

    This paper deals with splat flattening.

93. A. Vardelle, N.J. Themelis, M. Vardelle, and P. Fauchais: "Transport and Chemical Rate Phenomena in Plasma Sprays", J. High Temp. Mater. Proc., 1997, 1(3), pp. 295-314.

    This paper deals with splat flattening.

94. K. Nogi, N. Iwamoto, and K. Ogino: "Wetting Mechanism of Ceramics by Liquid Metals", Bull. Japan Inst. Metals, 1992, 31(4), pp. 278-81.

    This paper deals with splat flattening.

95. K. Suganuma: "Interface Binding Energy and Strength of Metal/Ceramic Joint",

Bull. Japan Inst. Metals, 1990, 29(11), pp. 882-87.

This paper deals with splat flattening.

96. P. Gougeon and C. Moreau: "Simultaneous Independent Measurements of Splat Diameter and Cooling Time During Impact on A Substrate of Plasma Sprayed Molybdenum Particles", J. Therm. Spray Technol., 2001, 10(1), pp. 76-82

This paper deals with splat flattening.

97. W. Liu, G.X. Wang, and E.F. Matthys: "Thermal Analysis and Measurements for a Molten Metal Drop Impacting on a Substrate: Cooling, Solidification and Heat Transfer Coefficient", Int. J. Heat Mass Transfer, 1995, 38(8), pp. 1387-95.

This paper deals with splat flattening.

98. W. Hofmeister and R.J. Bayuzick: "Observation of Thermal Profiles During Impact and Solidification of Nickel Droplets", in Solidification 1998, S.P. Marsh et al., ed., The Minerals, Metals and Materials Society, Warrendale, PA, 1998, pp. 375-87.

This paper deals with splat flattening.

99. T. Bennett and D. Poulikakos: "Heat Transfer Aspects of Splat- Quench Solidification: Modeling and Experiment", J. Mater. Sci., 1994, 29, pp. 2025-39.

This paper deals with splat flattening.

100. X.Y. Jiang, Y.P. Wan, X.Y. Wang, H. Zhang, R. Goswami, H. Herman, and S. Sampath: "Investigation of Splat/Substrate Contact During Molybdenum Thermal Spraying", in Thermal Spray: Surface Engineering via Applied Research, C.C. Berndt, ed., ASM International, Materials Park, OH, 2000, pp. 729-36.

This paper deals with splat flattening.

101. C.-J. Li, J.-L. Li, W.-B. Wang, A. Ohmori, and K. Tani: "Effect of Particle-Substrate Material Combinations on Morphology of Plasma Sprayed Splats", in Thermal Spray: Meeting the Challenges of the 21st Millenium, C. Coddet, ed., ASM International, Materials Park, OH, 1998, pp. 481-80.

This paper deals with splat flattening.

102. C.-J. Li, J.-L. Li, and W.B. Wang: "The Effect of Substrate Preheating and Surface Organic Covering on Splat Formation", in Thermal Spray: Meeting the Challenges of the 21st Century, C. Coddet, ed., ASM International, Materials Park, OH, 1998, pp. 473-80.

This paper deals with splat flattening.

103. C.-J. Li, J.-L. Li, W.B. Wang, A.-J. Fu, and A. Ohmori: "A Mechanism of the Splashing During Droplet Splatting", in Thermal Spraying in United Spray Confe-

rence Proc. Düsseldorf (1999), E. Lugscheider and P.A. Kammer, ed., DVS, Düsseldorf Germany, 1999, pp. 530-35.

This paper deals with splat flattening.

104. X. Jiang, Y. Wan, H. Herman, and S. Sampath: "Role of Condensates and Adsorbates on Substrate Surface on Fragmentation of Impinging Molten Droplets During Thermal Spray", Thin Select Films, 2001, 385(1–2), pp. 132–61.

This paper deals with splat flattening.

105. V. Pershin, M. Pasandideh-Fard, J. Mostaghimi, and S. Chandra: "Effect of Substrate Properties on the Formation of Plasma Sprayed Alumina Splats", in Thermal Spray 2001: New Surfaces for a New Millenium, C.C. Berndt, K.A. Khor, and E.F. Lugscheider, ed., ASM International, Materials Park, OH, 2001, pp. 813-20.

This paper deals with splat flattening.

106. Maitre, A., Denoirjean, A., Fauchais, P., and Lefort, P. (2002). Phys. Chem. Chem. Phys. 15(4), 3887.

This paper deals with splat flattening and adhesion.

107. Valette, S., Denoirjean, A., Lefort, P., and Fauchais, P. (2003). J. High Temp. Mater. Process. 7(2), 195.

This paper deals with splat flattening and adhesion.

108. Pech, J., Hannoyer, B., Lagnoux, O., Denoirjean, A., and Fauchais, P. (1999). In "Progress in Plasma Processing of Materials" (P. Fauchais and J. Amouroux, eds.), p. 543. Begell House, New York.

This paper deals with splat flattening and adhesion.

109. Valette, S., Denoirjean, A., Soulestin, B., Trolliard, G., Hannoyer, B., Lefort, P., and Fauchais, P. (2004). Alumina coatings on preoxidized low carbon steel. Interfacial phenomena between alumina and iron oxide layer. In "Proceedings of the International Thermal Spray Conference", Osaka, DVS Düsseldorf, Germany (electronic version).

This paper deals with splat flattening and adhesion.

110. Haure, T. (2003). Multifunctional layers by PACVD and Plasma Spraying, Ph.D. Thesis, University of Limoges, France, 14 November.

This paper deals with splat flattening and adhesion.

111. Espié, G., Fauchais, P., Hannoyer, B., Labbe, J. C., and Vardelle, A. (1999). In "Heat and Mass Transfer under Plasma Conditions during the APS on the Wettability" P. Fauchais, et al., eds.), Vol. 891, p. 143. N.Y. Academy of Sciences, NY,

USA.

This paper deals with splat flattening and adhesion.

112. Seyed, A. A., Denoirjean, P., Denoirjean, A., Hannoyer, B., Labbe, J. C., and Fauchais, P. (2000). In "Progress in Plasma Processing of Materials" (P. Fauchais, ed.), p. 465. Begell House, NY, USA.

This paper deals with splat flattening.

113. Pech, J., Hannoyer, B., Denoirjean, A., Bianchi, L., and Fauchais, P. (1999). Influence of substrate preheating monitoring on alumina splat formation in d.c. plasma processes. In "Thermal Spray: A United Forum for Scientific and Technological Advances" (C.C. Berndt, ed.), pp. 759–765. ASM International, Materials Park, OH, USA.

This paper deals with splat flattening.

114. Pech., J., Hannoyer, B., Lagnoux, O., Denoirjean, A., and Fauchais, P. (1999). Influence of preheating parameters on the plasma jet oxidation of a low-carbon steel. Progress in Plasma Processing of Materials, (P. Fauchais and J. Amouroux, eds.), pp. 543–554. Pub. Begell House, NY, USA.

This paper deals with splat flattening.

115. Thermal spraying: Practice, theory and application, prepared by AWS Committee on Thermal Spray (1999). American Welding Society, Miami, FL, USA, pp. 2-15.

This paper deals with splat flattening.

116. Haure, T., Denoirjean, A., Tristant, P., Hidalgo, H., Leniniven, C., Desmaison, J., and Fauchais, P. (2001). In "Thermal Spray 2001: New Surfaces for a New Millenium" (C.C. Berndt, K.A. Khor and E. Lugscheider, eds.), p. 613. ASM International, Materials Park, OH, USA.

This paper deals with splat adhesion.

117. Pawlowski, L. (1995). "The Science and Engineering of Thermal Spray Coatings". John Wiley, New York, NY, USA.

This paper deals with splat adhesion.

118. Haure, T., Denoirjean, A., Tristant, P., Hidalgo, H., Leniniven, C., Desmaison, J., and Fauchais, P. (2001). In "Thermal Spray 2001: New Surfaces for a New Millenium" (C. C. Berndt, K.A. Khor and E. Lugscheider, eds.), p. 613. ASM International, Materials Park, OH, USA.

This paper deals with splat adhesion.

119. Bianchi, L., Leger, A. C., Vardelle, M., Vardelle, A., and Fauchais, P. (1997). Thin

Solid Films 305, 35.

This paper deals with splat adhesion.

120. Bianchi, L., Denoirjean, A., Blein, F., and Fauchais, P. (1997). Thin Solid Films 299, 125–135.

This paper deals with splat adhesion.

121. Leger, A. C., Vardelle, M., Vardelle, A., Dussoubs, B., and Fauchais, P. (1995). Splat formation: Ceramic particles on ceramic substrate. In "Thermal Spray: Science and Technology" (C.C. Berndt and S. Sampath, eds.), pp. 169–177. ASM International, Materials Park, OH, USA.

This paper deals with splat adhesion.

122. Haddadi, A., Nardou, F., Grimaud, A., and Fauchais, P. (1995). Generation of the first layers of a zirconia plasma sprayed coating: Correlation between splat layering and spraying parameters. In "Thermal Spray: Science and Technology" (C.C. Berndt and S. Sampath, eds.), pp. 249–254. ASM International, Materials Park, OH, USA.

This paper deals with splat adhesion.

123. Valette, S. (2004). Influence of the Preoxidation of a Steel Substrate on the Adhesion of an Alumina Coating d.c. Plasma Sprayed, PhD. Thesis, University of Limoges, 30 November.

This paper deals with splat adhesion.

124. Zanchetta, A., Lefort, P., and Gabbay, E. (1995). J. Eur. Ceram. Soc. 15, 238.

This paper deals with splat adhesion.

125. Smith, M. F., Neiser, R. A., and Dykhuisen, R. C. (1994). An investigation of the effects of droplet impact angle in thermal spray deposition. In "Thermal Spray: Industrial Applications" (C.C. Berndt and S. Sampath, eds.), pp. 603–608. ASM International, Materials Park, OH, USA.

This paper deals with splat adhesion.

126. Denoirjean, A., Grimaud, A., Fauchais, P., Tristant, P., Tixier, C., and Desmaison, J. (1998). Splat formation first step of multitechnique deposition plasma spraying and microwave plasma enhanced CVC. In "Thermal Spray: Meeting in Challenges of the 21st Century" (C. Coddet, ed.), Vol. 2, pp. 1369–1374. ASM International, Materials Park, OH, USA.

This paper deals with splat adhesion.

127. Mifune, N. & Harada, Y. Mechanism of Vertical Microcracking in $CaOSiO_2$ - CaOZr

O_2. Sprayed Thermal Barrier Top Coating. 2004, Materials Transactions, 4(5), pp. 1788-1793.

This paper deals with issues related to the influence of flattening and solidification process in the appearance of splat cracks.

128. Wenzelburger, M. Escribano, M. & Gadow, R. Modeling of thermally sprayed coatings on light metal substrates: layer growth and residual stress formation. 2004, Surface and Coatings Technology, 180–181, pp. 429–435.

This paper deals with issues related to the plasma spray process parameters and its contention with residual stresses and their generation mechanisms.

129. Kulkarni, A.A., Goland, A., Herman, H., Allen, A.J., Ilavsky, J., Long, G.G. & De Carlo, F. Advanced Microstructural Characterisation of Plasma spraying. 2004, Journal of Thermal Spray Technology, 14(2), pp. 238-250.

This article describes the quantitative characterisation of the microstructure of plasma-sprayed particles by means of some imaging techniques.

130. M. Buchmann, R. Gadow, A. Killinger, J. Tabellion. Residual Stress Optimization of Thermally Sprayed Ceramic Coatings on Light Metal Components. 2000, R. Gadow (ed.), Advanced Ceramics and Composites, 6th Interregional European Colloquium on Ceramics and Composites, expert-Verlag, Renningen, pp. 268–281.

This paper deals with issues related to the plasma spray process parameters and its contention with residual stresses.

131. David, J. R. Handbook of Thermal Spray Technology. 2004, New York, ASM International, p. 123.

This book provides general information, which contains from the atmospheric plasma spray process to the splat characterisation.

132. Ohmori, A. & Li, C-J. The structure of thermally sprayed ceramic coatings and its dominant effect on the coating properties. 1993, Plasma Spraying, theory & applications (ed.) Surayanarayanam, World Scientific Publishing CO., pp. 179-200.

This reference provides general information, which contains from the basis of the APS process to the characterisation of the structure of alumina coatings and its effect on coating properties.

133. Sharmila M. Mukhopadhyay: “Sample preparation for microscopic and spectroscopic characterization of solid surfaces and films”, Department of Mechanical and Materials Engineering, Wright State University, Dayton, Ohio, ed JOHN WILEY & SONS, INC., 2003, pp 377-411.

This book has a useful chapter related to the sample preparation.

134. University of Glasgow, Imaging Spectroscopy & Analysis Centre (ISAAC): https://www.gla.ac.uk/schools/ges/researchandimpact/researchfacilities/isaac/services/scanningelectronmicroscopy/

This website contains information about how scanning electron microscopy works.

135. Goldstein, J. et al. Scanning Electron Microscopy and X-Ray Microanalysis. Springer. 2003.

A lot of very distinct images and schematic drawings make for a very interesting book and help readers who study scanning electron microscopy and X-ray microanalysis. The principal application and sample preparation given in this book are suitable for undergraduate students and technicians learning SEEM and EDS/WDS analyses. It is an excellent textbook for graduate students, and an outstanding reference for engineers, physical, and biological scientists.

136. Y. Tanaka a, M. Fukumoto: "Investigation of dominating factors on flattening behavior of plasma sprayed ceramic particles", in Technology Development Center, Toyohashi University of Technology, Japan, Department of Production Systems Engineering, Toyohashi University of Technology, Japan, ed Elsevier, 1999, pp 124-130.

In this study, the effects of the substrate, powder and pre-coating by PVD on the flattening of the plasma sprayed ceramic particles were investigated.

137. Brundle, C. R., Evans Jr., C. A., Wilson, S. and Fitzpatrick, L. E. eds. Encyclopaedia of Materials Characterization: Surfaces, Interfaces, Thin Films. 1992, Butterworth-Heinemann, Woburn, MA.

This book describes analytical techniques for the characterization of solid materials, with emphasis on surfaces, interfaces, thin films, and microanalytical approaches.

138. Fieldman, L. C. and Mayer, J. W. Fundamentals of Surface and Thin Film Analysis. 1986, Prentice Hall, Englewood Cliff, NJ.

This book discusses the physics underlying the techniques used to analyse the surface region of materials. It addresses the fundamentals of the few processes that govern the interactions of particles and radiation with matter.

139. Wacthman, J. B. Characterization of Materials. 1985, Butterworth-Heinemann, Woburn, MA.

This book covers the major techniques increasingly used by physical scientists and engineers working on and with materials. It offers a solid coverage of a broad range of techniques, explaining their foundations, discussing their capabilities and limitations, and teaching their vocabulary.

140. W. D. Kingery, H. K. Bowen, and D. R. Uhlman, Introduction to Ceramics, Wiley, New York, 1976.

This book provides useful information for understand the development, use, and control of the properties of ceramics from the point of view of physical ceramics.

141. B. L. Gabriel, SEM: A User's Manual for Materials Science, ASM International, Metals Park, OH, 1985.

This book provides a reference of techniques used by the metallurgical microscopist. It contains an introduction to the instrumentation and methods of scanning electron microscopy with historical as well as state-of-the-art methodologies. Topics covered include: SEM instrumentation, photography, energy dispersive spectroscopy, introduction to sample preparation, polished samples, fracture surfaces, replicas and thin films.

142. MathWorks, image processing toolbox, 1994-2016 The MathWorks, Inc, [24/05/17]: `http://es.mathworks.com/help/images/index.html`

This website is useful for the routine implement using this commercial software.

143. Costa, M. F. M. Image Processing. Application to the characterisation of thin films. 2011, Journal of Physics: Conference Series, 274(1): 012053.

This paper deals with issues related to image processing in the qualitative and quantitative characterisation of the porosity of thermal barrier coatings.

144. Acharya, T. & Ray, A.K. Image Processing: Principles and Applications. Wiley InterScience.

This book deals with image processing from basics to advanced applications.

145. SANTO, coated abrasives, understanding coated abrasives, Abrasive grade/Grit size, [29/06/17]: `http://santo-abrasives.com/abrasive-grade-grit-size`

This website provides useful information for the handle of abrasive plate.

Chapter 4

Methods

4.1 Introduction

This chapter deals with the experimental procedures followed in this study and the development of the applied routines. The details of the processes are outlined here.

4.2 Material selection and spray parameters

Firstly, five samples were prepared, which were manufactured in Institute for Manufacturing Technologies of Ceramic Components and Composites (IFKB) from University of Stuttgart. Each sample consisted of a stainless-steel bar coated on both sides, three clusters of splats in form of circle were deposited on each side (six clusters in each sample), which were enumerated according to the Figure 4.1.

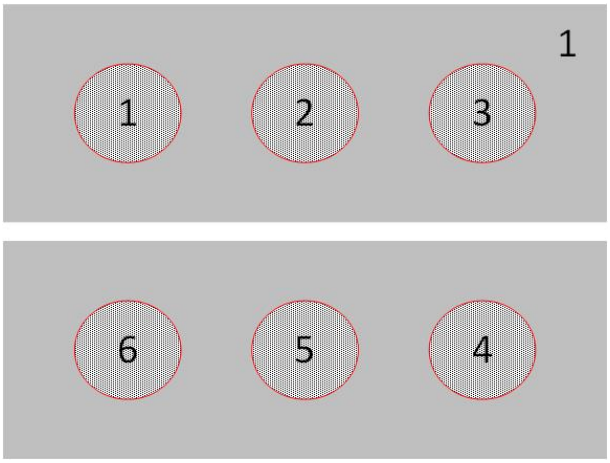

Figure 4.1: Enumeration of the clusters on the samples

The splat spraying parameters required to obtain the samples are 130 mm for torch

standoff distance and 500 mm/s for the torch velocity and the following currents: 550 A (samples 2 and 4) and 600 A (samples 1, 3 and 5). The substrate was not preheating.

The carrier gas parameters are 40 l/min for Argon and the following flows for the H_2: 12 l/min (samples 1, 3 and 5) and 8 l/m (samples 2 and 4).

Al_2O_3 powder sizes used are: -20+5 (samples 1 and 2) and -40+10 μm (sampes 3, 4 and 5). The powder was supplied with a angular velocity of 1 rpm, except to the face A in the sample 5 (0.5 rpm), and it contained Argon, supplied with a flow of 5 l/min for the five samples.

In order to depict the mean shape pattern followed by the powder an image is showed, Figure 4.2. As can be seen, the powder particles do not have a round shape hence the result of the spray process could provide an irregular splat. Nevertheless, it is expected that these go through the gun plume and develop a round shape if the heat release allows them melting their entire structure.

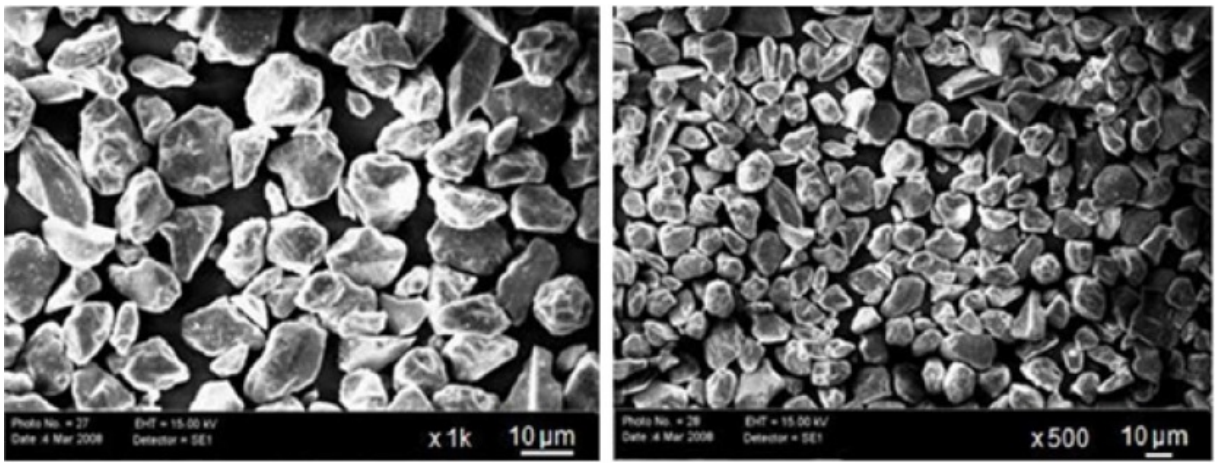

Figure 4.2: Alumina powder used for the coating spray process [136]

The changing of the main spray process parameters such as the gas feed rate or the power input provide different splat morphology. Hence the weakest power supply results in a lower temperature and the weakest gas feed rate results in a lower speed rate.

4.3 Technical procedure

A mask is used in order to get the individual splats, Figure 4.3. The mask has four groups of three holes. Each group of three holes covers a portion of a plate, which will be cut to produce one sample. The system produces individual splats with a wide range of deposition velocities, because of the fly angle of the droplet when they enter in one of the mask holes. A structure to support and place the mask and the plate is shown in Figure 4.4.

The process is realized with a spray gun moving over the mask, hence a white straight line marked over the mask is created, Figure 4.3. Besides, it is claimed that the amount of droplets that pass through the mask depend on the torch speed. Hence if it is required a major quantity of splats to be analysed the torch speed will have to decrease. However, a higher number of splats means a higher overlapping likelihood.

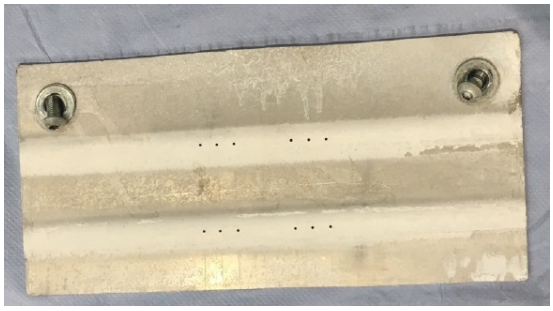

Figure 4.3: Mask with straight white alumina line

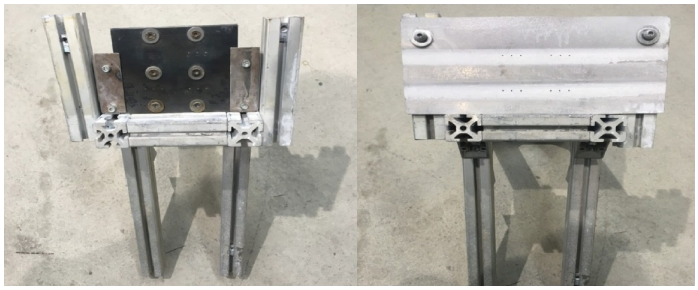

Figure 4.4: Structure to support and place the mask and the plate

Once the plate is sprayed a cut process of the samples is realized, Figure 4.5.

Figure 4.5: Sample bar cut with the low speed saw

In order to analyse the splat section, the samples, in turn, must be cut. With the help of an optical microscope, a sign maker provides a signal close to splats circle. A scratch is made on the signal by a roller cutter. Figure 4.6 shows the ISOMET saw machine.

Figure 4.6: ISOMET saw machine and detail of the cutting disk

Figure 4.7 shows the DigiMicro Profi optical microscope.

Figure 4.7: DigiMicro Profi optical microscope

The characteristics of ISOMET saw machine are:

- Low speeds, 0-300 rpm.
- Gravity fed specimen for repeatability.
- Adjustable cutting loads with 25 grams weights.
- Precision Micrometer for specimen alignment, ± 5 μm or ± 0.0001 in positioning via manual micrometer.
- Versatile chucks available for irregular specimens.
- Power: 14.72 W.

The next step is the section polishing. Since the scratch is close enough to the splats, the polishing time is small and no additional preventive measure are necessary relative to the velocity calculations. The figure 4.8 shows the grinder polisher.

Figure 4.8: A BUEHLER grinder polisher model MetaServ 250 [145]

Figure 4.9 shows the gripper designed to fit the sample during the polishing.

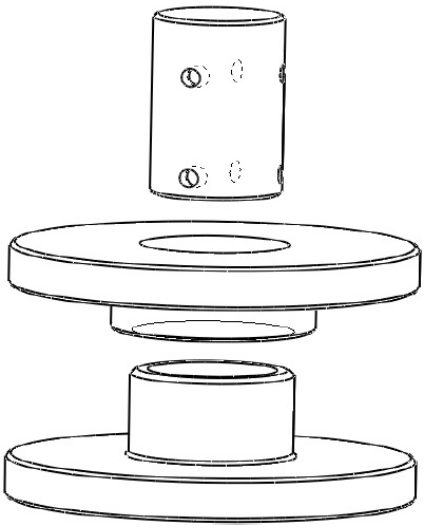

Figure 4.9: Gripper designed to fit the sample during the polishing

Once the sample has been cut its cross-section is polished using SiC abrasive papers. The grit sizes are reducing in the following steps: 240, 600 and 1200 European P-grades mesh. Finally, a diamond paste of 1 μm on a wheel at low revolutions is used. The target of this procedure is to get a clean splat section.

During the polishing, several pictures of the sample edge are taken, Figure 4.10. These pictures allow us to control the polishing. The time necessary to take apart the polished sample, clean it with alcohol and use the optical microscope is two minutes. Therefore, frequent controls can be done in order to avoid missing the splats.

The portable microscopy has been used to mark the splat section in the sample section, Figure 4.11. This mark is useful to find it out with the SEM.

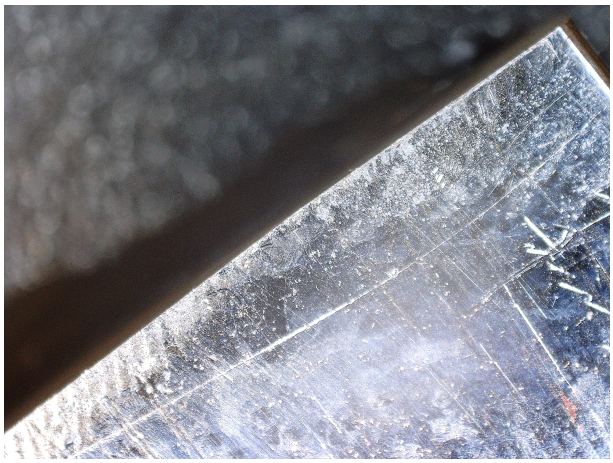

Figure 4.10: Picture taken during the polishing

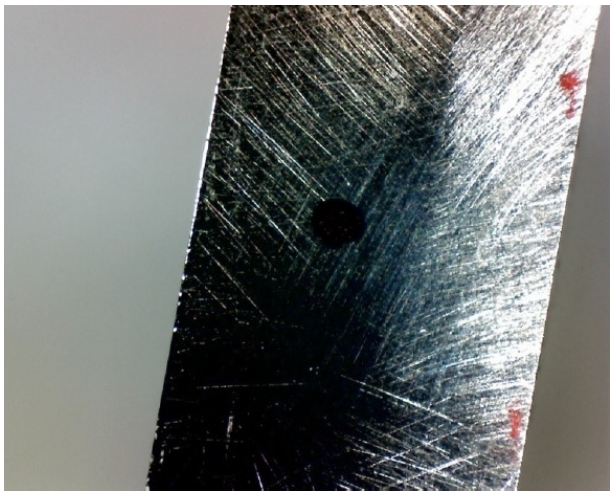

Figure 4.11: Mark over the sample section

4.4 Splat morphology and microstructure

We can classify splat categories in: disk splats, fingered splat, halo splat, halo fingered splat, halo doughnut splat, and fragmented splat.

Splat morphology can be quantified in terms of its circularity, its equivalent diameter and area.

MatLab provides a command in order to determine a circle, evaluated by its diameter, which has the same area as the region that represents the splat. This value is computed as

$$D_{equi} = \sqrt{\frac{4 \cdot Area}{\pi}}$$

Before applying this command, it is necessary to clean the object out of the splat and transforms its colour in white and the background in black, the filling image. This operation is obtained by a programme.

Another function converts the grayscale image to a binary image. If the pixels have luminance greater than the value defined as threshold, this value is changed to 1 (equivalent to white), otherwise the value is changed to 0 (equivalent to black).

The following sentence computes a global threshold that can be used to convert an intensity image to a binary image with the use of the suitable argument. This function uses Otsu's method, which chooses the threshold to minimize the intraclass variance of the black and white pixels.

Next, another sentence performs morphological closing on the grayscale or binary image, with the use of the suitable argument, a structuring element, returning the closed image. The structuring element must be a single object, as opposed to an array of objects. This element is obtained by a function which preserves the disk nature of the object and creates a disk-shaped structuring element, using the second argument, ranged from 0 to 10, which specifies the radius. Morphological operations using disk sets-up run much faster when the structuring element uses approximations. The morphological close operation is a dilation followed by an erosion, using the same structuring element for both operations.

In order to explain the process, we select one of the most complex splat morphologies, the doughnut.

These operations are applied in a SEM image, Figure 4.12, obtaining Figure 4.13.

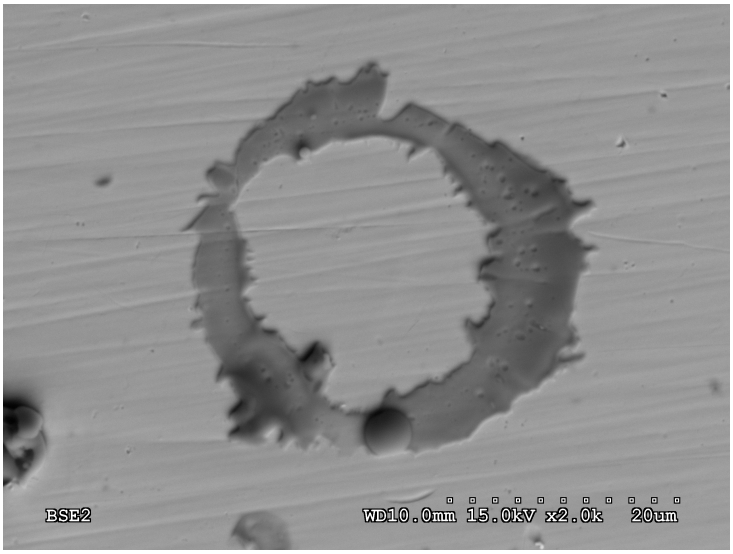

Figure 4.12: Original figure

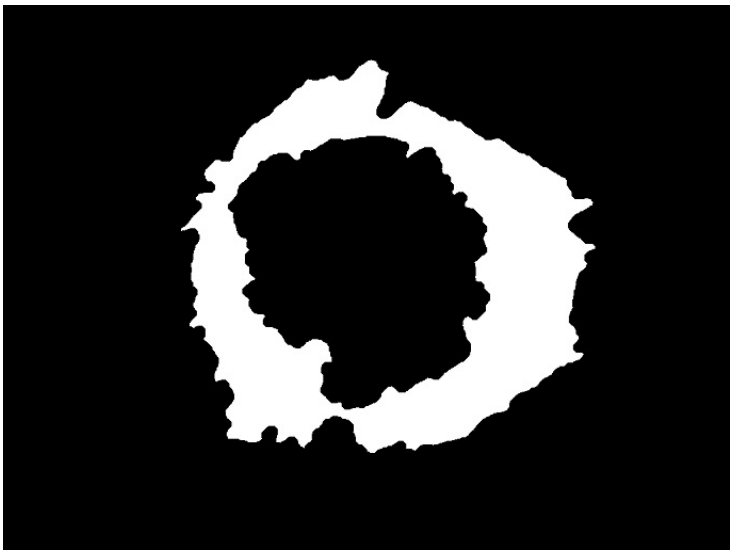

Figure 4.13: Filling image

The diameter diameter of the black figure surrounded by a white area cannot be calculated before the outer black area.

From Figure 4.13 and using the bucket fill of a raster graphics editor, it is possible to remove the black colour inside the splat inner contour. After that, a thin line, the border of the inner contour, is removed by the eraser of the editor. Then, the colour of the background is transformed to red, later, white colour is transformed to black and, finally, it is possible to transform the background colour to white without losing the splat, Figure 4.14. Hereafter, the programme has been run again using Figure 4.14.

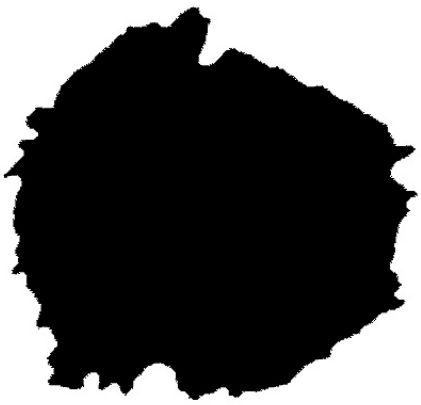

Figure 4.14: Selection of the splat outer contour

Finally, the equivalent diameter for the outer contour is available.

From Figure 4.13 and using the bucket fill of the editor used before, it is possible to select the inner splat contour in a white background, Figure 4.15. Hereafter, the programme has been run again using Figure 4.15, and obtaining the equivalent diameter for the inner contour.

Figure 4.15: Selection of the splat inner contour

According to these values we can classify each splat categories.

4.5 Image Processing Stages

The aim is to simplify a complex image, where heterogeneous objects are arranged in the background, in a matrix of vectors, where each vector corresponds to an object, and each component of the vector to a morphological property of that object. It is clear that to achieve our purpose we must simplify our problem step by step using the tools provided by Image Processing techniques. For example, stretching techniques are employed to improve the overall contrast in the image, thus the principal objects in the image become more apparent than the background. Threshold selection methods are used to obtain a binary image where there is a background and a foreground. Morphological operation is used to obtain segmented objects of that foreground. Labelling and feature extraction techniques are used to obtain some discriminatory features that can facilitate the splat characterisation. In our case, the automatic procedure involves four stages as shown in Figure 4.16.

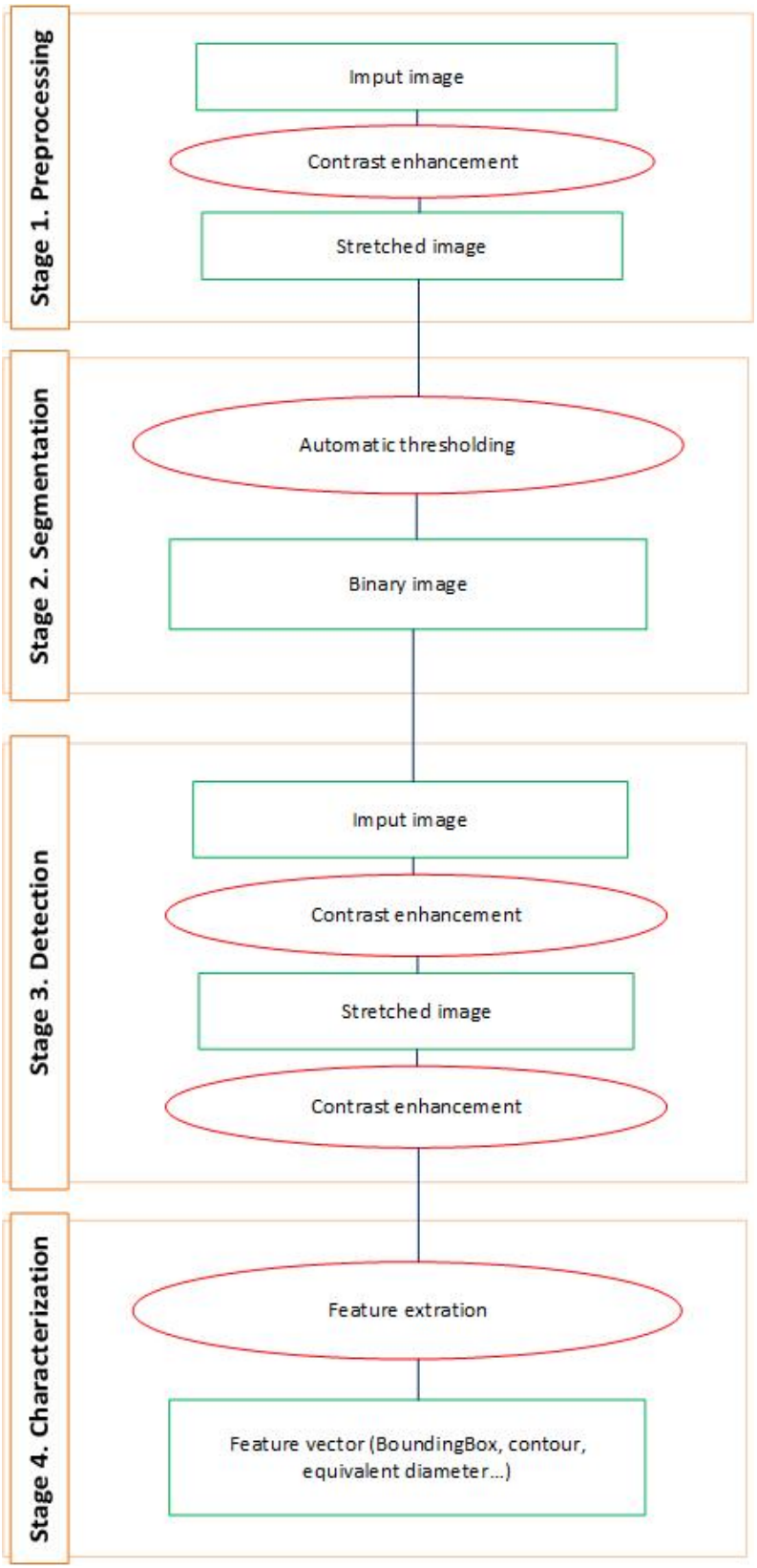

Figure 4.16: Software algorithm

First stage consists of a pre-processing stage where the SEM (Scanning Electron Microscope) image contrast is improved. Stage 2 performs segmentation stage which involves thresholding by means Otsu's method. Stage 3 carries out a detection stage where the binary image is processed by various morphological operations, labelling techniques, in order to obtain an image where the splat is labelled. Stage 4 involves an image analysis and characterisation stage where the segmented splat is characterised by means of techniques based on labelling connected components and features extraction. The input and output images can be seen in Figure 4.17.

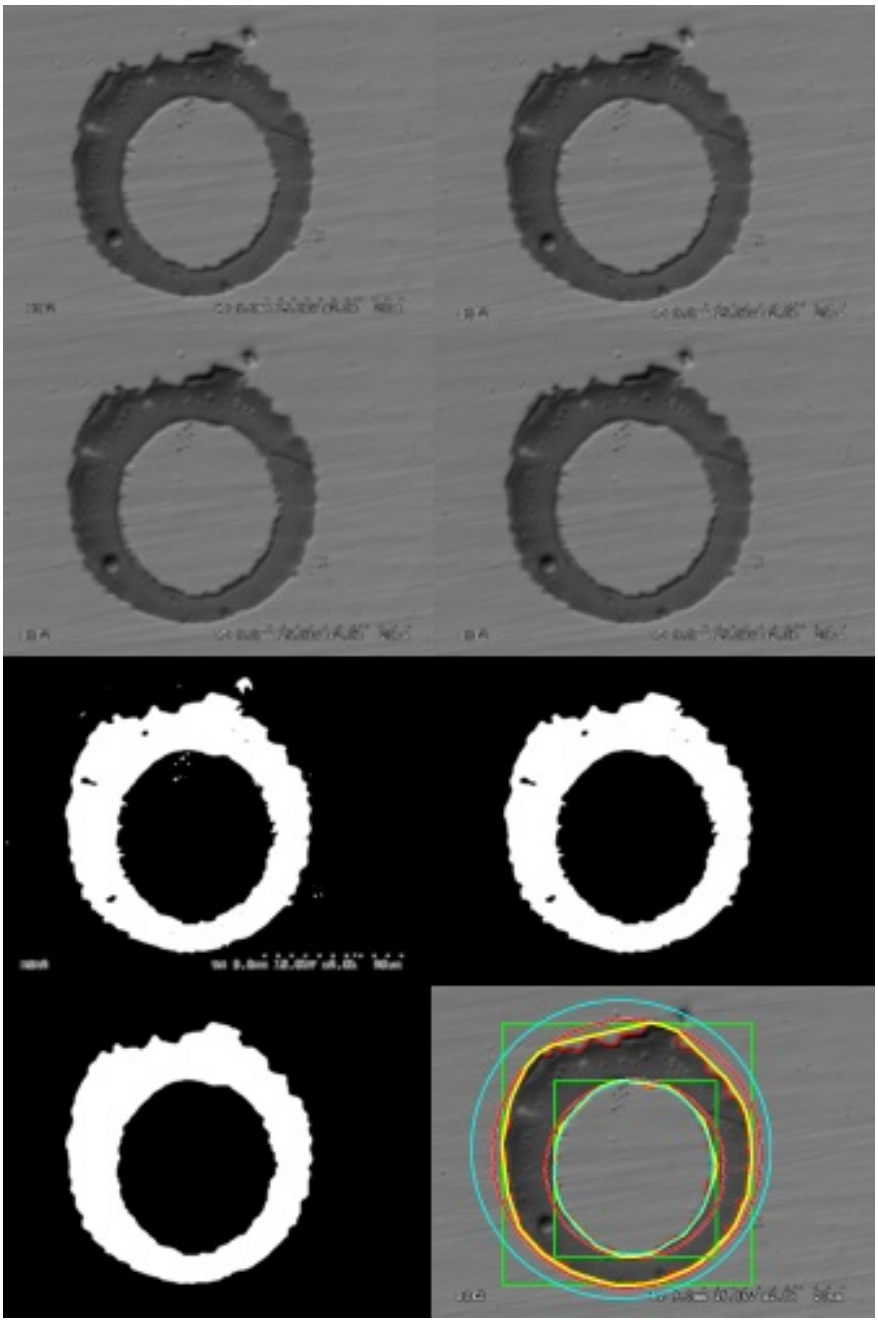

Figure 4.17: Procedure output images

In this work, the first stage or pre-processing stage is carried out by the application of a contrast enhancement procedure. The algorithm stretches the intensity value of the original image in a new transformed image, then the values of pixels are reassigned to cover the entire available range of the histogram. In other words, the values that represent the limit of the histogram between 1 % and 99 % of the total of the pixels are projected in the range of 0 to 1, while the rest of the values are clipped.

In the second stage or detection-splat stage, once the image has been enhanced in contrast, it is transformed from grey level, coded from 0 to 1; to binary, black or 0 (background) and white (foreground) or 1, in order to delimit objects placed in the background. This second stage must find an optimal overall threshold that converts the greyscale image to a binary one, and delimit splat boundaries. In our case, we have used the Otsu's method, which chooses the threshold to minimise the intraclass variance of the black and white pixels. The algorithm assumes that the image contains two classes of pixels following bi-modal histogram (foreground and background pixels), then it calculates the optimum threshold separating the two classes so that their combined spread (intra-class variance) is minimal, or equivalently (because the sum of pairwise squared distances is constant), so that their inter-class variance is maximal.

In the third stage the final binary objects obtained from the previous stage are labelled using a technique based on connected components. The implemented algorithm uses the general procedure proposed by Haralick and Shapiro. The algorithm returns a matrix of the same size as the input image containing labels for the 8-connected objects in the input image. The pixels labelled 0 are the background, the pixels labelled 1 represent one object, the pixels labelled 2 represent a second one, and so on. The procedure finds the object with maximum area because the splat is the object with maximum area due to our a priori knowledge. The rest of objects are refused easily labelling with 0 (background). The splat is then labelled with 1. The image is again binary which is composed with a background and the splat, defined by 1. Now, the binary image is subjected to different morphological operations. These operations apply a structuring element to an input image creating an output image of the same size. Dilation adds pixels to the objects boundaries in an image, while erosion removes pixels on these boundaries. The number of pixels added or removed from the objects depends on the size and shape of the structuring element used to process it and the own image. The rule used to process the pixels defines one operation or other. In a dilation, the value associated to the output pixel is the maximum value of all the pixels in the input pixel's neighbourhood. In an erosion, the value of the output pixel is the minimum value of all the pixels in the input pixel's neighbourhood. This procedure permits us to close splats boundaries.

In the fourth stage, and to the extent that our binary image is also a labelled image, we calculate the morphological properties of the splat. To be more precise, we are interested in boundaries (outer and inner), bounding box, and equivalent diameter and ellipse which fits to the splat. To sum up, a complex image, where heterogeneous objects are arranged in the background, is simplified in a vector, where the vector corresponds to splat object. Later, each component of the vector is simplified, in turn, to a morphological

property of that object.

4.6 Splat top view analysis

4.6.1 Contrast improvement (segmentation)

Each shade of gray is associated with a amount of pixels. The variety of gray is divided into two groups according to the amount of pixels of gray: one with few pixels and another one with many pixels of gray. The software add pixels to these grays with more pixels and take rid of pixels to these grays with less pixels.

4.6.2 Pores and particles deleting

The gray with less pixels in "Contrast improvement (segmentation)" is converted black and the gray with many pixels is converted white. It is used a mathematics function that recognises those white areas within black background. The contour is more regular.

4.6.3 Edges determination

The software draws the drop outline by points, it means that points are around drop and the joining make the outline.

4.6.4 Bounding box set-up

The software draws the minimum straight square which includes the drop. In this case, "straight" means the edges must be totally vertical or horizontal, this condition does not appear in "Adapted bounding box set-up", therefore the square is bigger in this case.

4.6.5 Circumscription process

The software draws the minimum circle which includes the drop.

4.6.6 Adjust by ellipse

The software draws the ordinary ellipse which includes the drop.

4.6.7 Adapted bounding box set-up

The software draw the minimum square (non-straight) which includes the drop, this square is smaller than that one made in "Bounding box set-up".

4.6.8 Adjust by polygon

With a naked eye, this picture is the same one that appears in "Edges determination", The difference is that the software draws the minimum polygon which includes the drop in this case.

4.6.9 Post processing

The software joins all the results above in the same picture.

4.7 Splat cross section analysis

The main procedures used to prepare the specimens for their analysis are reported here, thereby, a polishing is required before to be able to visualize the splat section.

As previous step to the polishing some cuttings more are realized to the metal sample in addition to those made in Stuttgart. That are the last cuttings over the plate; which allow adapting the sample at the different grippers, described in Section 4.5.

In order to realize a suitable splat section the suggested polishing process should be manual. Thus, the sample should be polished manually, putting pressure on it against the grid disk, being this process discontinue because of it should been looked over by microscope, every two minutes. This is a ineffective process so an improvement is required.

Chapter 5

Results and discussions

5.1 Introduction

In the previous chapter, the methodology procedures required to visualize and study the samples was described. Splats have been classified and their characteristics measured. All the test results belonging to the visual analysis (top and cross sections) of the splats are presented and discussed in this chapter.

Besides a preliminary splat section by SEM is made in order to know the internal splat structure.

5.2 Visual analysis: top sections

As mentioned in Section 4.6, the SEM images will be processed by the code named "splats.m".

The software is able to identify the splat contour, figures 5.1 to 5.6, that consist of doughnuts as well as pancakes. The order followed to analyse the splats is, firstly, those with a doughnut morphology and, later, the pancake morphology. Figure 5.1 shows the detected contour for a drop in the circle 1 from sample 3. Figure 5.2 shows the detected contour for a drop in the circle 3 from sample 3. Figure 5.3 shows the detected contour for a drop in the circle 5 from sample 4. Figure 5.4 shows the detected contour for a drop in the face marked with the characters "5A" from sample 5. Figure 5.5 shows the detected contour for a drop in the circle 1 from sample 4. Figure 5.6 shows the detected contour for a drop in the circle 2 from sample 1. Figure 5.7 shows the detected contour for a drop in the circle 3 from sample 2.

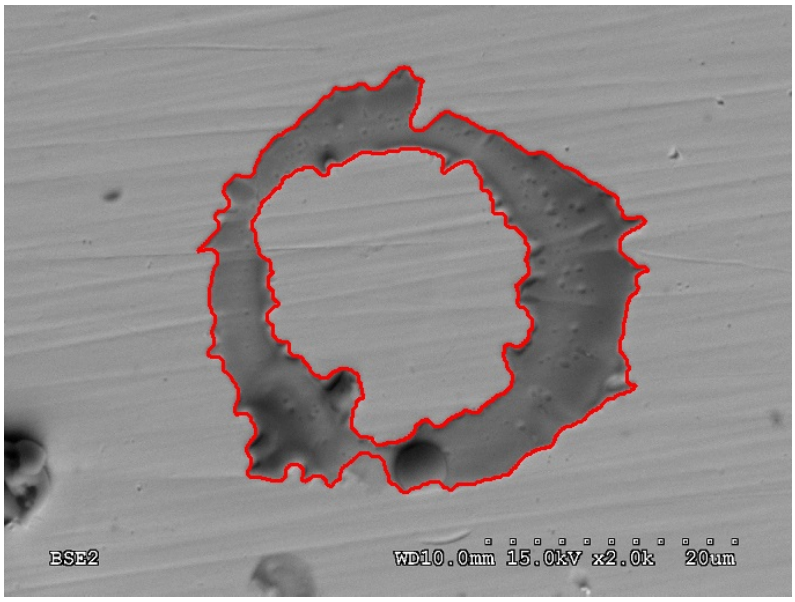

Figure 5.1: Doughnut splat contour from sample 3, cluster 1

In the bottom zone of the splat in Figure 5.1, the red curve does not follow the actual contour. It has lost a small part of the splat because it is very clear, probably due to the thinner thickness.

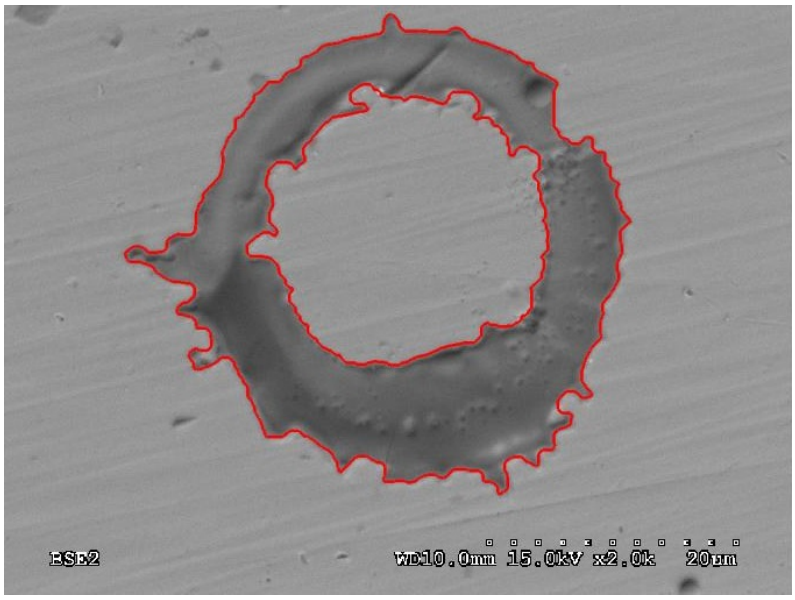

Figure 5.2: Doughnut splat contour from sample 3, cluster 1

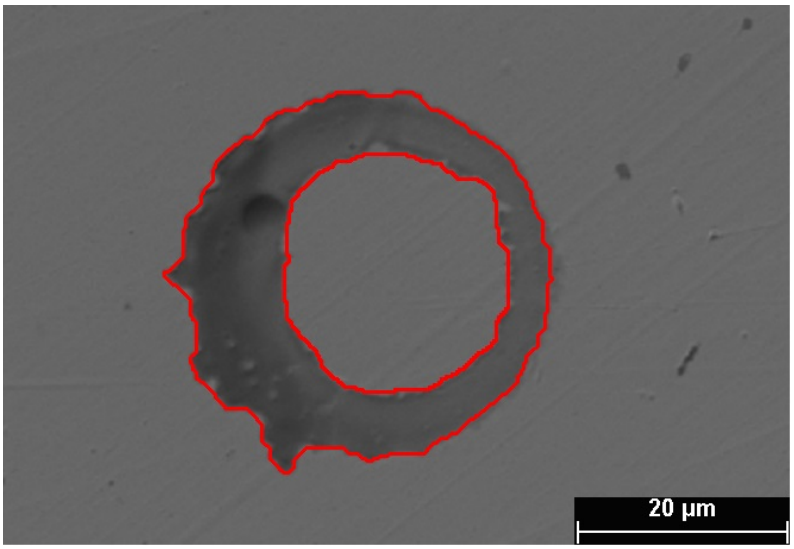

Figure 5.3: Doughnut splat contour from sample 4, cluster 5

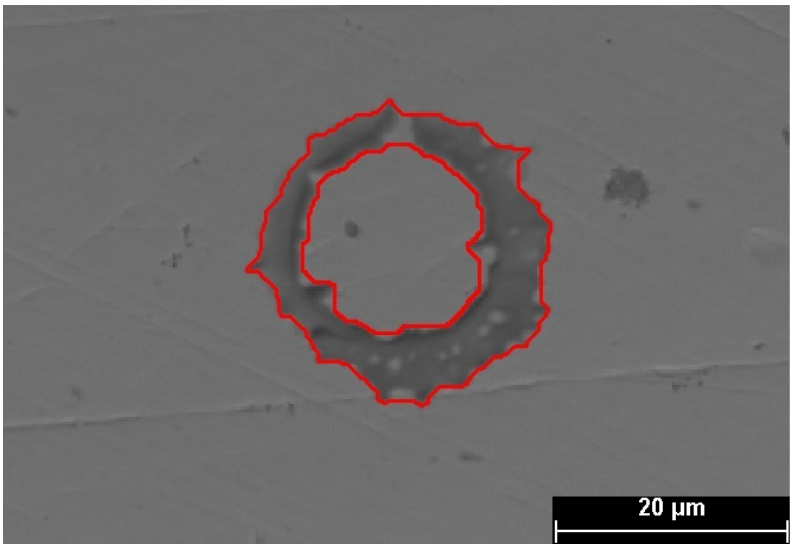

Figure 5.4: Doughnut splat contour from sample 5, face marked with the characters "5A"

In the upper zone of the splat in Figure 5.4, we obtain the same result as in Figure 5.1. In this event, the splat is not a perfect doughnut, thus the morphological closing operations on the grayscale provides an approximated contour which does not included the details of the small fingers in the actual contour.

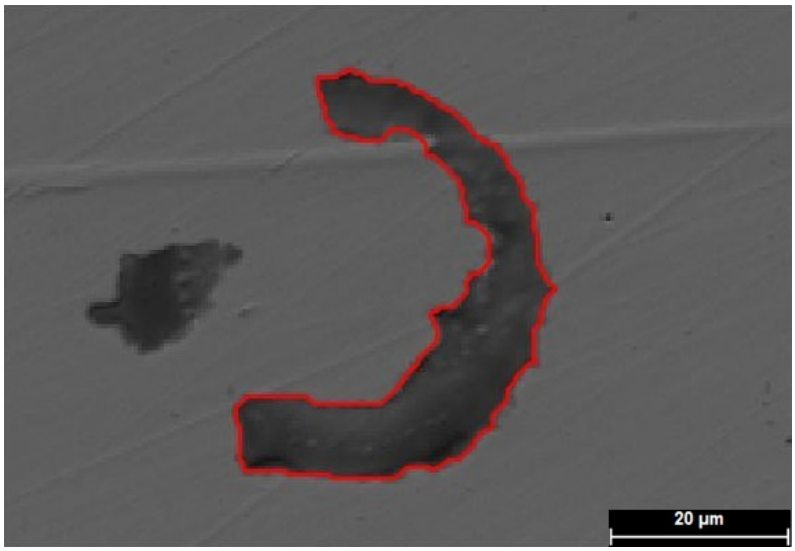

Figure 5.5: Doughnut splat contour from sample 4, cluster 1

Figure 5.5 shows a incomplete splats; therefore, the software can only draw a contour for each splat.

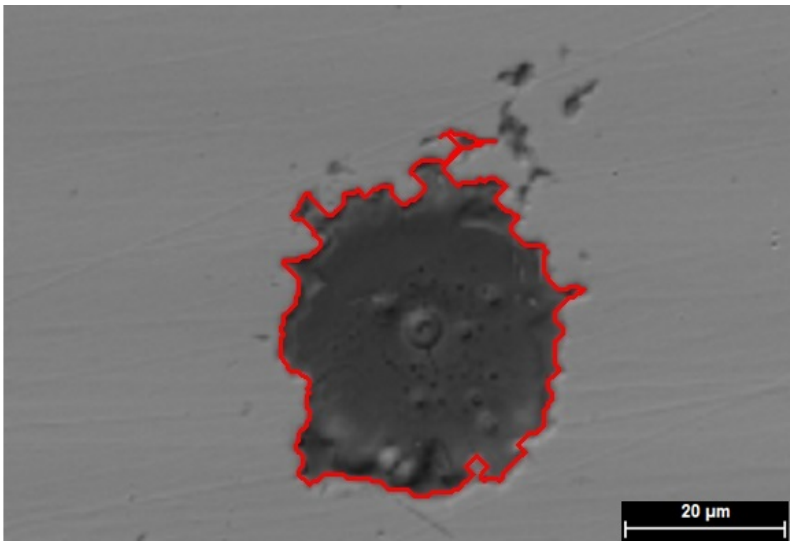

Figure 5.6: Pancake splat contour from sample 1, cluster 2

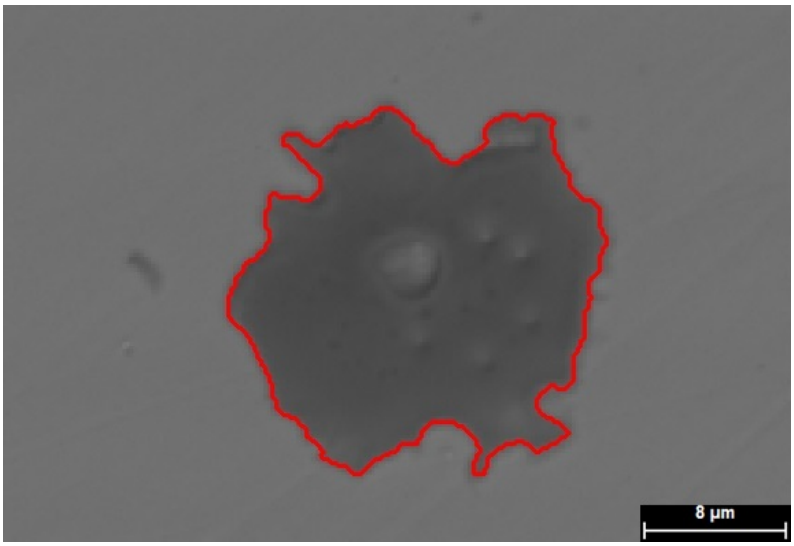

Figure 5.7: Pancake splat contour from sample 2, cluster 3

In the following sections, we will analyse the splat contours for the available samples, it set the fourth one because of the splats are not completed.

5.2.1 Splat contour analysis: Sample 1

First, we analyse the doughnut splats. A total of 12 splats have been analysed, obtaining the equivalent diameter as mentioned in the paragraph 4.4.

Since the equivalent diameters are calculated using pixels as unit (d_{fp}), we need to transform the values to μm. In order to obtain this conversion, it is necessary to find out the ratio between the width measured in pixels (L_p) and μm (L). In order to know the last width, we use scale bar at the bottom of the image. Thus, equivalent diameters in μm (d_f) is obtained by

$$d_f = \frac{L}{L_p} \cdot d_{fp}$$

In order to get a better insight of the diametrical relationship, the splat list has been ordered from thicker to thinner, Figure 5.8. The thickness ranges from 3.52 μm to 7.97 μm (mean of 5.63 μm).

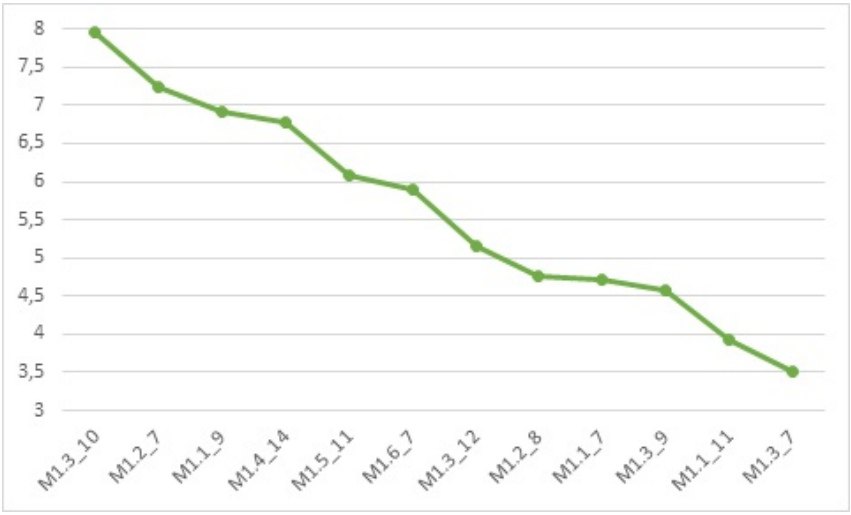

Figure 5.8: Doughnut splat thickness on the sample 1

Figure 5.9 shows the outer and inner diameters of the splats. If we remove the fifth, seventh and the two latter points, correspondent to splats with uncommon outer and inner diameters' ratio, Figures 5.10 to 5.13, a smoother curve is available, Figure 5.14. Figures 5.10 to 5.12, correspondent to the seventh and the two latter points, represent splats with a small section thickness, while Figure 5.13, correspondent to the fifth point, represents a splat with an exceptional thickness.

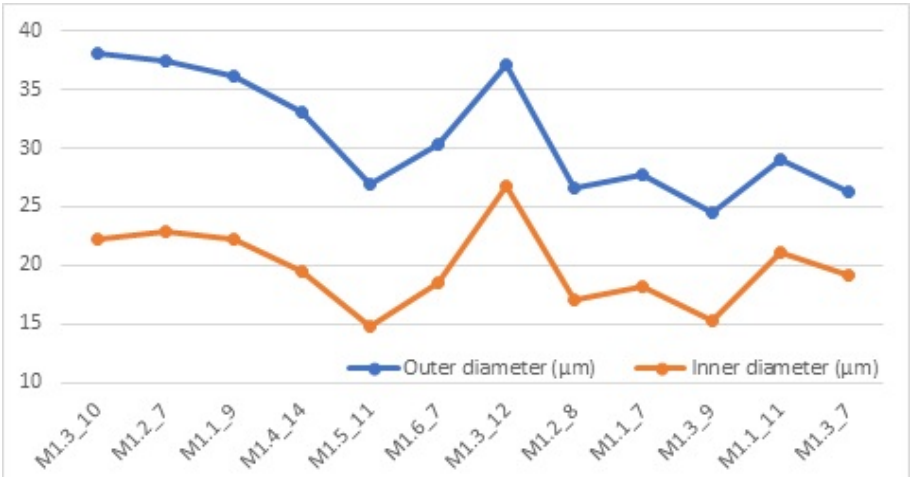

Figure 5.9: Outer and inner diameters of doughnut splats on the sample 1

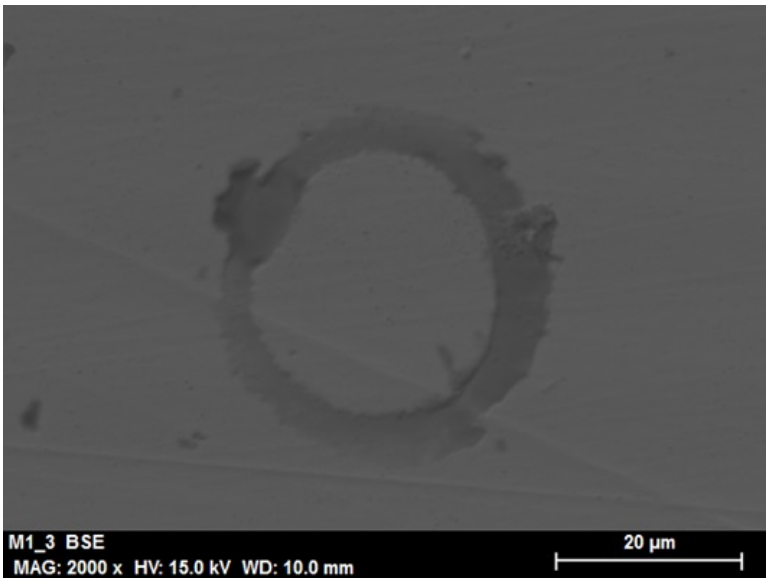

Figure 5.10: Doughnut splat with abnormal geometry on the sample 1, cluster 3

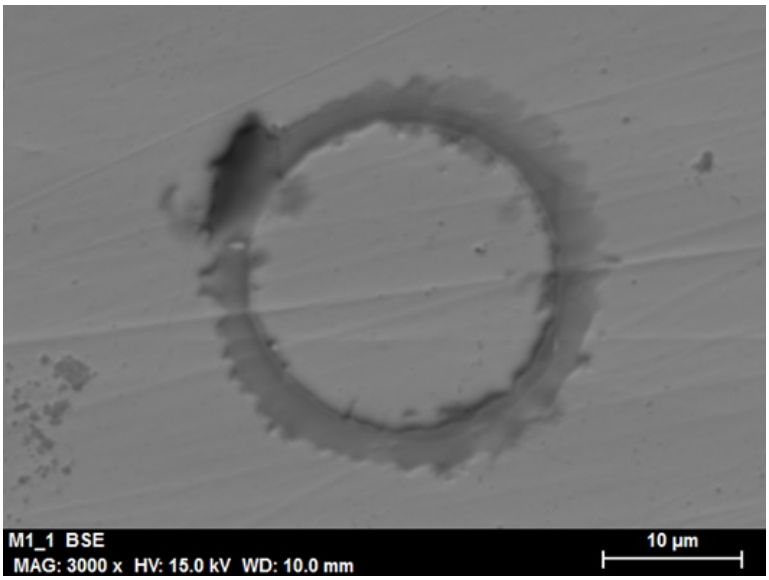

Figure 5.11: Doughnut splat with abnormal geometry on the sample 1, cluster 1

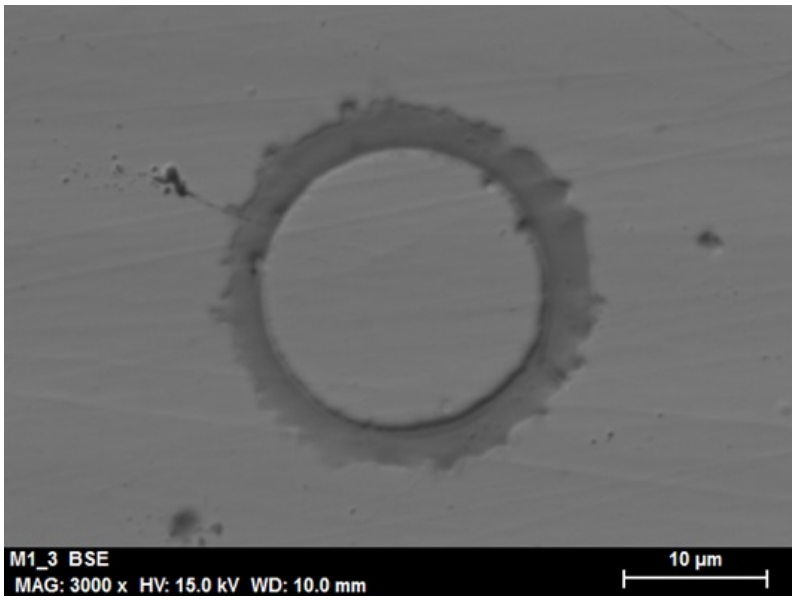

Figure 5.12: Doughnut splat with abnormal geometry on the sample 1, cluster 3

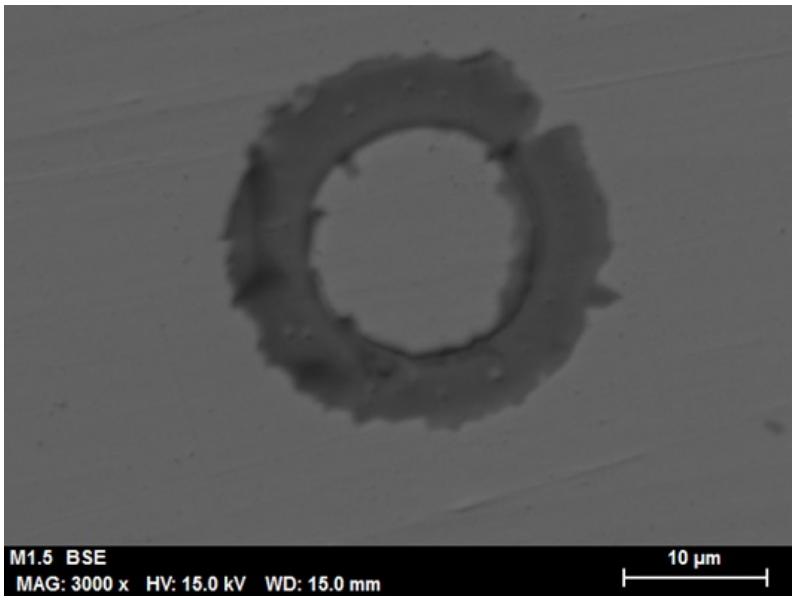

Figure 5.13: Doughnut splat with abnormal geometry on the sample 1, cluster 5

From Figure 5.14, we can see that the larger the outer diameter is, the bigger the thickness is. The large diameter has relation to a big expansion, in turn, related to a high impact energy; therefore, the drops have a high velocity before the impact. For the same diameter, the thickness depends on the drop diameter.

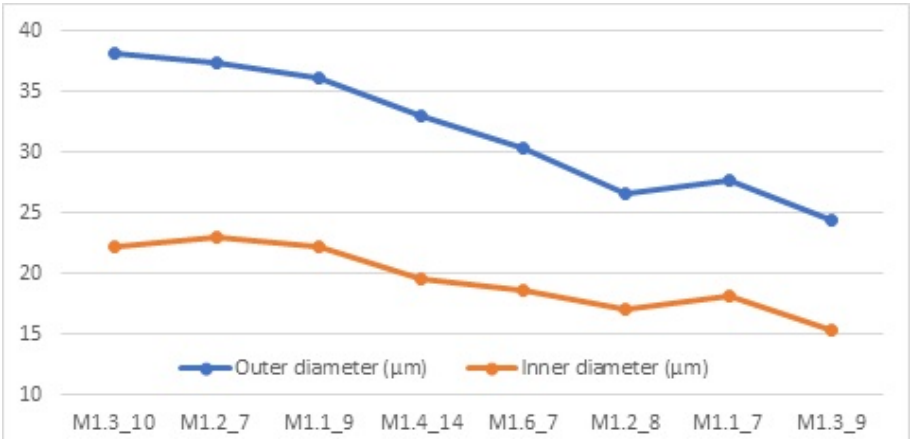

Figure 5.14: Refined outer and inner diameters of doughnut splats on the sample 1

The pancake splats diameters, easier to analyse, are depicted in Figure 5.15. From this figure, the first splat shows a diameter very different to the next lower one. Figure 5.16 shows this splat with an abnormal geometry, which is removed from the list.

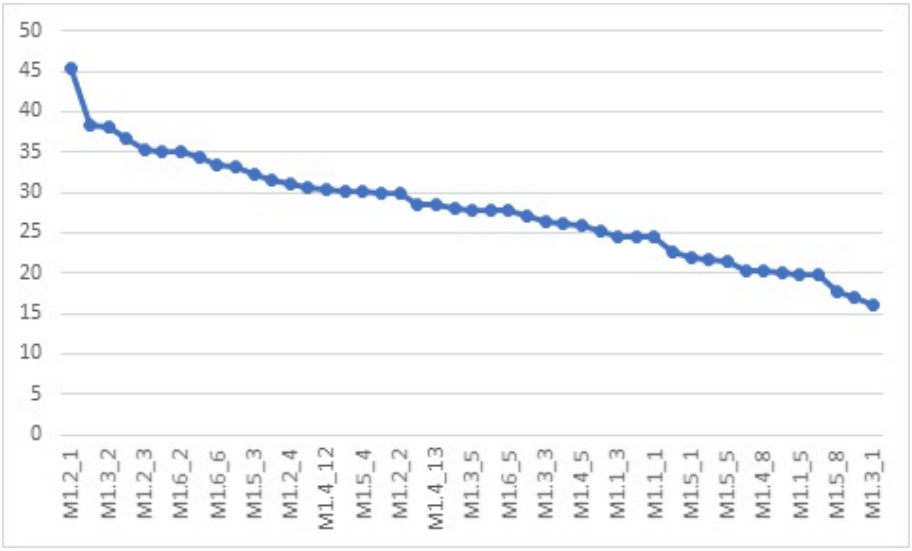

Figure 5.15: Pancake splat diameters on the sample 1

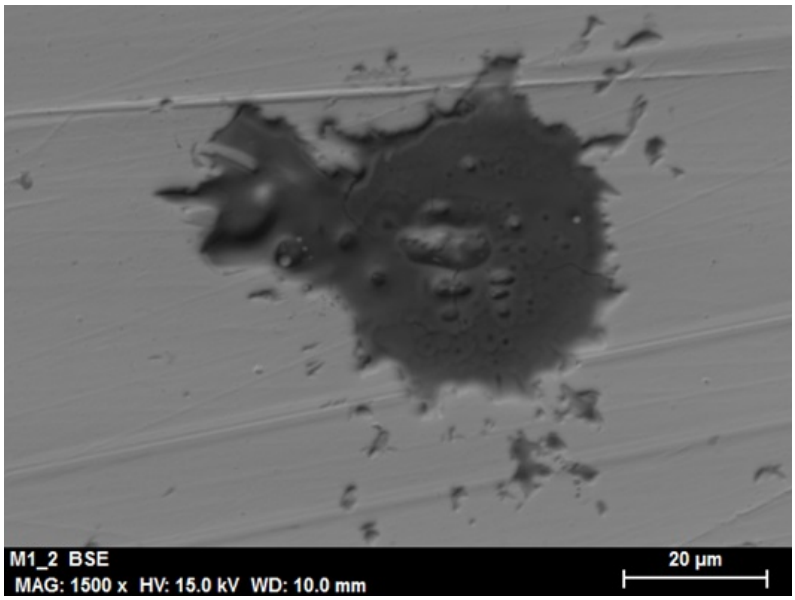

Figure 5.16: Pancake splat with abnormal geometry on the sample 1, cluster 2

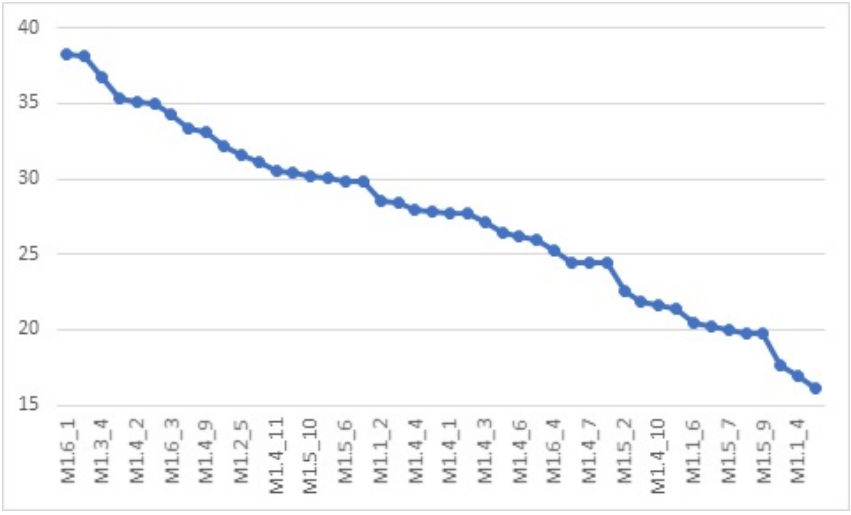

Figure 5.17: Refined pancake splat diameters on the sample 1

The pancake splats diameters, easier to analyse, are depicted in Figure 5.17. The diameters are ranged from 16.09 μm to 38.32 μm (mean of 27.41 μm). For the doughnut splats, the outer diameters are lowers, ranged from 24.42 μm to 38.10 μm (mean of 31.71 μm). It is evident that the pancake splats have a higher kinetic energy than the doughnut splats.

5.2.2 Splat contour analysis: Sample 2

This sample has only pancake splats. From Figure 5.18, the last splat shows a diameter very different to the next lower one. Figure 5.19 shows this splat with an abnormal geometry, which is removed from the list.

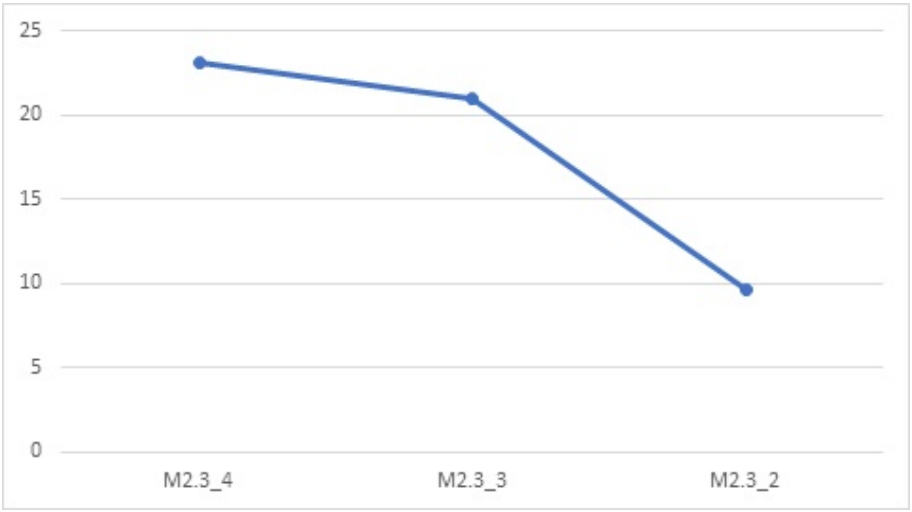

Figure 5.18: Pancake splat diameters on the sample 2

Figure 5.19: Pancake splat with an abnormal geometry on the sample 2, cluster 3

Thus, the splat diameters are ranged from 20.96 μm to 23.13 μm (mean of 22.05 μm). These splats are smaller than those on the sample 1.

5.2.3 Splat contour analysis: Sample 3

First, we analyse the doughnut splats. A total of four splats have been analysed, obtaining the equivalent diameters. In order to find out the diametrical relationship the splat list has been ordered from thicker to thinner, Figure 5.20. The thickness ranges from 5.24 μm to 6.47 μm (mean of 5.83 μm).

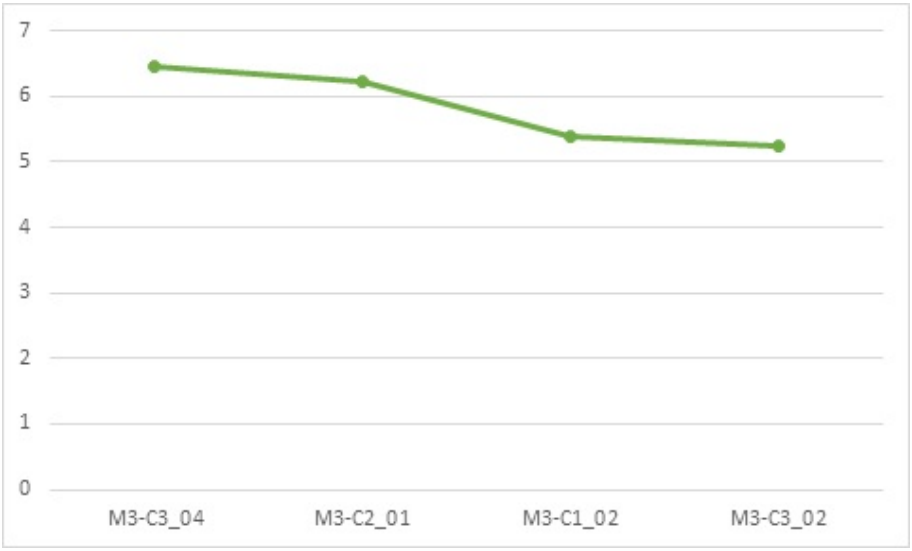

Figure 5.20: Doughnut splat thickness on the sample 3

Figure 5.21 shows the outer and inner diameters of the splats.

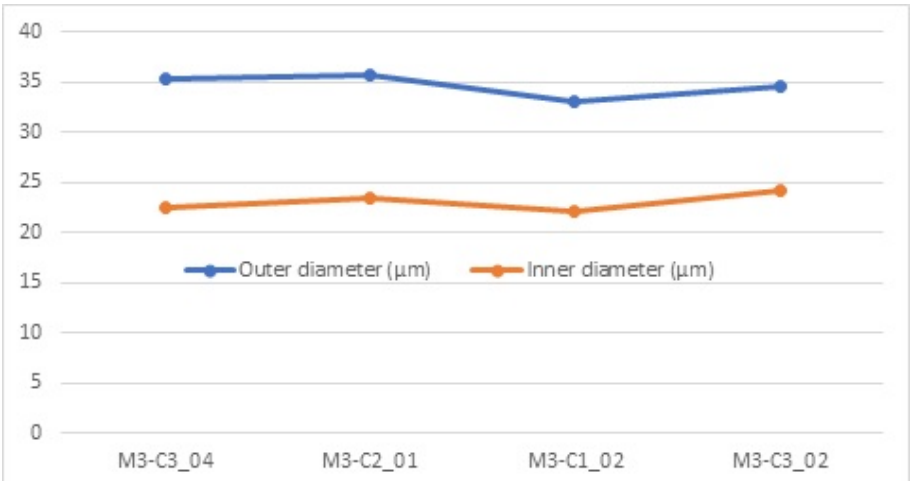

Figure 5.21: Outer and inner diameters of doughnut splats on the sample 3

From Figure 5.21, the diameters are very close each other. The pancake splats, easier to analyse, are depicted in Figure 5.22.

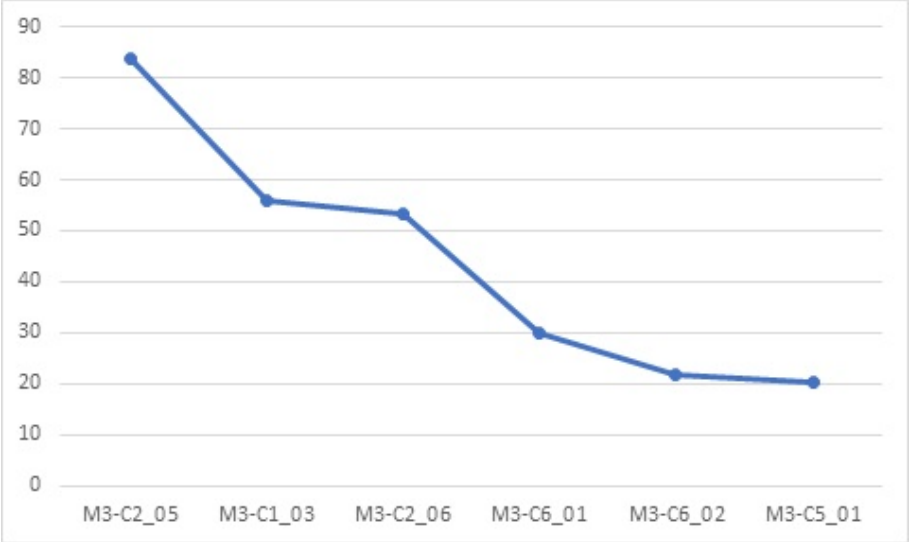

Figure 5.22: Pancake splat diameters on the sample 3

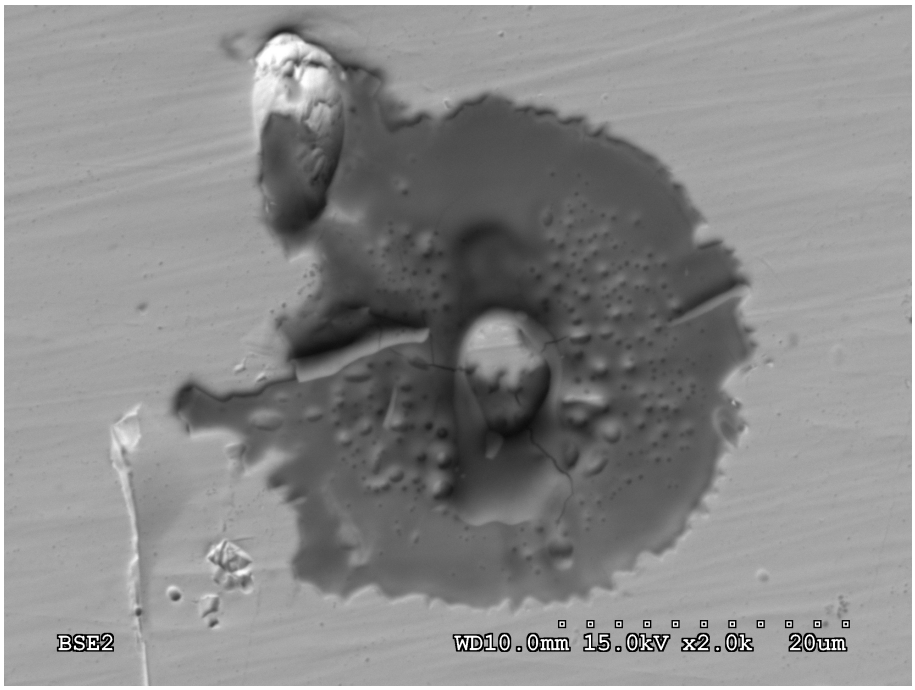

Figure 5.23: Pancake splat with an abnormal geometry on the sample 3, cluster 3

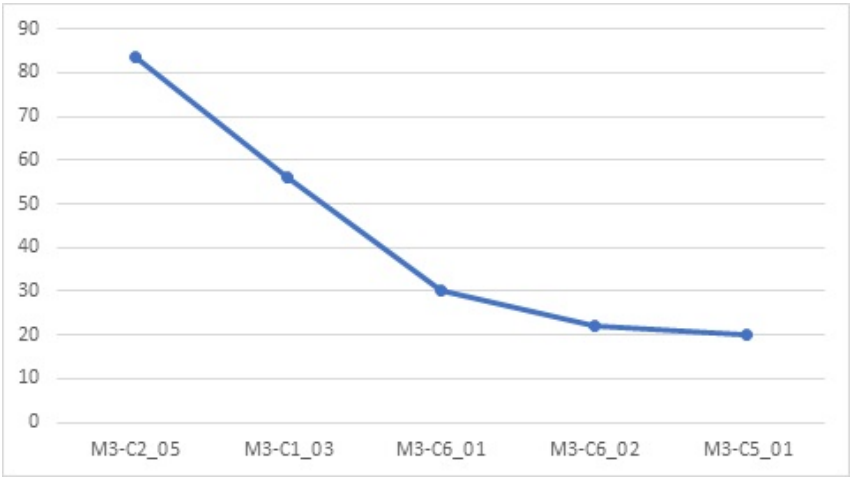

Figure 5.24: Refined pancake splat diameters on the sample 3

We reviewed the remainder splats looking for more unsuitable splats, as it appears in Figure 5.25. Thus, Figure 5.26 shows the new refined pancake splat diameters.

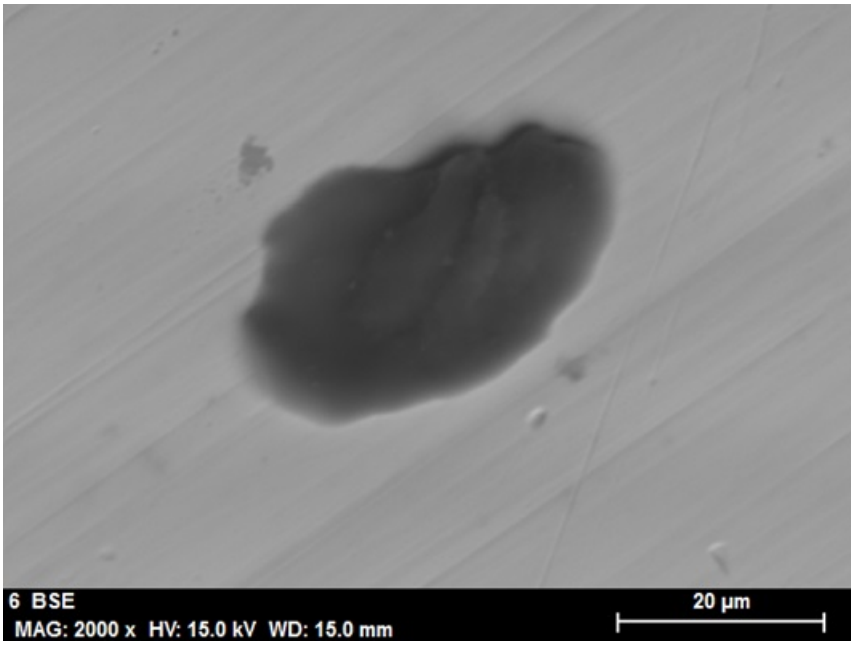

Figure 5.25: Pancake splat with an abnormal geometry on the sample 3, cluster 3

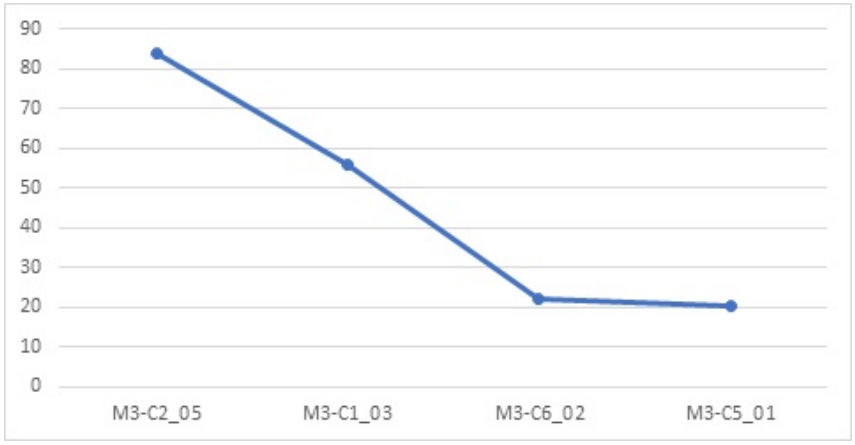

Figure 5.26: New refined pancake splat diameters on the sample 3

The pancake splats, easier to analyse, are depicted in Figure 5.26. The diameters are ranged from 20.26 μm to 83.79 μm (mean of 45.46 μm). For the doughnut splats, the outer diameters are lowers, ranged from 32.98 μm to 35.76 μm (mean of 34.67 μm). It is evident that the pancake splats have a higher kinetic energy than the doughnut splats.

5.2.4 Splat contour analysis: Sample 4

Only a splat with doughnut shape has been found in the sample 4, its outer equivalent diameter measures 43.17 μm, the inner one is 27.85 μm, thus its thickness takes a value of 7.66 μm.

Regarding pancake splats, we have observed two splats. Their diameters are 31.16 μm and 51.75 μm (mean of 41.45 μm).

5.2.5 Splat contour analysis: Sample 5

In this sample, alumina has been shot with different parameters in each face, A and B. The mask was not used; thus, splats appears in the whole faces.

Splat contour analysis: Sample 5, face A

A total of 18 splats have been analysed, obtaining the equivalent diameter. In order to find out the diametrical relationship the splat list has been ordered from thicker to thinner, Figure 5.27. The thickness ranges from 5.14 μm to 13.10 μm (mean of 8.46 μm).

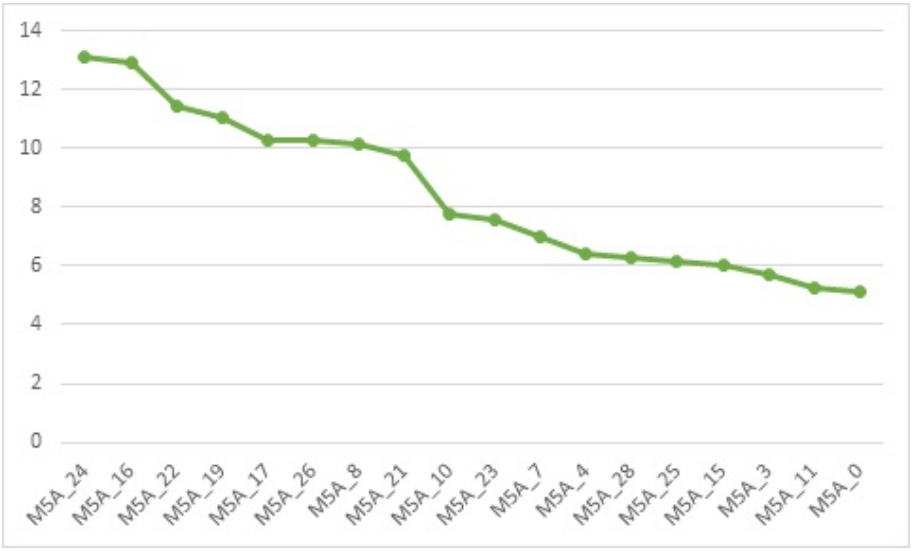

Figure 5.27: Doughnut splat thickness on the sample 5, face A

Figure 5.28 shows the outer and inner diameters of the splats. If we remove the 8 splats, a smoother curve is available, Figure 5.37.

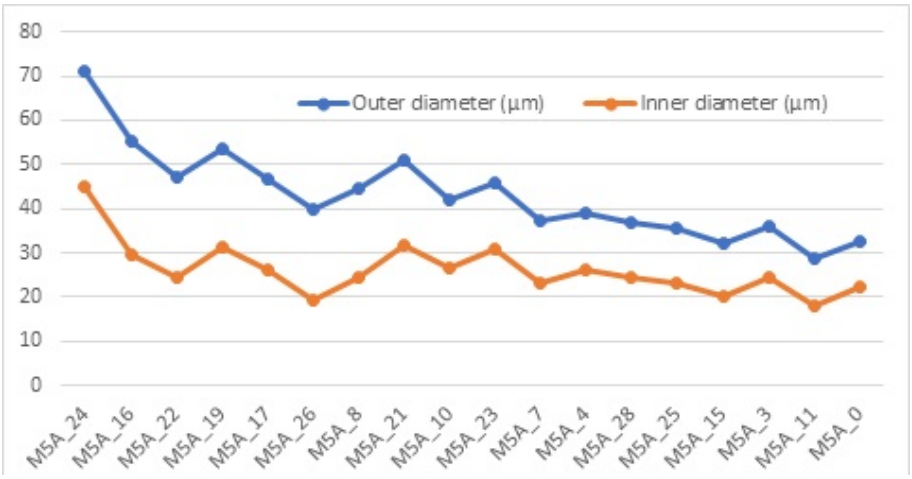

Figure 5.28: Outer and inner diameters of doughnut splats on the sample 5, face A

Figures 5.29 to 5.36 show splats which have impacted with an angle different to 90°.

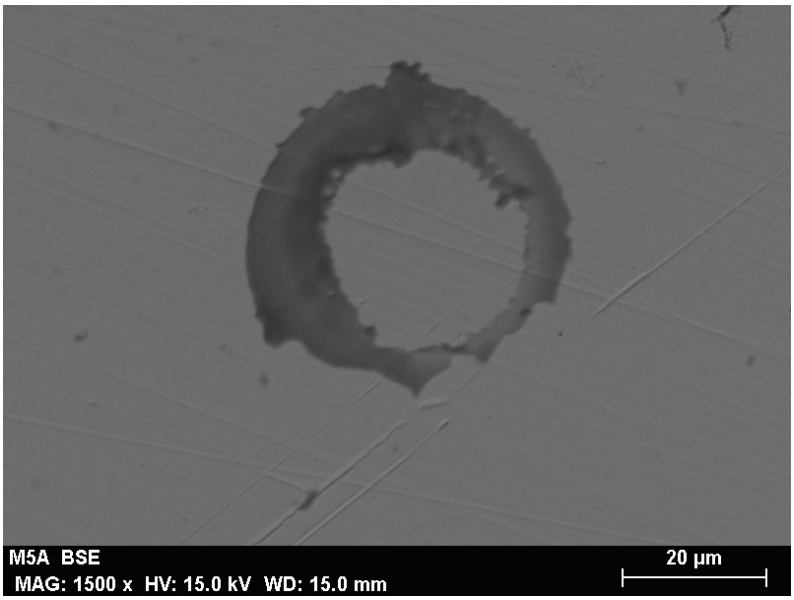

Figure 5.29: Doughnut splat with an abnormal geometry on the sample 5, face A

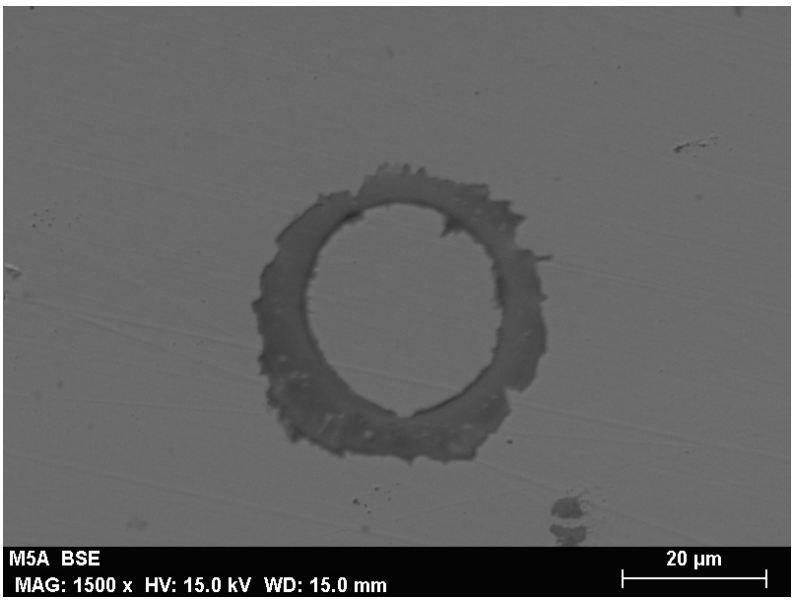

Figure 5.30: Doughnut splat with an abnormal geometry on the sample 5, face A

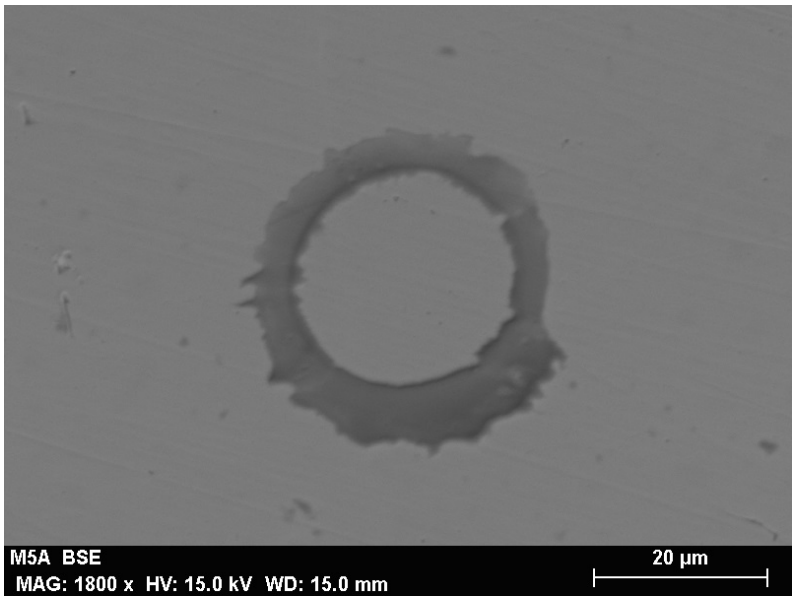

Figure 5.31: Doughnut splat with an abnormal geometry on the sample 5, face A

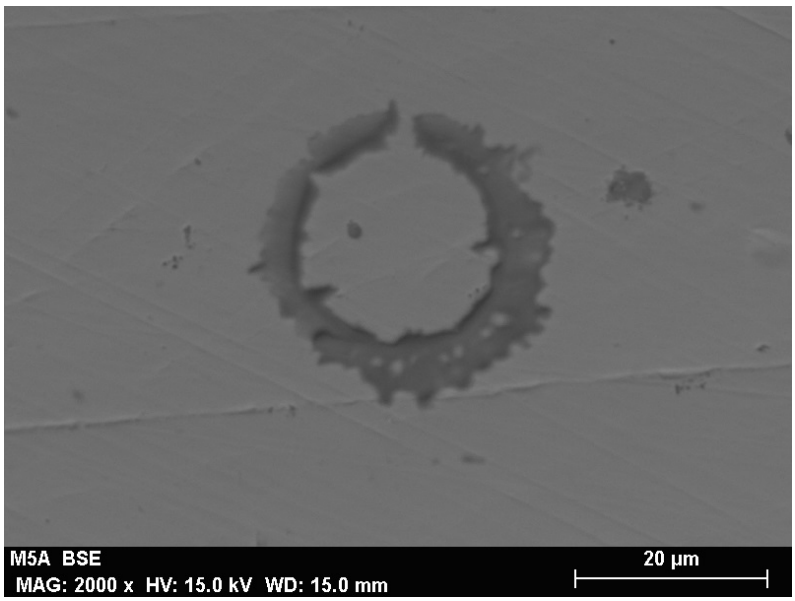

Figure 5.32: Doughnut splat with an abnormal geometry on the sample 5, face A

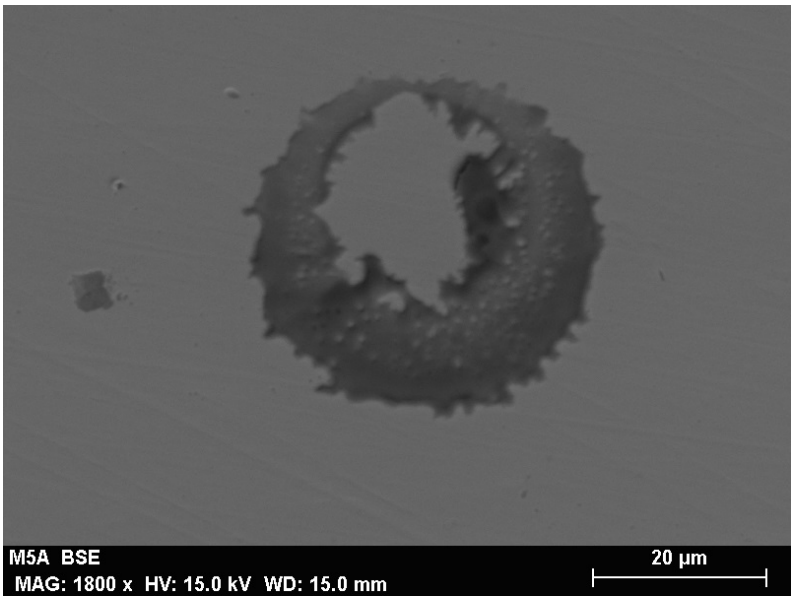

Figure 5.33: Doughnut splat with an abnormal geometry on the sample 5, face A

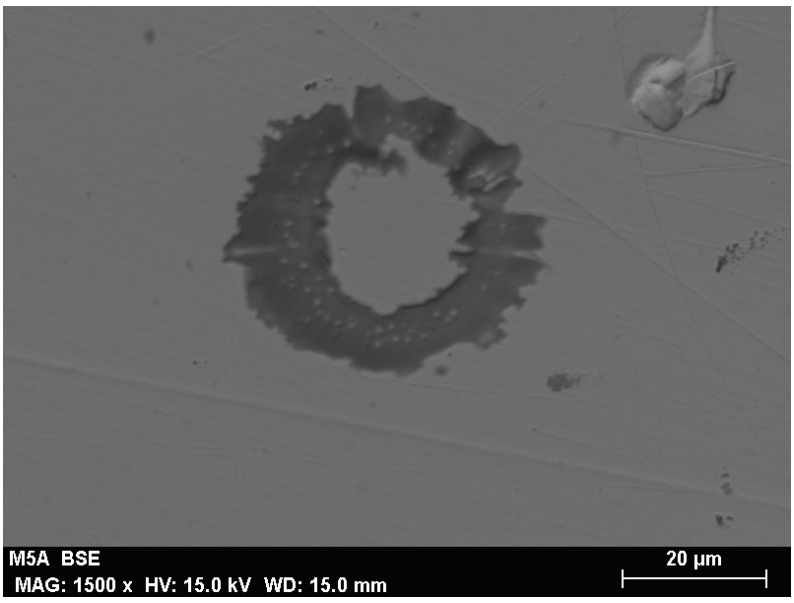

Figure 5.34: Doughnut splat with an abnormal geometry on the sample 5, face A

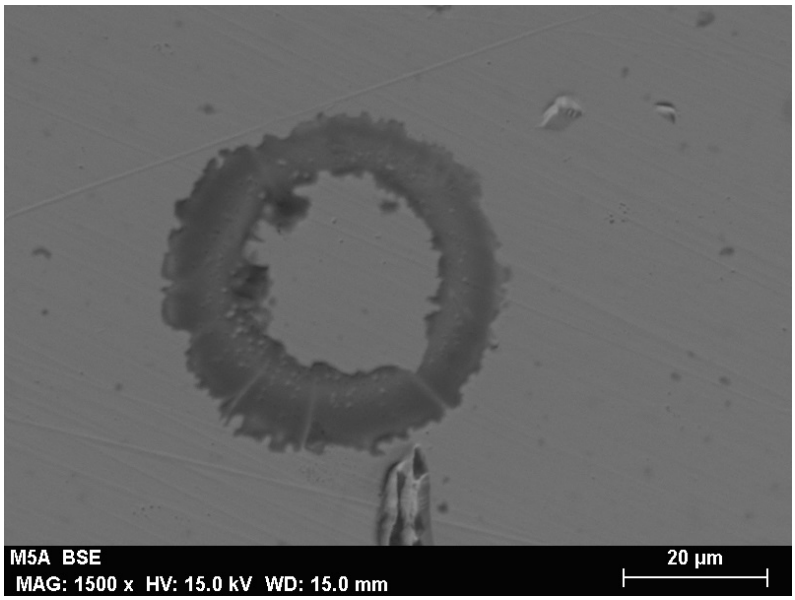

Figure 5.35: Doughnut splat with an abnormal geometry on the sample 5, face A

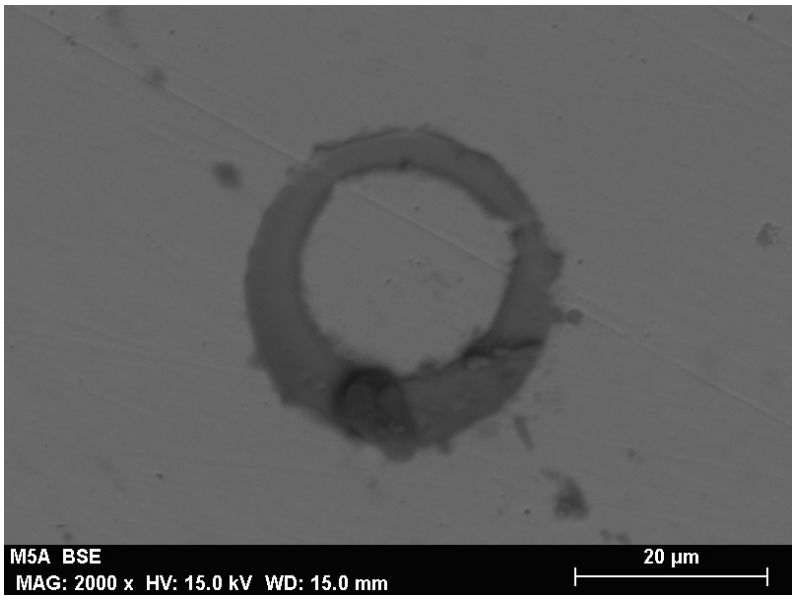

Figure 5.36: Doughnut splat with an abnormal geometry on the sample 5, face A

We reviewed the remainder splats looking for more unsuitable splats. Figure 5.37 shows the new refined pancake splat diameters; the removed splats appear in Figure 5.38 to Figure 5.41.

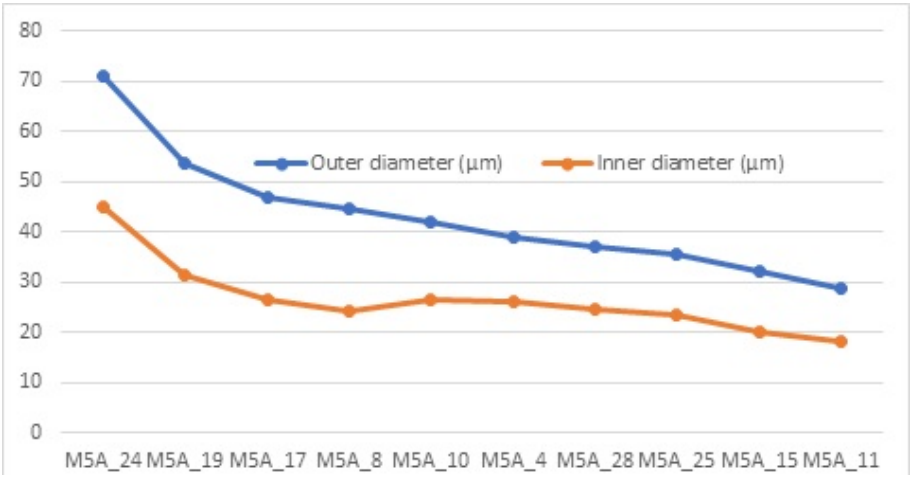

Figure 5.37: Refined outer and inner diameters of doughnut splats on the sample 5, face A

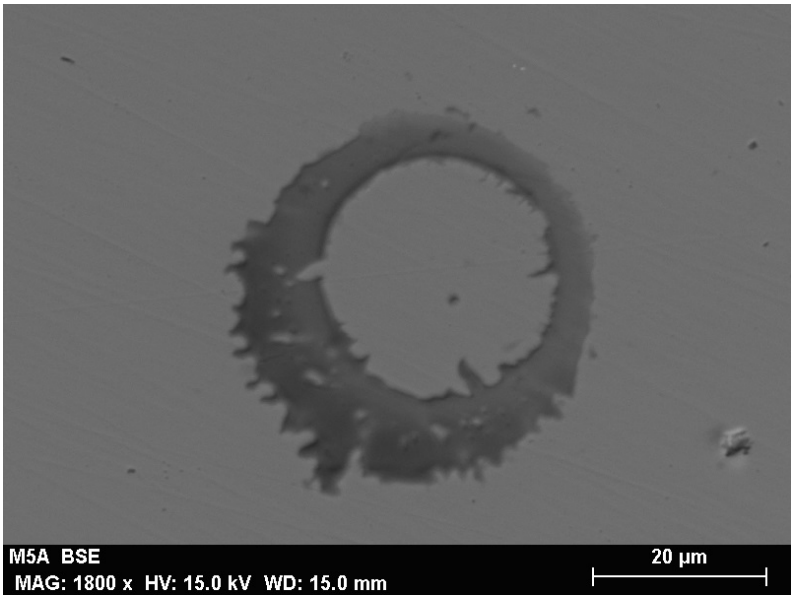

Figure 5.38: Doughnut splat with an abnormal geometry on the sample 5, face A

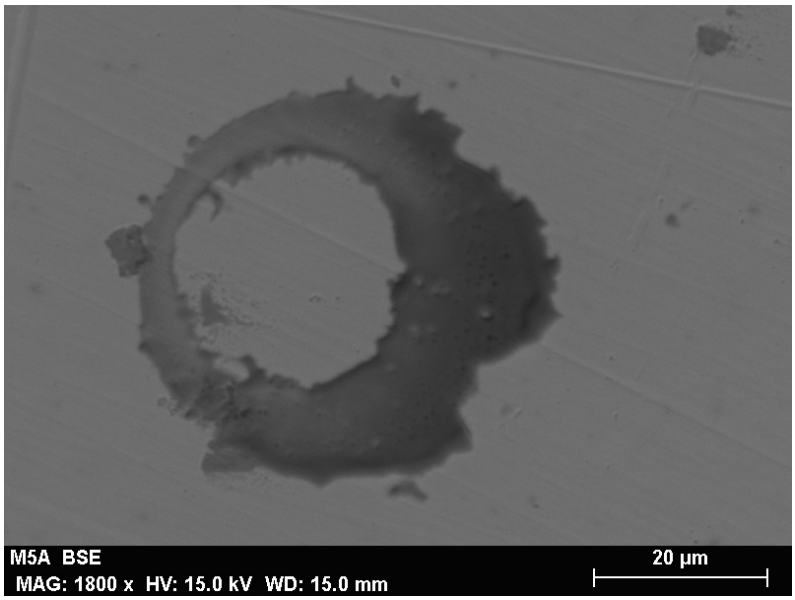

Figure 5.39: Doughnut splat with an abnormal geometry on the sample 5, face A

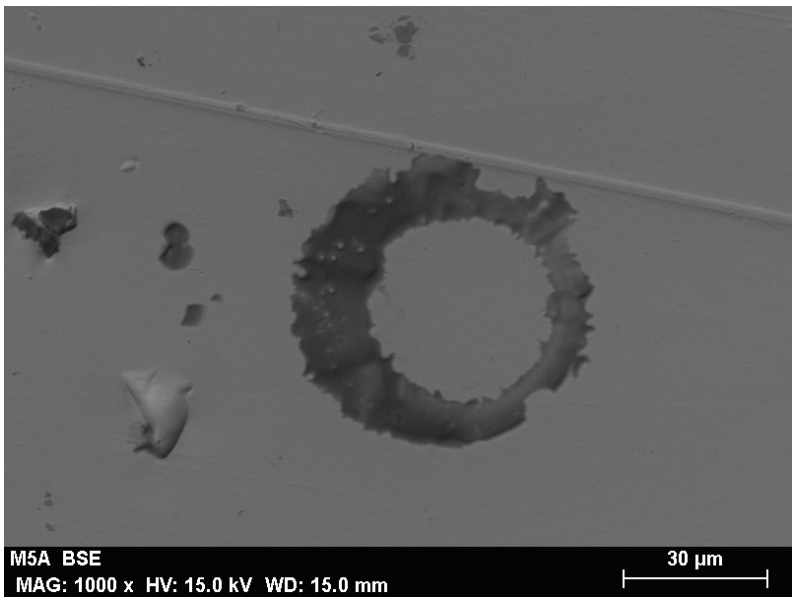

Figure 5.40: Doughnut splat with an abnormal geometry on the sample 5, face A

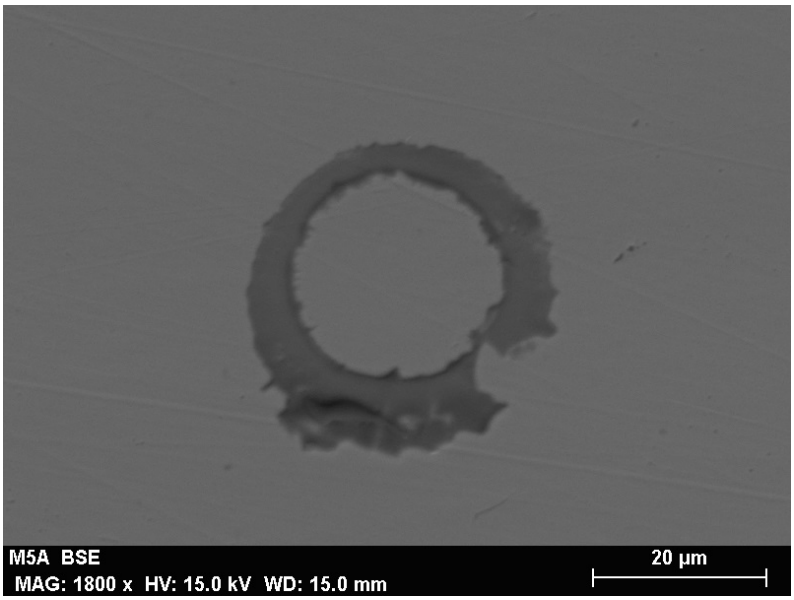

Figure 5.41: Doughnut splat with an abnormal geometry on the sample 5, face A

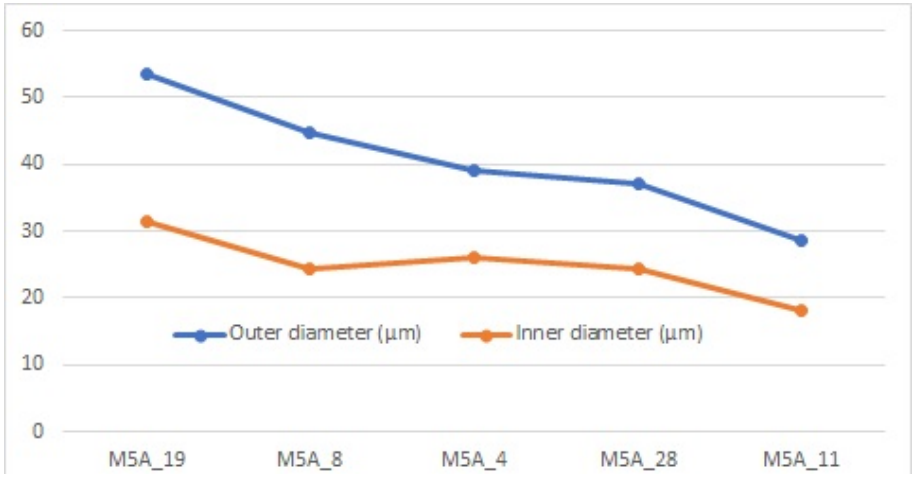

Figure 5.42: New refined outer and inner diameters of doughnut splats on the sample 5, face A

The pancake splats, easier to analyse, are depicted in Figure 5.43. The diameters are ranged from 30.15 μm to 56.95 μm (mean of 43.88 μm). For the doughnut splats, the outer diameters are lowers, ranged from 28.55 μm to 53.55 μm (mean of 40.55 μm). It is evident that the pancake splats have a higher kinetic energy than the doughnut splats.

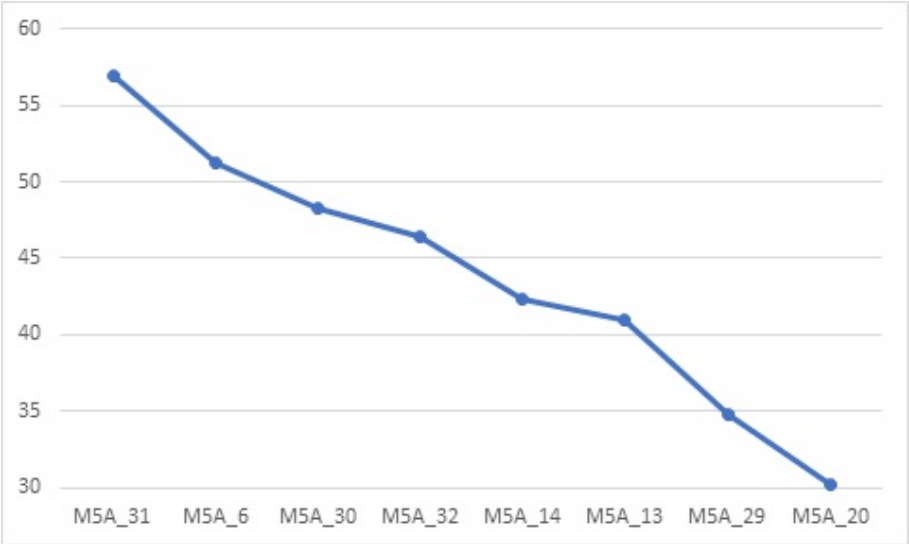

Figure 5.43: Pancake splat diameters on the sample 5, face A

Splat contour analysis: Sample 5, face B

A total of 24 splats have been analysed, obtaining the equivalent diameter. In order to find out the diametrical relationship the splat list has been ordered from thicker to thinner, Figure 5.44. The thickness ranges from 5.14 μm to 13.10 μm (mean 8.46 μm).

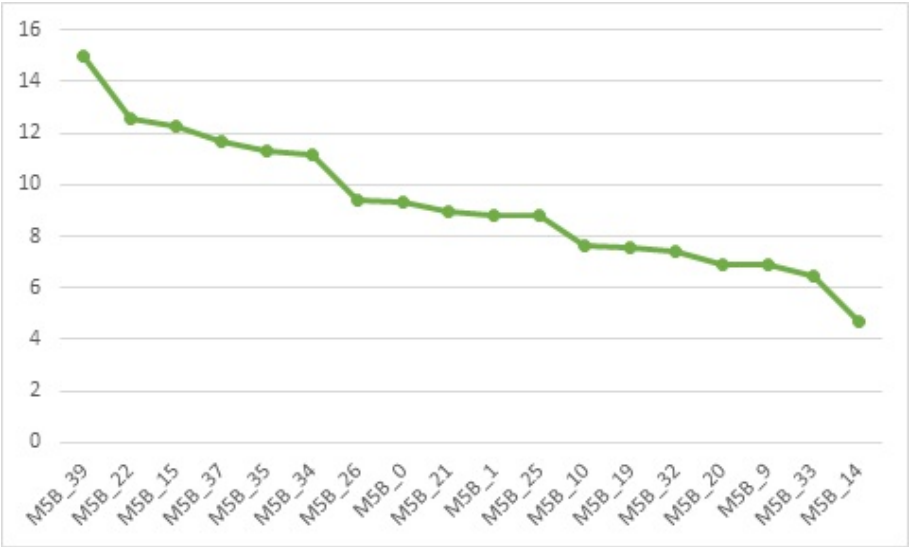

Figure 5.44: Doughnut splat thickness on the sample 5, face B

Figure 5.45 shows the outer and inner diameters of the splats. If we remove the 4 splats, a smoother curve is available, Figure 5.50.

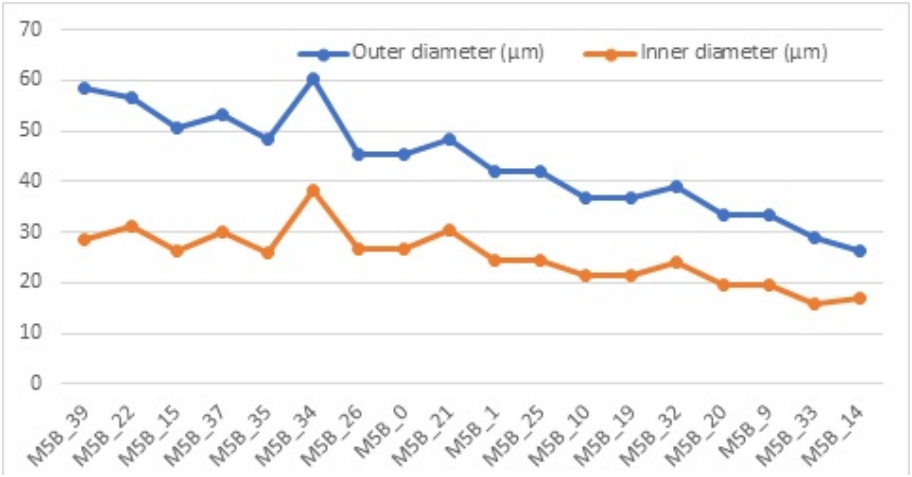

Figure 5.45: Outer and inner diameters of doughnut splats on the sample 5, face B

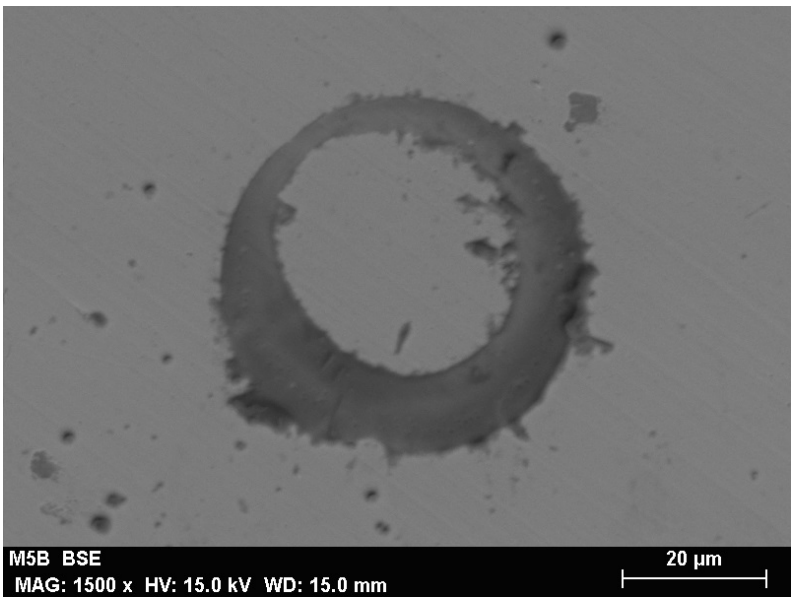

Figure 5.46: Doughnut splat with an abnormal geometry on the sample 5, face B

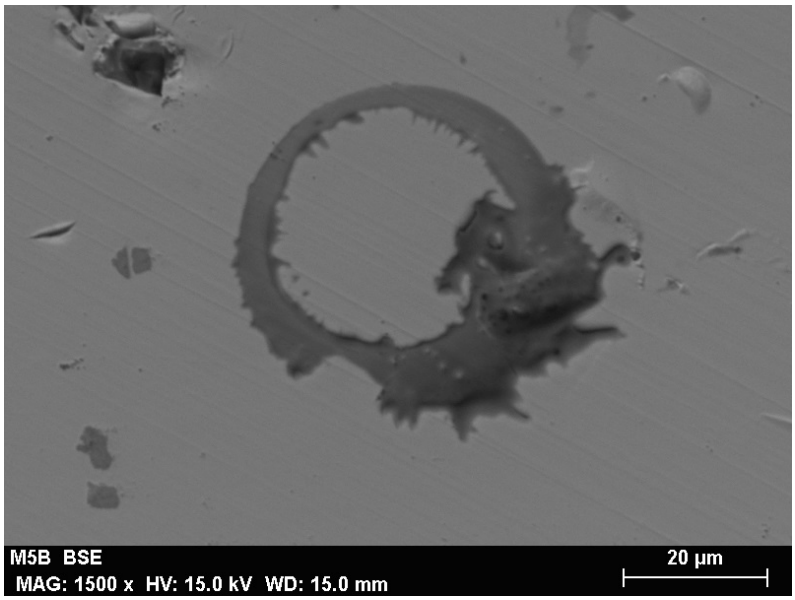

Figure 5.47: Doughnut splat with an abnormal geometry on the sample 5, face B

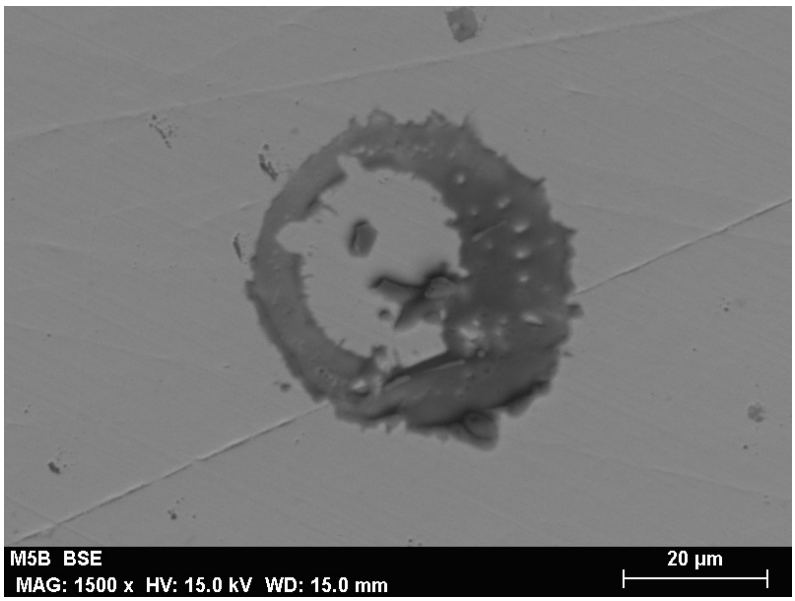

Figure 5.48: Doughnut splat with an abnormal geometry on the sample 5, face B

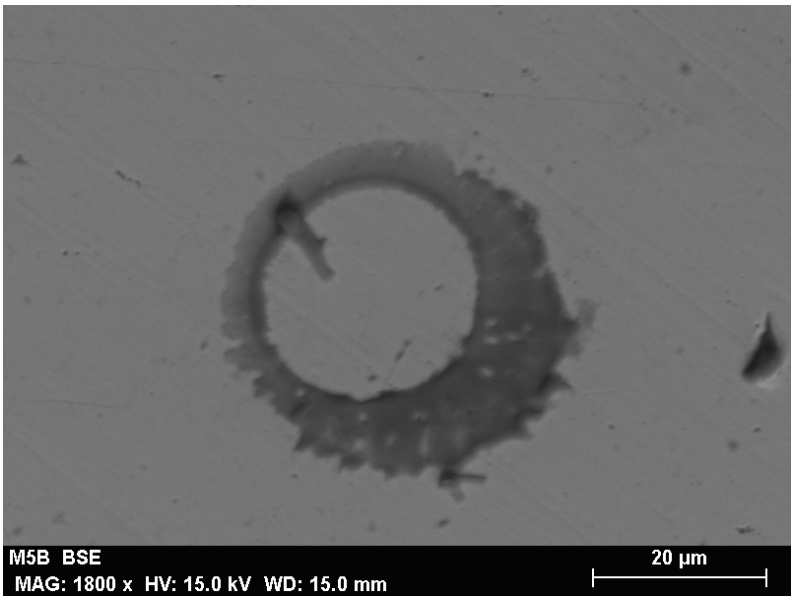

Figure 5.49: Doughnut splat with an abnormal geometry on the sample 5, face B

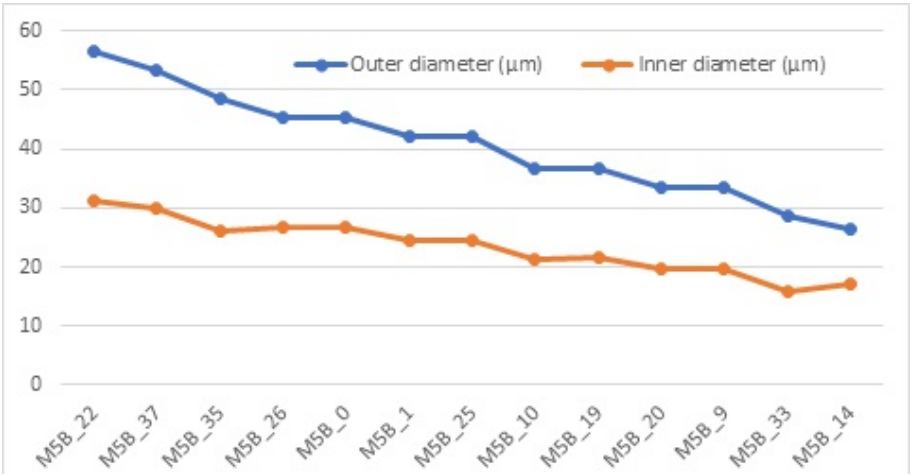

Figure 5.50: Refined outer and inner diameters of doughnut splats

We reviewed the remainder splats looking for more unsuitable splats. Figure 5.54 shows the new refined pancake splat diameters; the removed splats appear in Figure 5.51 to Figure 5.53.

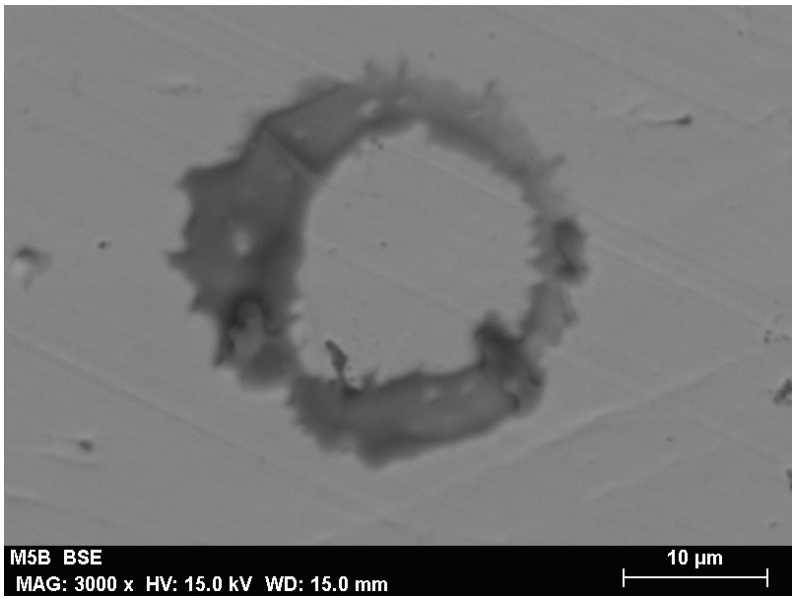

Figure 5.51: Doughnut splat with an abnormal geometry on the sample 5, face B

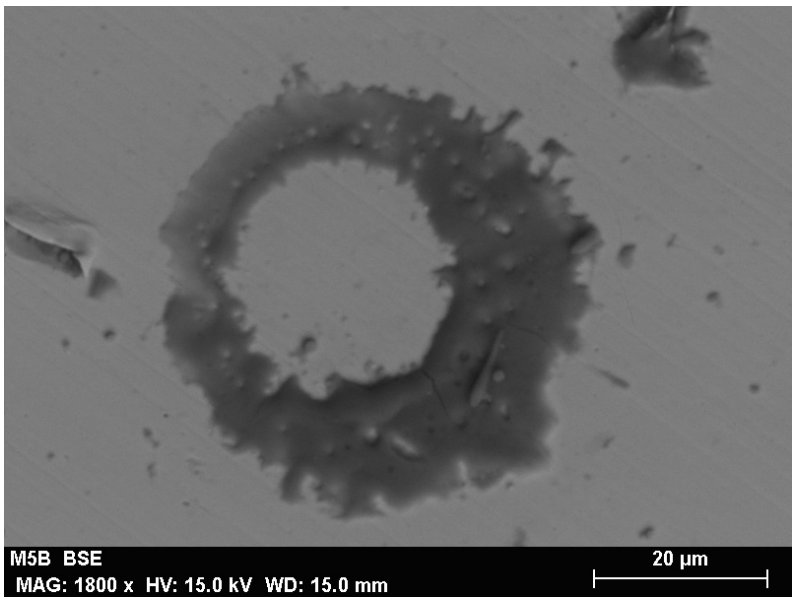

Figure 5.52: Doughnut splat with an abnormal geometry on the sample 5, face B

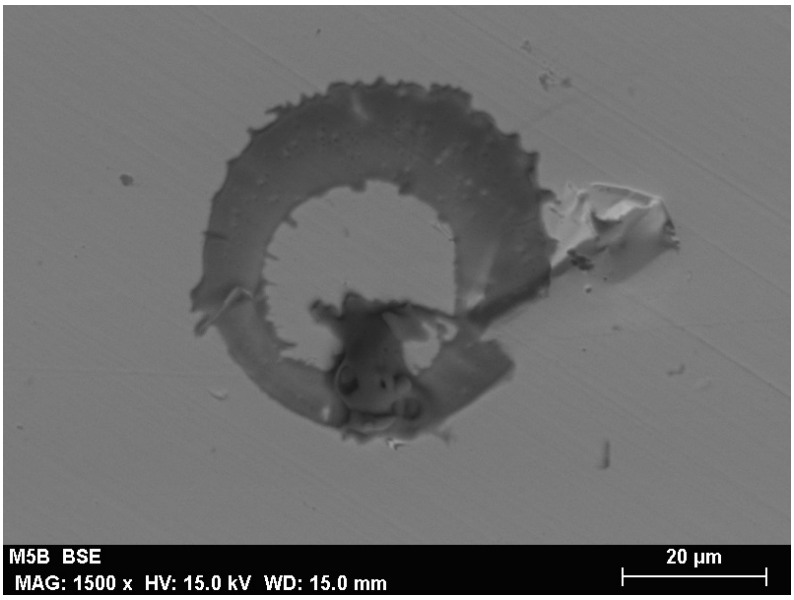

Figure 5.53: Doughnut splat with an abnormal geometry on the sample 5, face B

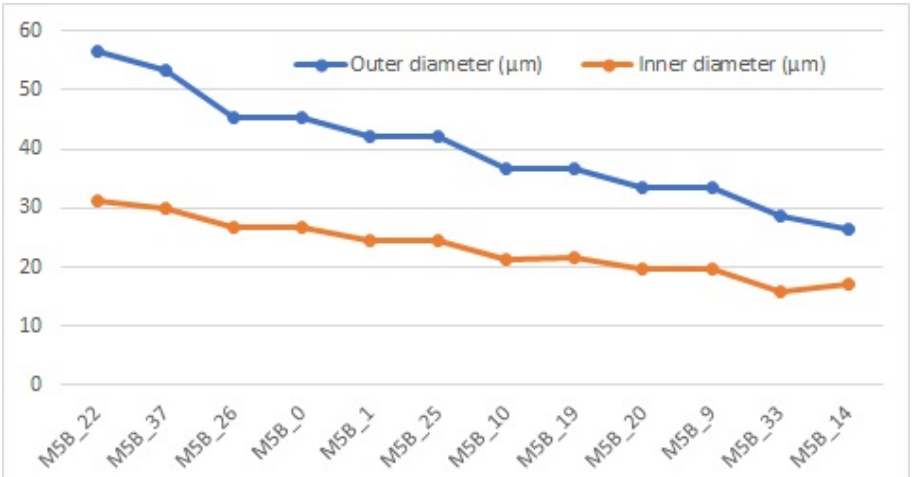

Figure 5.54: New refined outer and inner diameters of doughnut splats on the sample 5, face B

The pancake splats, easier to analyse, are depicted in Figure 5.55.

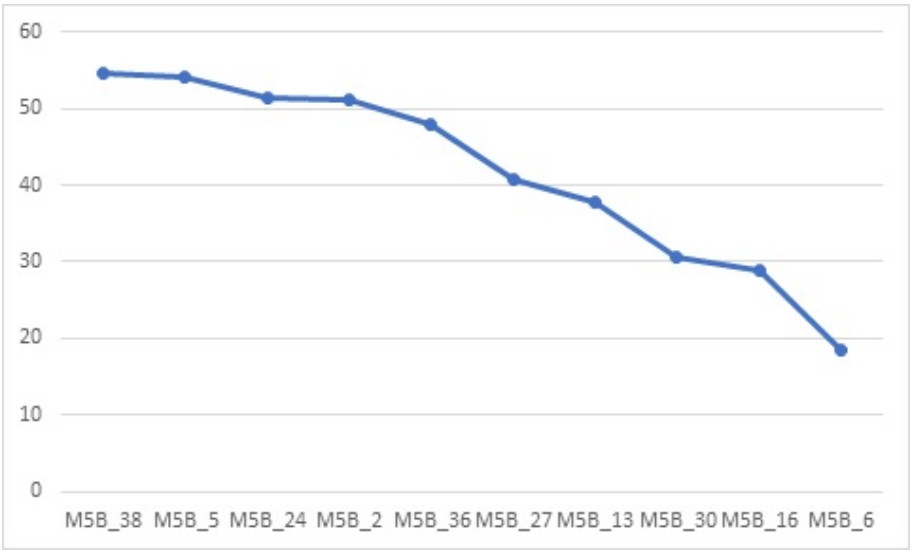

Figure 5.55: Pancake splat diameters on the sample 5, face B

We reviewed the remainder splats looking for more unsuitable splats. Figure 5.58 shows the refined pancake splat diameters; the removed splats appear in Figure 5.56 and Figure 5.57.

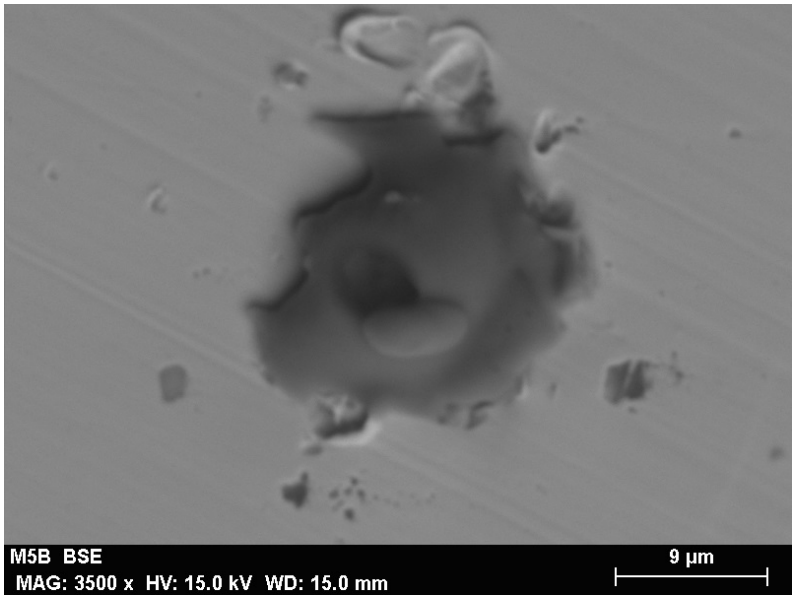

Figure 5.56: Pancake splat with an abnormal geometry on the sample 5, face B

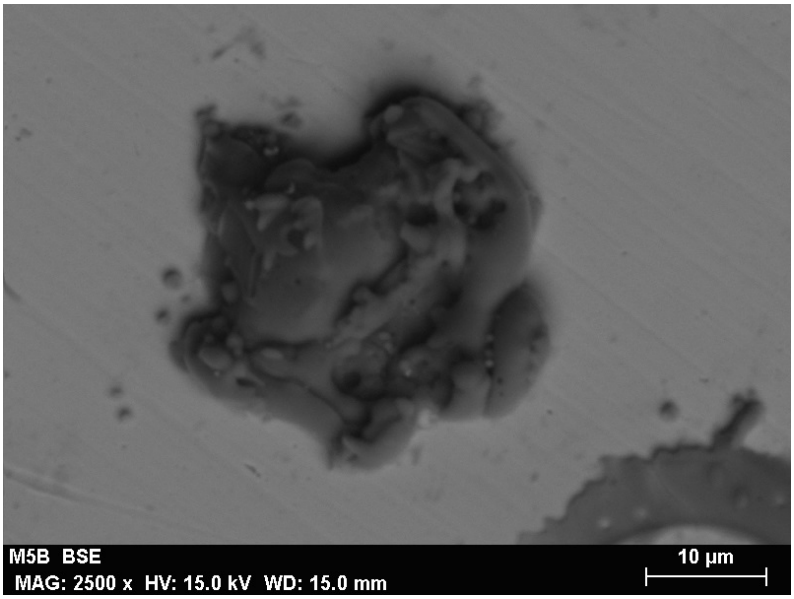

Figure 5.57: Pancake splat with an abnormal geometry on the sample 5, face B

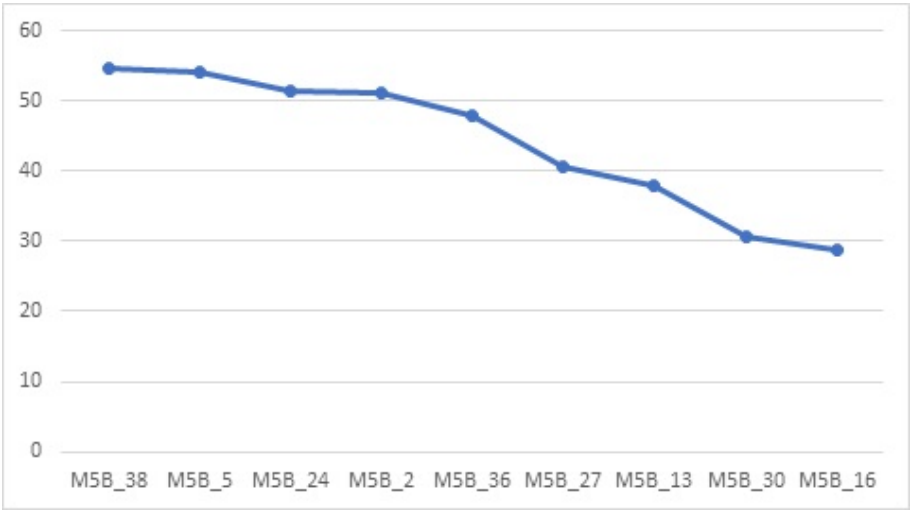

Figure 5.58: Refined pancake splat diameters on the sample 5, face B

The diameters are ranged from 28.76 μm to 54.70 μm (mean of 44.09 μm). For the doughnut splats, the outer diameters are lowers, ranged from 26.37 μm to 56.46 μm (mean of 40.00 μm). It is evident that the pancake splats have a higher kinetic energy than the doughnut splats.

5.3 Visual analysis: cross sections

Figure 5.59 shows the top view of a possible cut splat.

Figure 5.59: Possible cut splat on the sample 4, cluster 3

Figure 5.60 to 5.67 show cross sections of splats, where appear some unmelted particles inside. In some parts of the section, it is possible to see pale surfaces which can be some small scraps.

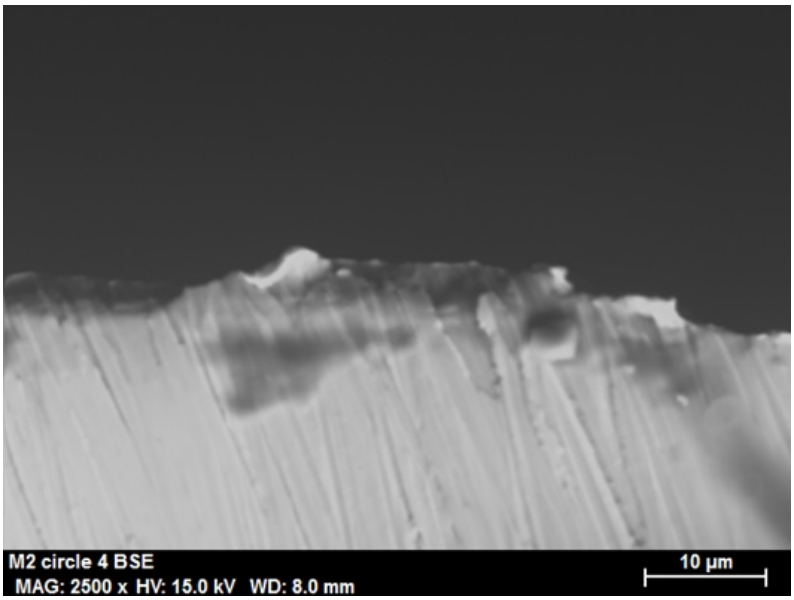

Figure 5.60: Splat cross sections on the sample 2, cluster 4

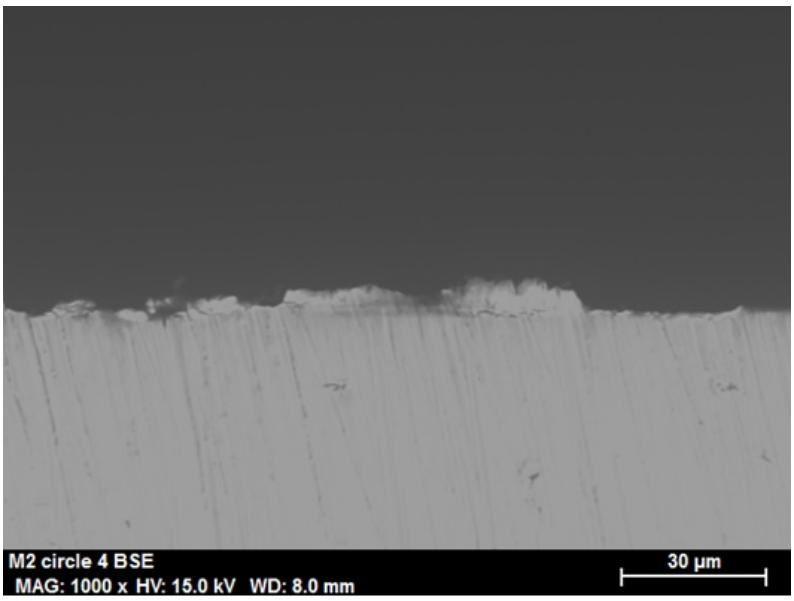

Figure 5.61: Splat cross sections on the sample 2, cluster 4

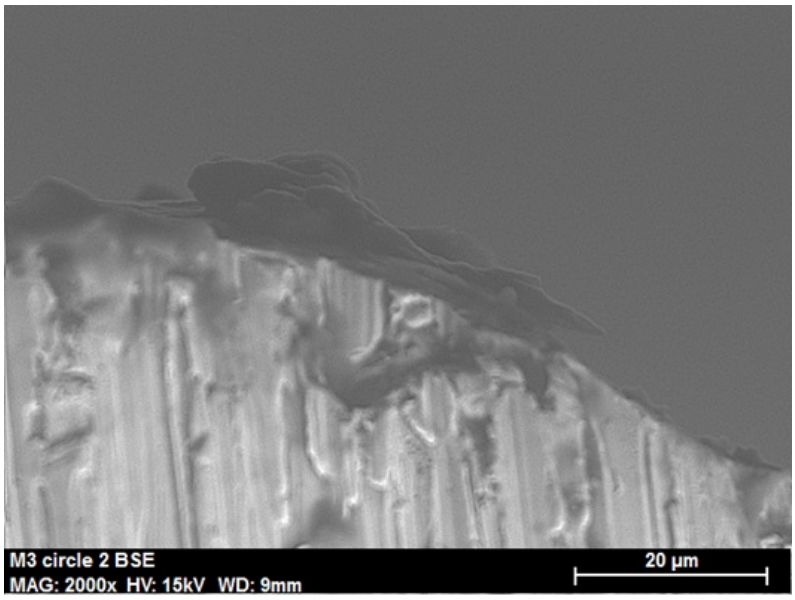

Figure 5.62: Splat cross sections on the sample 3, cluster 2

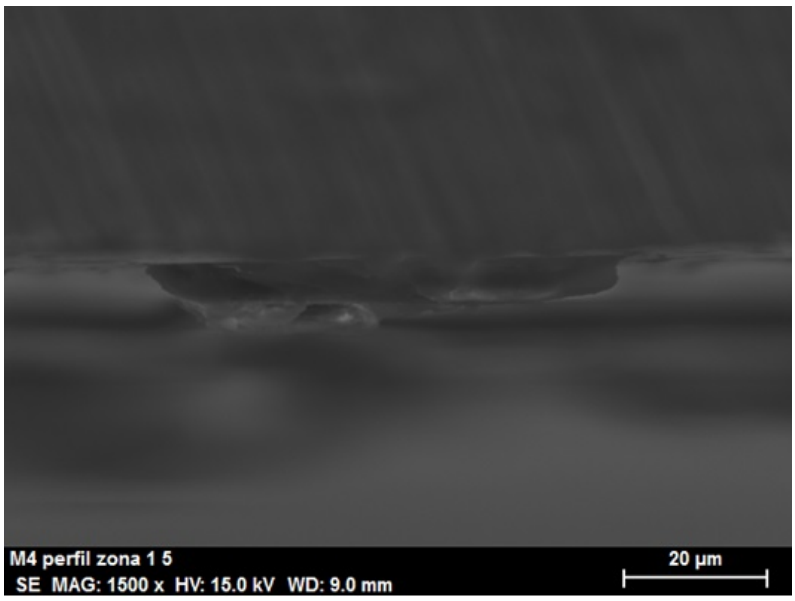

Figure 5.63: Splat cross sections on the sample 4, cluster 1

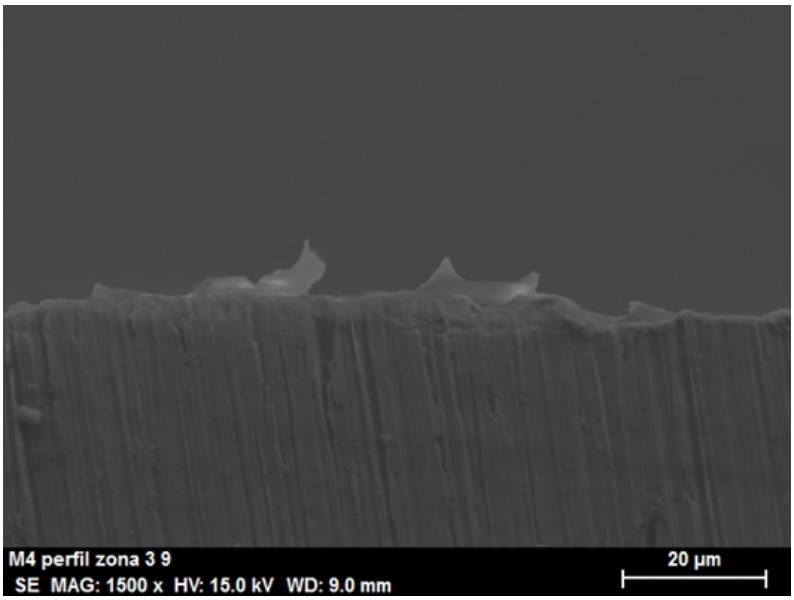

Figure 5.64: Splat cross sections on the sample 4, cluster 3

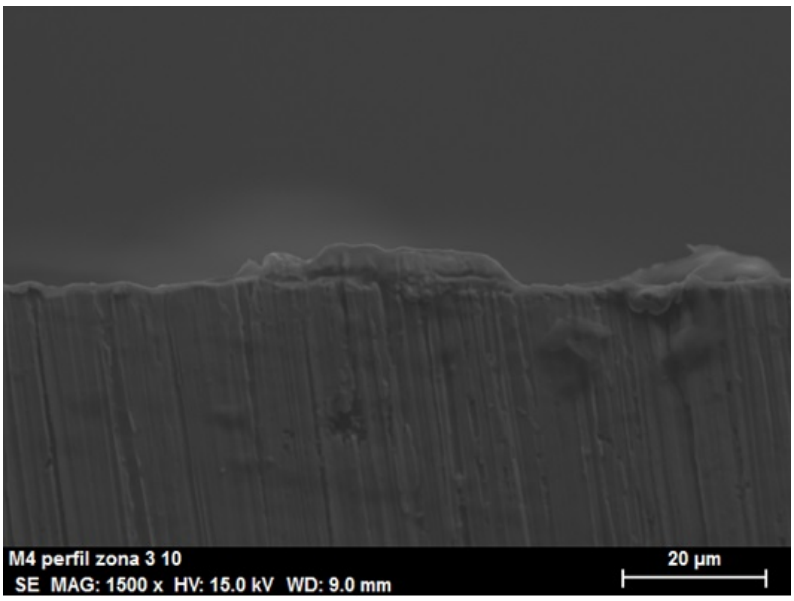

Figure 5.65: Splat cross sections on the sample 4, cluster 3

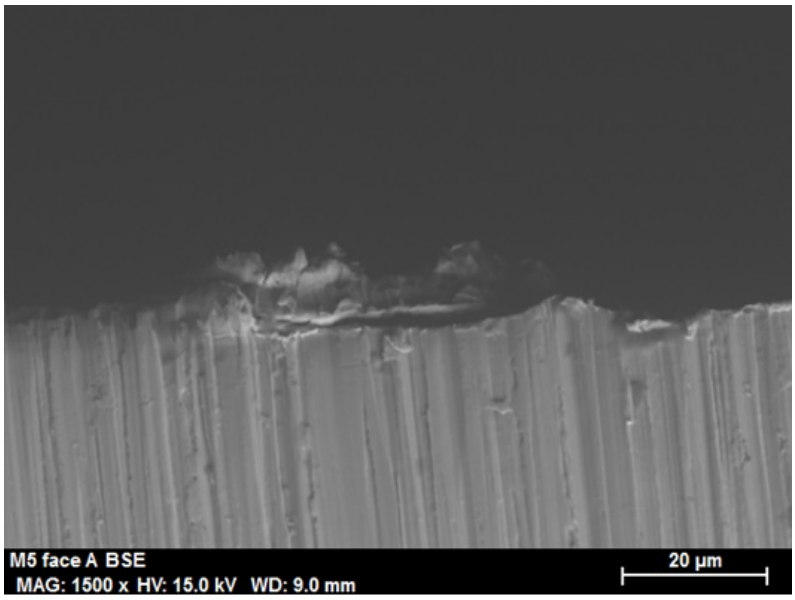

Figure 5.66: Splat cross sections on the sample 5, face A

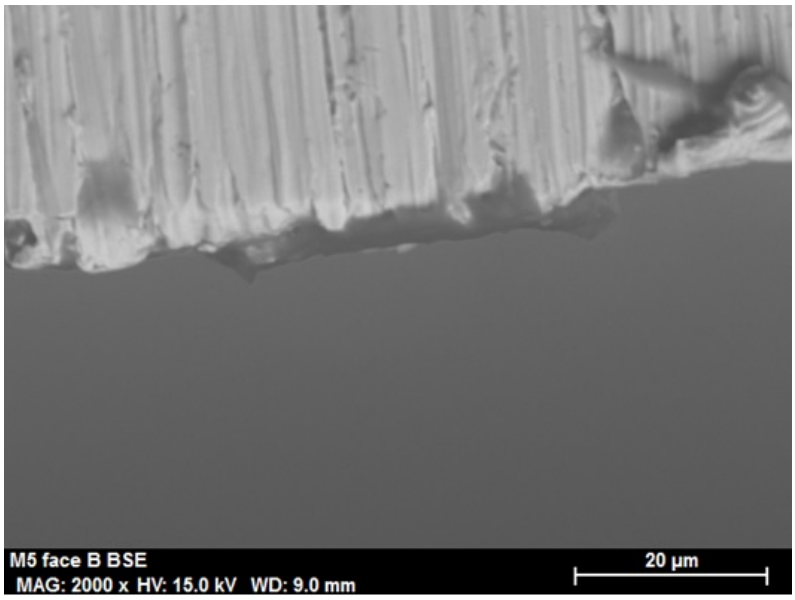

Figure 5.67: Splat cross sections on the sample 5, face B

Some unmelted particles in top view images are marked in Figures 5.68 to 5.74 with red rectangles.

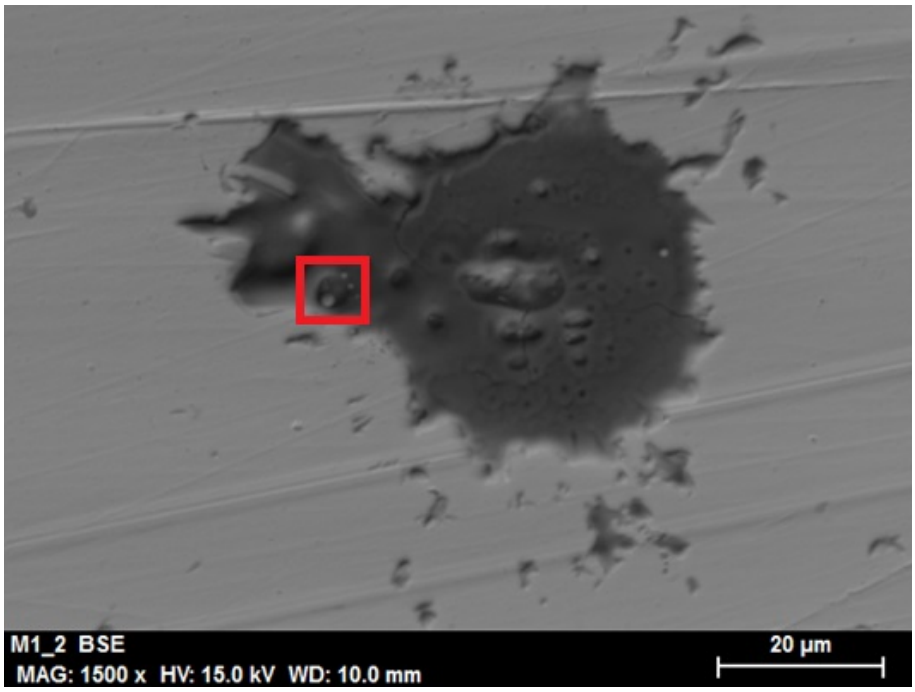

Figure 5.68: Unmelted particles inside a splat on the sample 1, cluster 2

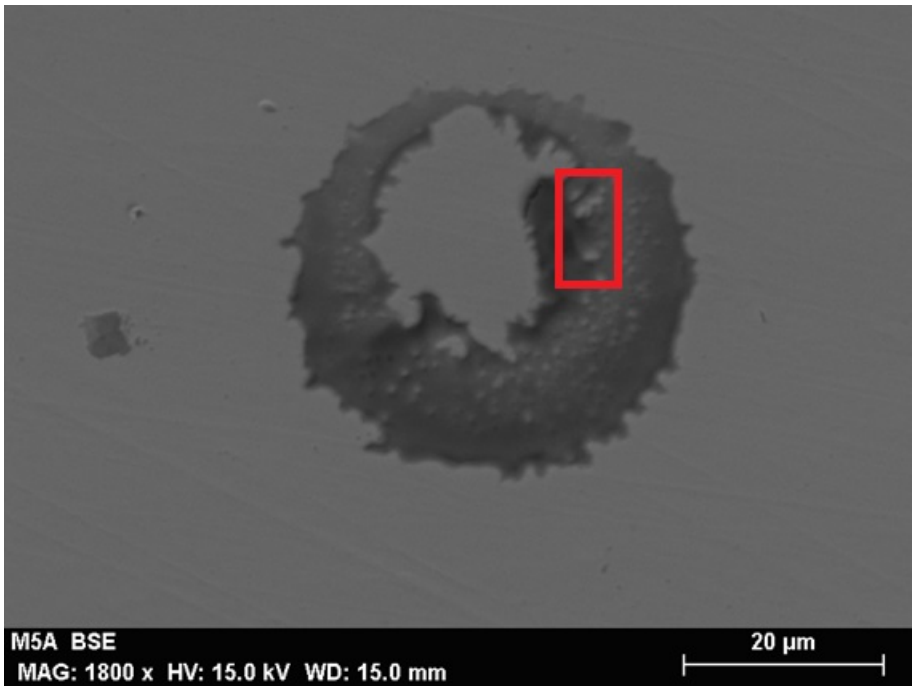

Figure 5.69: Unmelted particles inside a splat on the sample 5, face A

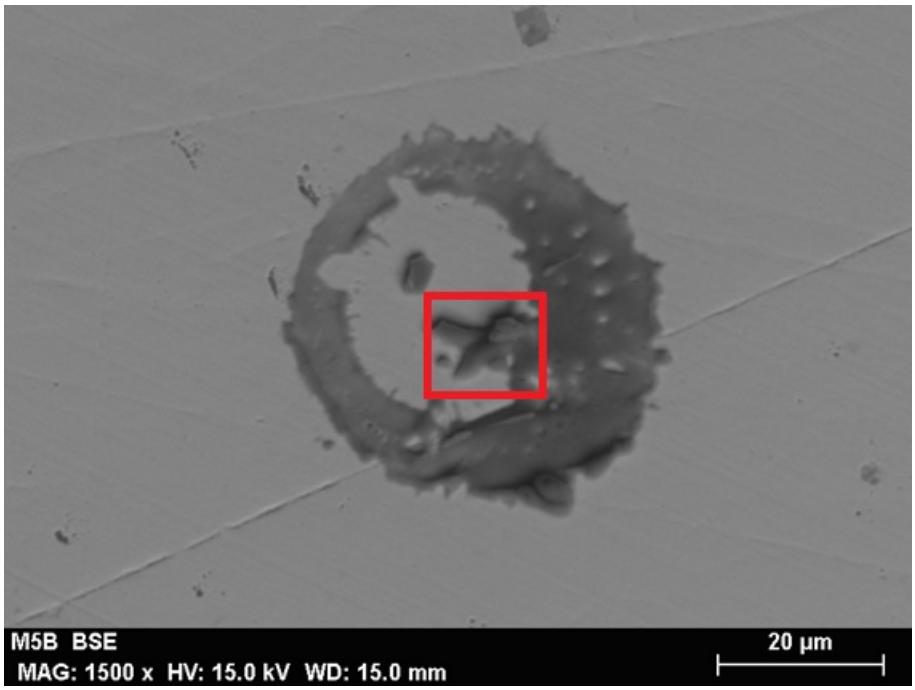

Figure 5.70: Unmelted particles inside a splat on the sample 5, face B

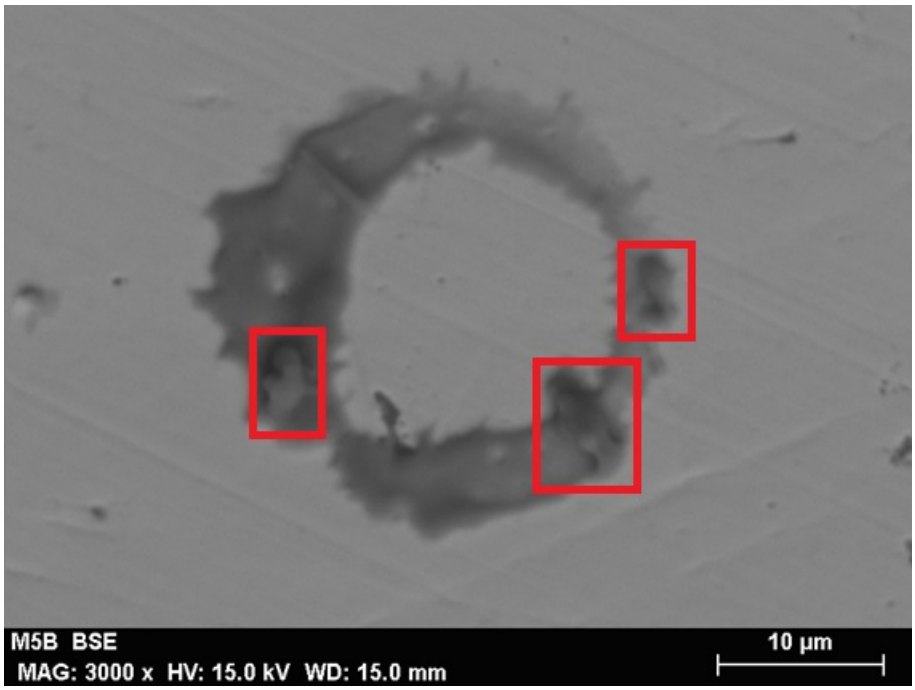

Figure 5.71: Unmelted particles inside a splat on the sample 5, face B

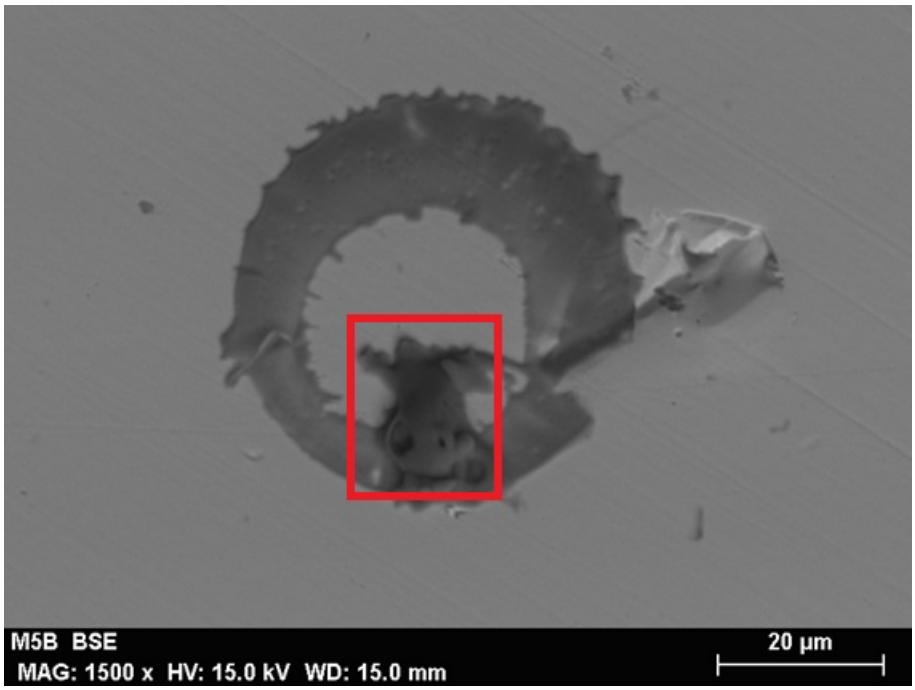

Figure 5.72: Unmelted particles inside a splat on the sample 5, cluster B

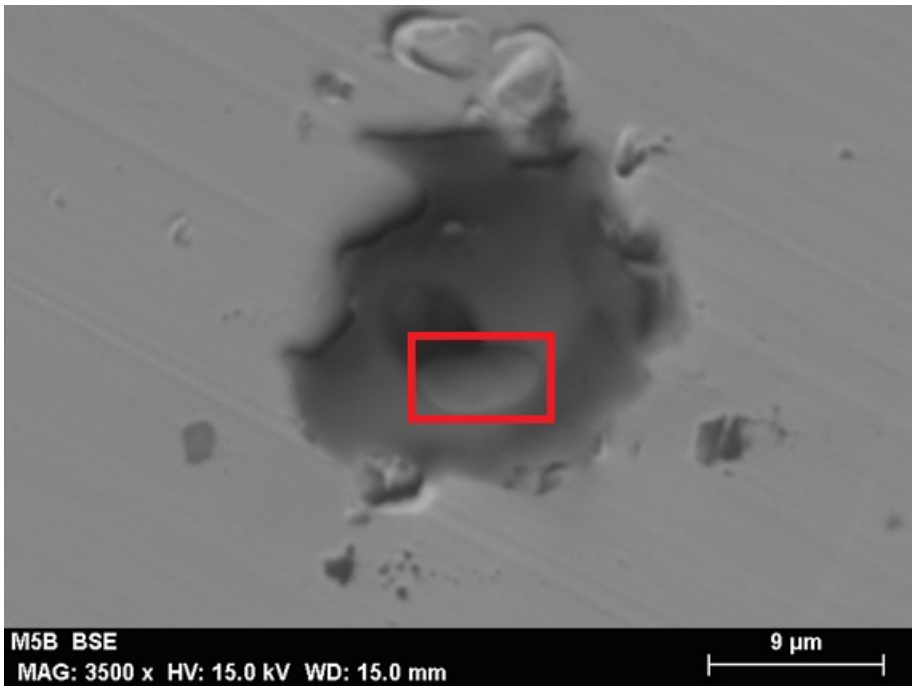

Figure 5.73: Unmelted particles inside a splat on the sample 5, cluster B

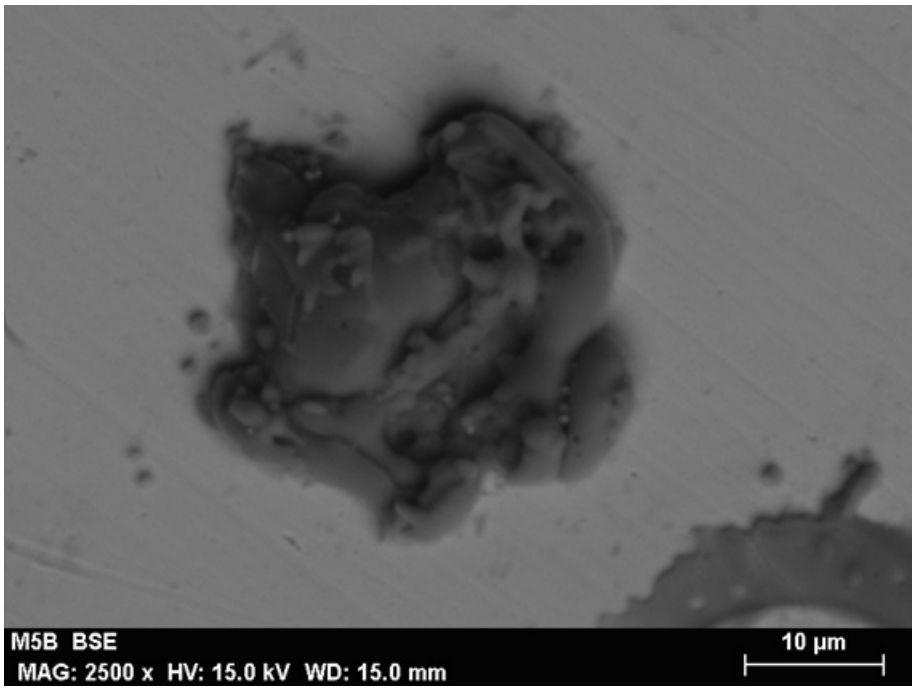

Figure 5.74: Unmelted particles inside a splat on the sample 5, cluster B

Conclusions

The literature relative to splat morphology has been reviewed in order to obtain all available information about the cause of pores and cracks in splats. Also the relationship between the coating manufacture parameters and splat morphology, and the relationship between splat morphology and coating strength, has been collected.

To get the most complete information, the splat has been studied from different point of views: top view and cross section view.

A review of the splats in five samples has been done. The cross section has been obtained. Unfortunately, the internal structure is not clear, and a chemical treatment must be applied.

From the top view images, several analyses have been done: splat contour detection and equivalent diameters calculation. An additional study has been implemented in order to classify the size of the two most frequent splat morphologies: doughnut and pancake.

A code has been programmed in order to automatize the image processing. Several additional operations have been necessary to obtain the inner and outer diameters of the doughnut splats and the diameters of the doughnut splats.

From the analysed samples coating and splat characteristics have been identified by simple visual analysis. To be more precise, it has been found:

a) A big amount of pores has been found through the entire cluster of samples shown in this work. These pores are produced by the presence of adsorbates and condensates at the naked substrate.

b) Blisters and columns have been found. The gases intend to reach the surface leading to these shapes.

c) Some particles present a small quantity of material which remains unmelted after the impingement. These structures are formed from alumina not melted at the spray plume or with a poor temperature reception.

From the visual analysis we strongly recommend vacuum or preheating in order to avoid blisters and pores.

Expression of the thanks

The author wishes to express that the development of this Final Degree Project has been possible thanks to the invaluable help of IFKB, through the collaboration of Dr. Rainer Gadow and PhD. Venancio Martínez.

He also expresses his deep sense of gratitude to his guide and supervisor, Dr. José Andrés Moreno Nicolás, for their invaluable guidance, motivation and attention at all stages of this work; as well as to the Polytechnic University of Cartagena. He also shows gratitude to Dr. Juan Francisco Zapata Pérez for the interesting advices about image processing software.

He also wants to express gratitude especially to María José Roca Hernández, who helped him in the SEM image acquisition, belonging to SAIT institution and in the Department of Materials and Manufacturing Fernando Ródenas Moncada.

He also wishes to acknowledge with gratitude the support that came from his family members and friends to see the completion of this work.